UNIVERSITY OF CALIFORNIA SAN DIEGO

Optimized Systems and Calibration of Millimeter-Wave Phased-Arrays for 5G, SATCOM and Radar Applications

A dissertation submitted in partial satisfaction of the
requirements for the degree
Doctor of Philosophy

in

Electrical Engineering (Electronic Circuits and Systems)

by

Zhe Zhang

Committee in charge:

Professor Gabriel M. Rebeiz, Chair
Professor Gert Cauwenberghs
Professor Brian Keating
Professor Vitaliy Lomakin
Professor Daniel Sievenpiper

2021

The dissertation of Zhe Zhang is approved, and it is acceptable in quality and form for publication on microfilm and electronically.

University of California San Diego

2021

DEDICATION

To my beloved Parents, family, and friends

EPIGRAPH

Quiet people have the loudest minds

– Stephen Hawking

TABLE OF CONTENTS

LIST OF FIGURES

LIST OF TABLES

ACKNOWLEDGEMENTS

I would first like to thank my advisor, Professor Gabriel M. Rebeiz, for his invaluable expertise, generous support and guidance during my master and doctoral studies. I still remembered when I took his ECE 166 course during my last year of undergraduate study at UCSD in 2016, I was deeply intrigued and inspired by the class, which led to my pursuit of the field of RF and microwave engineering. Later during my first year of graduate study, I was introduced to the world of antennas and phased array design by his also interesting ECE 222A. I am always amazed by Prof. Rebeiz passion in teaching. His classes have a huge impact on my choice of career, and I believe they also inspire many more students to choose the field of RF, microwave and antenna engineering. A year later in 2018, I was contacted by Prof. Rebeiz to be his teaching assistant in his ECE 222A, and asked if I was interested in pursuing a Ph.D. degree in antennas and phased array design. When I first joined the group, I was very anxious because I no real design experience in this field, only the fundamental theories I learned from the classes. Prof. Rebeiz along with every TICS group members provided me tremendous support during my 3 years of research, helped me pick up skills after skills and made me confident in tackling problems independently as I have become now. I cannot emphasize enough how grateful I am for this invaluable opportunity to work with Prof. Rebeiz, and his mentoring, patience and trust in me in the past 5 years.

I would like to thank my dissertation committee members, Prof. Gert Cauwenberghs, Prof. Brian Keating, Prof. Vitaliy Lomakin and Prof. Daniel Sievenpiper for their time, interest, and valuable comments about my research studies.

I would like to thank Ahmed Nafe, Bhaskara Rupakula, Kevin Low, Yusheng Yin, Gokhan Gultepe, Tom Phelps and Jacob Schalch for their help on my research projects, technical discussions and friendship.

I would like to thank all my other TICS group colleagues that I had the honor to spend time with, Siwei Li, Li Gao, Yaochen Wang, Changtian Wang, Qian Ma, Shufan Wang, Zhaoxin

Hu, Qian Ma, Hyunchul Chung, Linjie Li, Tian Liang, Abdurrahman Aljuhani, Abdulrahman Alhamed, Oguz Kazan, Mustafa Lokhandwala, Sultan Alqarni, Eric Wagner, Umut Kodak, and Omar El-Aassar, for their technical discussions and friendship.

I would like to thank my girlfriend Jiawei Huang, whom I met around the time I joined the group, and accompanied me through out my entire doctoral study. The path to a Ph.D. degree is not easy, but it was a lot easier with her.

Most importantly, I would like to express my gratitude to my parents for their unconditional support. In September 2013, I left home and began my study in the United States. During the 8 years I spent at UCSD, they have supported every decision I made and even tolerated my sometimes unreasonable behavior. This long separation has been as hard for them, if not harder, as it has been for me, and I cannot achieve anything I have now without their support.

This dissertation was completed with the generous support of Semiconductor Research Corporation and The Defense Advanced Research Projects (DARPA) under the Joint University Microelectronics Program (JUMP), Keysight Technology, Mirise/Toyota, Renesas Electronics America (formerly IDT), and Kyocera International, San Diego.

The material in this dissertation is based on the following papers which are either published, has been submitted for publication, or contains material that is currently being prepared for submission for publication.

Chapter 2, in part, is a reprint of the material as it appears in: Y. Yin, Z. Zhang, T. Kanar, S. Zihir and G. M. Rebeiz, "A 24-29.5 GHz 256-Element 5G Phased-Array with 65.5 dBm Peak EIRP and 256-QAM Modulation," *2020 IEEE/MTT-S International Microwave Symposium (IMS),* Los Angeles, CA, USA, 2020, pp. 687-690, doi: 10.1109/IMS30576.2020.9224031. The dissertation author was the co-author of this paper.

Chapter 2, in full, is a reprint of the material as it may appear in: Z. Zhang, Y. Yin and G. M. Rebeiz, "Intersymbol Interference and Equalization for Large 5G Phased Arrays with Wide Scan Angles," in *IEEE Transactions on Microwave Theory and Techniques,* vol. 69, no. 3, pp.

1955-1964, March 2021, doi: 10.1109/TMTT.2020.3048005. The dissertation author was the primary investigator and author of this paper.

Chapter 3, in part, is a reprint of the material as it appears in: Y. Yin, Z. Zhang, T. Kanar, S. Zihir and G. M. Rebeiz, "A 24-29.5 GHz 256-Element 5G Phased-Array with 65.5 dBm Peak EIRP and 256-QAM Modulation," *2020 IEEE/MTT-S International Microwave Symposium (IMS),* Los Angeles, CA, USA, 2020, pp. 687-690, doi: 10.1109/IMS30576.2020.9224031. The dissertation author was the co-author of this paper.

Chapter 3, in full, is a reprint of the material as it may appear in: Z. Zhang, J.S. Schalch, Y. Yin and G. M. Rebeiz, "System-Level Analysis and Measurements of Thinned Randomized 27-29 GHz TX and RX Arrays for 5G Communications and for Radars with Low Sidelobe Levels," in *IEEE Transactions on Microwave Theory and Techniques,* submitted. The dissertation author was the primary investigator and author of this paper.

Chapter 4, in part, is a reprint of the material as it appears in: Y. Yin, Z. Zhang, T. Kanar, S. Zihir and G. M. Rebeiz, "A 24-29.5 GHz 256-Element 5G Phased-Array with 65.5 dBm Peak EIRP and 256-QAM Modulation," *2020 IEEE/MTT-S International Microwave Symposium (IMS),* Los Angeles, CA, USA, 2020, pp. 687-690, doi: 10.1109/IMS30576.2020.9224031. The dissertation author was the co-author of this paper.

Chapter 4, in full, is a reprint of the material as it may appear in: Z. Zhang, A. Nafe, Y. Yin and G. M. Rebeiz, "Improved 5G and SATCOM Phased-Array Calibration Using the 2×2 Quad-Antenna Method," in *IEEE Transactions on Microwave Theory and Techniques,* submitted. The dissertation author was the primary investigator and author of this paper.

Chapter 5, is coauthored with Nafe, Ahmed, Yin, Yusheng and Rebeiz, Gabriel M. The dissertation author was the primary investigator and author of this chapter.

VITA

2017	Bachelor of Science in Electrical Engineering, University of California San Diego, CA, USA
2019	Masters of Science in Electrical Engineering (Electronic Circuits and Systems), University of California San Diego, CA, USA
2021	Doctor of Philosophy in Electrical Engineering (Electronic Circuits and Systems), University of California San Diego, CA, USA

PUBLICATIONS

Z. Zhang, Y. Yin and G. M. Rebeiz, "Intersymbol Interference and Equalization for Large 5G Phased Arrays With Wide Scan Angles," in *IEEE Transactions on Microwave Theory and Techniques,* vol. 69, no. 3, pp. 1955-1964, March 2021, doi: 10.1109/TMTT.2020.3048005.

Z. Zhang, J.S. Schalch, Y. Yin and G. M. Rebeiz, "System-Level Analysis and Measurements of Thinned Randomized 27-29 GHz TX and RX Arrays for 5G Communications and for Radars with Low Sidelobe Levels," in *IEEE Transactions on Microwave Theory and Techniques* (submitted).

Z. Zhang, A. Nafe, Y. Yin and G. M. Rebeiz, "Improved 5G and SATCOM Phased-Array Calibration Using the 2×2 Quad-Antenna Method," in *IEEE Transactions on Microwave Theory and Techniques* (submitted).

S. Li, Z. Zhang, B. Rupakula and G. M. Rebeiz, "An Eight-Element 140-GHz Wafer-Scale IF Beamforming Phased-Array Receiver With 64-QAM Operation in CMOS RFSOI," in *IEEE Journal of Solid-State Circuits,* doi: 10.1109/JSSC.2021.3102876.

S. Li, Z. Zhang, B. Rupakula and G. M. Rebeiz, "An Eight-Element 140 GHz Wafer-Scale Phased-Array Transmitter with 32 dBm Peak EIRP and > 16 Gbps 16QAM and 64QAM Operation," *2021 IEEE/MTT-S International Microwave Symposium (IMS),* Atlanta, GA, USA, Jun., 2021.

T. Phelps, Z. Zhang, and G. M. Rebeiz, "Simultaneous Channel Phased- Array Calibration Using Orthogonal Codes and Post Coding," *2021 IEEE/MTT-S International Microwave Symposium (IMS),* Atlanta, GA, USA, Jun., 2021.

Y. Yin, Z. Zhang, T. Kanar, S. Zihir and G. M. Rebeiz, "A 24-29.5 GHz 256-Element 5G Phased-Array with 65.5 dBm Peak EIRP and 256-QAM Modulation," *2020 IEEE/MTT-S International Microwave Symposium (IMS),* Los Angeles, CA, USA, 2020, pp. 687-690, doi: 10.1109/IMS30576.2020.9224031.

ABSTRACT OF THE DISSERTATION

Optimized Systems and Calibration of Millimeter-Wave Phased-Arrays for 5G, SATCOM and Radar Applications

by

Zhe Zhang

Doctor of Philosophy in Electrical Engineering (Electronic Circuits and Systems)

University of California San Diego, 2021

Professor Gabriel M. Rebeiz, Chair

Phased array technologies has been in development for many decades but primarily in defense industry with large complicated systems and excessively high cost. With the recent advances in silicon chips and printed-circuit board (PCB) manufacturing, planar phased arrays can be built on a PCB in a compact form with drastically lower cost. The new 5G communication standards also utilize millimeter wave bands that require phased arrays with high effective isotropic radiated power (EIRP) and beam steering capabilities. The 5G systems, with the fast growing industry of satellite communications on-the-move, and millimeter wave automotive radars used for self-driving technologies, contribute to a giant market in need of a large amount

of low cost phased arrays. This dissertation focuses on such commercial-use phased arrays, studies their artifacts and how to eliminate them, provides solutions to optimized phased-array systems, and proposes calibration methods essential for their performance. First, it presents the intersymbol interference (ISI) caused by the phased array when it is scanned with a simple effective equalization scheme, and then, it presents a TX/RX phased-array system with a reduced number of randomly distributed elements that is optimized for radar applications. This dissertation also presents a new method for phased array calibration based on 2×2 sub-arrays that is more robust across different scan angles and yields better performance while reducing the measurement time. Finally, a method to measure the error vector magnitude (EVM) of the phased array in the near-field is presented, which can be used to verify the calibration and performance of phased arrays in communication systems when they are deployed in the field.

Chapter 1

Introduction

1.1 Phased Arrays in 5G, SATCOM and Radar

As the internet, social networks and digital content become more and more important part of people's lives, our cell phones are becoming equipped with more and more functionality and are starting to replace the role of traditional computers. This has led to a large demand for a mobile communication network with a huge capacity and high bandwidth, and capable of gigabit-per-second data transmission and low latency.

Since the first announcement in 2016 and initial deployment in 2019, the fifth generation (5G) communication standard has been aimed to achieved the goals above. As shown in Fig. 1.1, The 5G standard will not only increase the link data rate, but will also integrate itself into more aspects of our lives, such as Internet-of-Things (IoT) to connect more intelligent appliances, and autonomous driving that allow for faster car-to-car communications and advanced safety standards [1].

Numerous technologies has developed for 5G systems, including massive MIMO (multiple-input multiple-output), millimeter-wave (mmWave) bands, beamforming, small cells, etc [11]. Although these technologies cannot be separated from each other in the development of 5G

Figure 1.1: An overview of the 5th generation (5G) communication applications [1].

networks, this thesis will focus on two of them, millimeter-waves and beamforming, that are related and even essential to research in phased arrays.

Traditionally, millimeter-wave spectrum is used mainly for defense applications and ka-band satellite communications. The previous generations of mobile communications utilize frequency bands under 6 GHz (sub-6 GHz bands), and part of the 5G standard for the first time incorporates mmWave spectrum into mobile communications. Millimeter-wave frequency bands have the advantage of higher waveform bandwidth for the same relative bandwidth, and is essential to achieve gagabit-per-second wireless transmission. However, due to the higher frequency and the antenna aperture size with respect to the wavelength, signals at millimeter waves experience drastically higher space loss compared to sub-6 GHz bands, which necessitates antennas with high directivity and large effective isotropic radiated power (EIRP) to compensate for the increased space loss. The millimeter-wave antennas also have beamforming capabilities to focus the radiated power on end users, and hence the introduction of phased array systems, also know as active electronically steered array antennas (AESA), to 5G systems.

Millimeter-wave 5G bands have been deployed in the United States and licensed all over the world and mainly range from 24 to 29 GHz and from 37 to 40 GHz, with the U.S. and

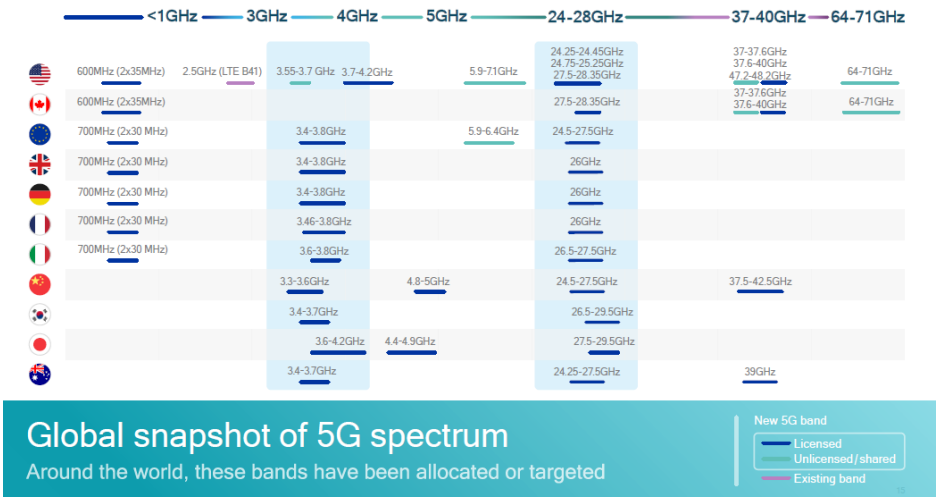

Figure 1.2: Licensed 5G millimeter-wave bands around the world [2].

Canada also sharing allocation from 64 to 71 GHz for unlicensed spectrum (Fig. 1.2) [2]. Note that a large portion of the 5G bands reside in the sub-6 GHz frequencies. Both Sub-6 GHz and millimeter-wave bands will likely co-exist and are important parts of the 5G networks as the sub-6 GHz bands provide better coverage and millimeter-wave bands deliver the best performance. The research in this thesis mainly focuses on the phased arrays designed to operate at 24-29 GHz but the findings can be applied to other frequencies as well.

A large effort has been done by industry to develop antennas and active phased-array systems for cell phones and base stations. Fig. 1.3 presents a prototype cell phone with three 2×4 phased array units placed at different locations (Qualcomm) [3], 5G integrated radio units with 1024 antennas for base stations from Samsung [4], and a Nokia AirScale 28 GHz 5G Active Antenna unit with two millimeter-wave phased arrays [5]. Several manufacturers have also introduced cell phones equipped with millimeter-wave 5G to the consumer's market, such as the iPhone 13 and Samsung Galaxy S21, etc.

Even though millimeter-wave 5G or 5G in general is not yet the dominant technology for mobile communications, it will grow into a market with the size comparable or even larger than the current 4G market in the coming few years. With the huge number of users and devices, and

Figure 1.3: (a) A Qualcomm's cell phone prototype with 2×4 arrays for 5G communications [3]. (b) Samsung's mmWave 5G NR integrated radio unit with 1024 antennas [4]. (c) Nokia AirScale 28 GHz 5G Active Antenna [5]

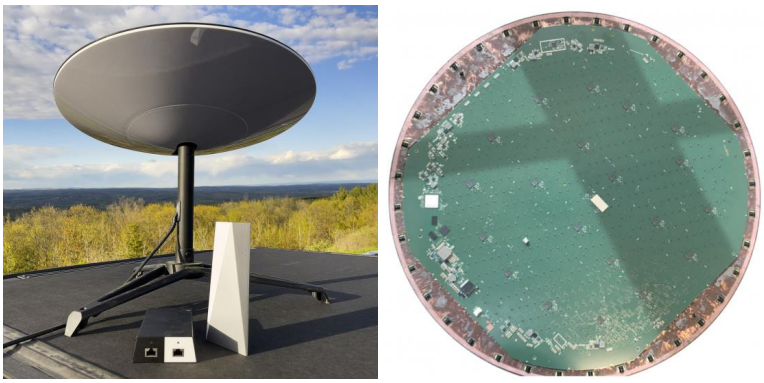

Figure 1.4: Starlink ku-band phased array for SATCOM and its interior PCB [6, 7].

a technology newly introduced to high-data rate communications, it is important to study and understand the artifacts that come with certain usage scenarios, and find solutions to optimized the performance of the phased arrays. Moreover, with the narrow beams inherent in phased arrays, a target tracking algorithm is necessary for smooth operation, and an effective calibration method is essential for accurate beam tracking and delivering good performance to millions of end users. Therefore, these aspects of the phased arrays will be the focus of this thesis.

In addition to 5G, low earth orbit (LEO) satellite communications is another force pushing

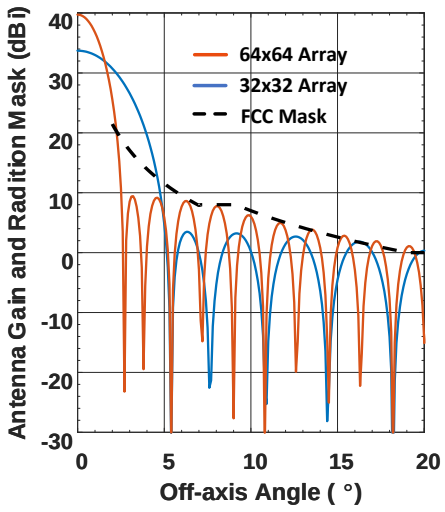

(a)

$29-25\log^{10}\theta$	dBi	for $2° \le \theta \le 7°$.
8	dBi	for $7° < \theta \le 9.2°$.
$32-25\log^{10}\theta$	dBi	for $9.2° < \theta \le 19.1°$.
0	dBi	for $19.1° < \theta \le 180°$.

FCC Sec. 25.209

(b)

Figure 1.5: (a) Radiation mask for Ka-band SATCOM on top of patterns of 32×32 and 64×64 phased array patterns with -30 dB Taylor taper. (b) FCC Radiation mask for Ka-band SATCOM antennas [8].

the development of commercial phased arrays, and with the most notable example being the Starlink systems operated by SpaceX [6, 7]. Starlink has already launched over 1800 satellites and aims to have tens of thousands of satellites in orbit. Internet service is now available to users for 99 US dollars a month and a one-time payment of 499 dollars for the hardware [12]. Along with other companies following suit, SATCOM will be another large market for phased arrays.

The necessity of calibration of phased arrays used in SATCOM lies in the stringent radiation mask requirements [8]. The beam width and sidelobe levels of the patterns are strictly regulated by the Federal Communications Commission (FCC) and require aggressive tapers on the apertures and accurate calibration to meet the requirements. Fig. 1.5 presents the radiation mask and simulated patterns for a 32×32 and 64×64 array with -30 dB Taylor taper applied. For the 64×64 array, the pattern barely meet the FCC regulation even with -30 dB Taylor taper, and a

Figure 1.6: An NXP 77-GHz phased array for automotive radar [9].

phased array with at least 4000 elements is required for the narrow beam width.

Another important application for millimeter-wave phased arrays is automotive radar. Fig. 1.6 shows a 77 GHz radar module made by NXP [9]. With the current research and investment in autonomous driving, complicated millimeter-wave radar modules together with powerful processing units are expected to be introduced in future vehicles, and provide both high resolution and long range object detection. In addition to well calibrated phased arrays required for high performing radar systems, the thesis also presents an optimized radar systems with reduced elements and cost, which still delivers the required performance for automotive radar.

1.2 Thesis Overview

This thesis presents studies on millimeter-wave low cost planar phased array that can be used for 5G communication, SATCOM, and radar applications, and several methods for calibrating and optimizing the systems with these phased arrays.

Chapter 2 presents the Intersymbol interference (ISI) that is introduced in a phased array when the beam is scanned. The cause of the ISI is demonstrated and its dependence on the phased array dimensions, scan angle, and symbol rate is derived. A mathematical model is created to simulate the ISI effects on transmitted (or received) symbols, and an equalizer model is introduced and achieves near-perfect equalization of the ISI. Also, for wideband signals, it is shown that large phased-arrays result in amplitude modulation versus frequency. The effect of ISI on the error vector magnitude (EVM) is simulated using complex modulated signals, and the EVM before and after equalization are compared, using an adaptive 17-tap linear equalizer implemented in MATLAB. The results show that ISI in large phased arrays can be equalized regardless of the modulation, bandwidth, scan angle and symbol rate. The EVM of 16-, 64- and 256-QAM signals are measured for a 256-element array in the transmit mode. The measurements verify the derivations, eliminating ISI and resulting in low EVM values after equalization. The effect of array tapering on EVM is also presented and the results show no difference on the EVM for uniform and tapered excitation.

Chapter 3 presents a novel approach for radars with greatly reduced number of elements while still keeping narrow beamwidths and low sidelobe levels. The design is based on thinned transmit (TX) and receive (RX) arrays, each one randomized in an orthogonal fashion, such that the high sidelobes in one pattern (TX or RX) are greatly reduced by nulls in the other pattern (RX or TX). The goal is to build communication arrays and radars with narrow beamwidths but with one half or one quarter of the elements in the TX and RX arrays. This approach lowers the cost of large-aperture systems typically requiring hundreds or thousand of elements, while still

keeping a high degree of fidelity in the patterns (beamwidth, sidelobes, and scan volume). The thinned-array impact on the transmit effective isotropic radiated power (EIRP), receive gain, and 16 and 64-QAM EVM versus radiated power are also considered in this paper. These concepts can be applied to 24 GHz and 77 GHz automotive radars for collision avoidance and imaging systems, and in X, Ku and Ka-band air-to-air due-regard radars, landing systems and other applications.

Chapter 4 presents a new method for phased-array calibration, and is particularly suited for large phased-arrays. Different than the traditional calibration method where each antenna element is measured one-at-a-time, this method measures quad unit cells (2×2 antennas), with the quad calibration procedure applied on the whole array. Another correction may also be done inside a single quad to determine the variations within the quad. The method results in better signal to leakage ratio (12 dB higher dynamic range), is four times faster than the traditional method, and most important, removes the pattern ripples when a single element is turned on, thus reducing the required variable gain amplifier (VGA) dynamic range for array calibration. The work also shows that the traditional method converges to the quad-method if measured individually and averaged mathematically. A 256-element 5G phased-array is calibrated at 27-28 GHz using this technique, and results in better calibration and sidelobes than the traditional method. The 2×2 quad-calibration method can also be applied to satellite phased-arrays and other large phased-array such as radars and mm-wave imaging systems.

Chapter 5 presents a method of measuring the error vector magnitude of the phased array utilizing the mutual coupling between antennas. This chapter is an extension of the built-in-self-test (BIST) calibration which calibrate the amplitude and phase of each channel using the mutual coupling symmetry, and great success has been demonstrated [13]. The measured EVM of complex modulated signals is an important metric showing the performance of phased arrays used for communication applications. With the fast growing market in millimeter-wave 5G and SATCOM, it becomes impractical to measure every arrays in the far-field due to cost and time constraints. Therefore, a near-field measurement that uses the TX and RX channels of the array

itself provides a good way to verify the array performance in large volume. In this chapter, a 4×8×8 28-GHz TX/RX phased array is used for EVM measurement. The array is consist of 4 quadrant each with independent RF input/output and can be set to TX or RX mode individually. One quadrant is set to TX mode as the "quad under test" and another adjacent quadrant is set to RX probes. The near-field results are compared to the far-field one and show close trend with differences caused by the linearity of the RX channels.

Chapter 6 concludes the dissertation and discusses future work.

Chapter 2

Intersymbol Interference and Equalization for Large 5G Phased-Arrays with Wide Scan Angles

2.1 Introduction

Recent advancements in the fifth generation (5G) millimeter-wave communication systems with multi-gigabit-per-second data links have encouraged the development of highly integrated, low-cost phased array systems [14–29]. To overcome the increased path loss of millimeter-wave signals, a large phased array with 128 to 512 elements and high equivalent isotropic radiated power (EIRP) is desired. To compensate the narrow beamwidth resulting from large apertures and also to increase the coverage area, the phased array needs to be able to scan to wide angles. This article investigates the distortions created by a phased array under wide scan angle conditions. Both intersymbol interference (ISI) and amplitude modulations are demonstrated, with a focus on the ISI, which becomes more prominent with larger array size and scan angle.

Previous works have studied the ISI effects and its equalization in a communication

systems [30–40]. This work, which is an expansion of [10], focuses on the ISI created by the phased array itself, and its effect on the error vector magnitude (EVM) of modulated signals. A solution consisting of a multi-tap linear equalizer is proposed and analyzed, and it is demonstrated that even the most serious ISI can be equalized, resulting in low EVM values and excellent performance over all scan angles. Section II demonstrates the cause of the ISI in a phased array and its relation to the array size, scan angle and symbol rate. Section III discusses the amplitude modulation over a wideband spectrum when the phased array is scanned. Section IV presents simulations on the effects of the ISI on the transmitted signals and analytically provides an equalizer model as a solution. Section V presents the simulated effects of ISI and equalizers on phased-array EVM. Section VI presents measurements that verify the calculations and simulations, and section VII concludes the paper.

2.2 ISI in Phased Arrays When Scanned

Fig. 2.1(a) presents a typical 256-element phased-array used for 5G base-stations. The array is composed of 16x16 antennas spaced at 0.5λ and can scan to $\pm 60^{\circ}$ in all planes. This array employs the RF beamforming architecture, but the analysis in this work applies equally for arrays using the LO and IF beamforming techniques [16–18]. The effect of the time-delay of the received (or transmitted) signals between different antenna elements is shown in Fig. 2.1(b). When the phased array is scanned to an angle θ_0, the plane wave results in a finite time delay between the antenna elements. In the receive mode, when the 256 signals are added together in the Wilkinson combiner, the symbols overlap with each other and cause ISI. In the transmit mode, the transmitted signals (i.e. waveforms) add in the direction of propagation with a finite delay and therefore also cause an ISI at the receive antenna. The effect of ISI on symbols is presented in Fig. 2.1(c). It is clear that when two symbols overlapping with each other are combined, the signal amplitudes at the sample points change, which can increase the EVM of amplitude-modulated

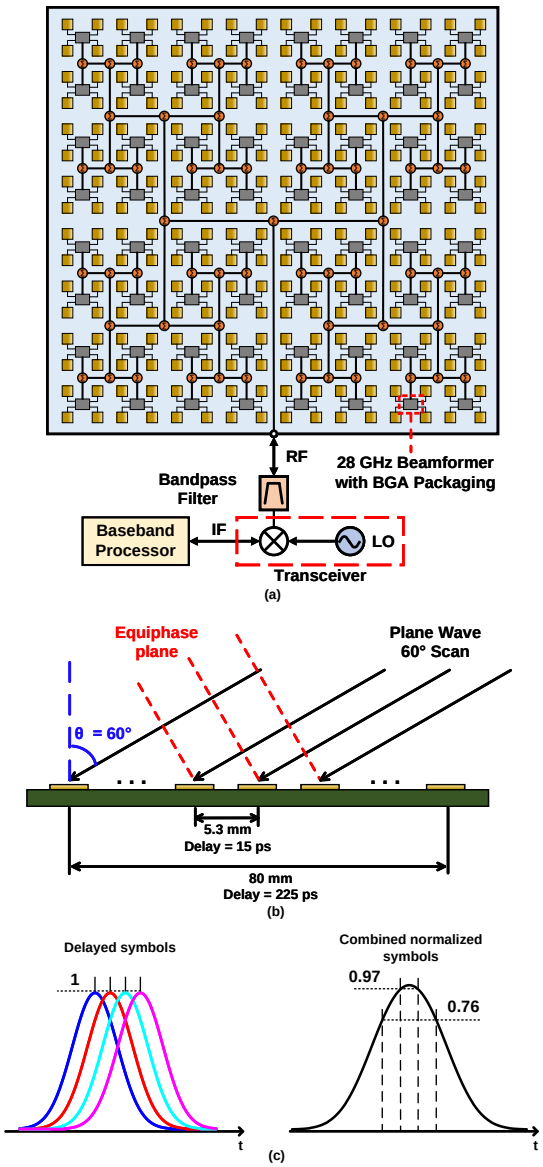

Figure 2.1: (a) A 256-element phased-array using RF beamforming (from [10]). (b) Demonstration of time-delay between antenna elements in a 16x16 28-GHz phased array (from [10]). (c) Demonstration of intersymbol interference.

signals.

The time delay between neighboring antennas in the azimuth-plane is calculated as [41]:

$$TD_{element} = \frac{d_{el} \times \sin(\theta_0)}{c} = 15\ ps \tag{2.1}$$

where d_{el} is the spacing between the antennas, c is the speed of light and $\theta_0 = 60^\circ$. The maximum time delay between antennas at two edges of the phased array is:

$$TD_{array} = \frac{(N-1) \times d_{el} \times \sin(\theta_0)}{c} = 225\ ps \tag{2.2}$$

where N is the number of elements in the scan plane (N = 16 in this case). The delay and resulting ISI increase linearly with the number of elements and is 225 ps from edge-to-edge for a 256-element array (16x16 antenna elements). For an 100-MBaud modulated signal, the unit symbol interval is 10 ns, and the edge-to-edge time delay is at maximum of 2% of the symbol interval, and does not cause significant EVM degradation. However, the symbol interval is inversely proportional to the signal bandwidth, and the 225 ps delay results in an ISI of 20% of the symbol interval for a 1-GBaud waveform. With wide bandwidths required for modern communication systems, such an ISI can result in high EVM and unusable signals.

Since the ISI created by such time delay is linear to antenna positions, it can be equalized using a linear multi-tap equalizer in the transmit (TX) or receive (RX) modem with simple zero-forcing (ZF) or minimum mean-square error (MMSE) algorithms, resulting in very low EVM after equalization and demodulation.

Fig. 2.2(a) presents MATLAB simulated EVM values versus the ISI percentage for 16, 64, and 256-QAM waveforms. The ISI percentage is defined as the time delay between 2 edges of the array (TD_{array}) over a symbol period, given by [42]:

$$ISI_{\%} = 100 \times Symbol\ Rate \times TD_{array} \tag{2.3}$$

The EVM values first increase linearly with the ISI and then saturate at different ISI percentages. The EVM of the higher-order modulations saturates quickly because of the smaller distances between the symbols in the constellations, and the plateaus are caused by one symbol being recognized as another symbol. Note that this results in a higher bit-error-rate (BER), as shown in

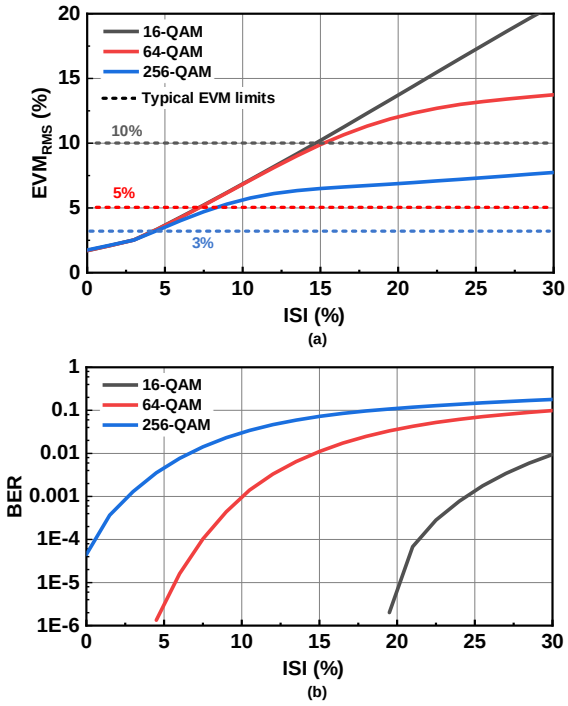

Figure 2.2: Simulated (a) EVM, (b) BER, for different modulation formats versus ISI percentage in terms of symbol period. ISI is defined from edge-to-edge in a phased arrays.

Fig. 2.2(b), but not necessarily a higher EVM, but still, EVM is used here as a measure of fidelity as it will always be reduced to low levels after equalization. Note that an edge-to-edge ISI of 4.5%, which is an ISI of 0.3% between adjacent antennas in a 16×16 array, can cause a 3% EVM, which results in significant distortions on both the 256-QAM and 64-QAM waveforms.

2.3 Far-Field Amplitude Modulation of Wideband Signals In Phased Array when Scanned

In addition to ISI, a phased array also causes amplitude modulation in the far-field at wide scan angles. Due to the use of phase-shifters on every element (as opposed to true-time-delay units), the energy of a wideband signal with frequencies given by f_{min}, f_0, f_{max} are radiated to slightly different angles given by θ_{max}, θ_0, and θ_{min}, respectively. This phenomena is labeled as

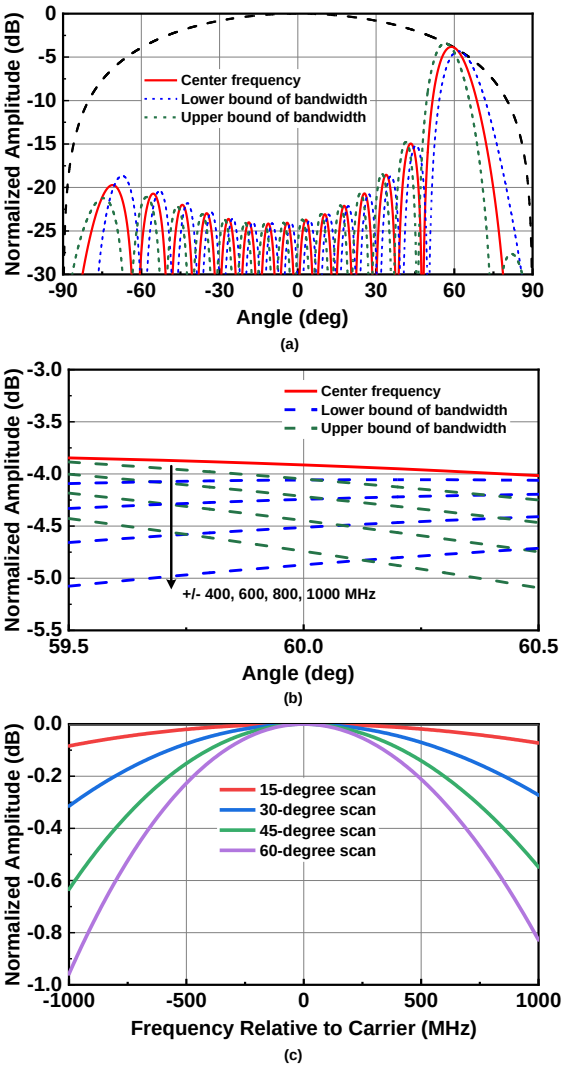

Figure 2.3: (a) Beam squint in phased array when scanned. (b) Expanded view of patterns at ±400 to ±1000 MHz from center frequency. (c) Amplitude modulation caused by beam squint versus frequency offset from the center frequency at different scan angles. Simulated on a 16×16 array.

beam squint and θ is given by:

$$\theta_{min,max} = sin^{-1}(\frac{f_0 \sin(\theta_0)}{f_{max,min}}) \tag{2.4}$$

Depending on the array size, bandwidth and scan angle, the energy radiated to different directions will cause a decrease in signal amplitude in the desired scan angle θ_0, creating amplitude

modulation versus frequency. Fig. 2.3(a) presents the simulated patterns of a 256-element phased array centered at 28 GHz and scanned to 60° for a 1600 MHz bandwidth signal at 27.2 GHz, 28 GHz and 28.8 GHz. Fig. 2.3(b) presents an expanded view of the patterns around 60°. It is shown that the directivity drops by 4 dB following an element factor of $\cos(\theta)^{1.3}$ common in microstrip patch antennas. At a look angle of 60°, beam squinting causes a dip of 0.55 dB and 0.6 dB at 27.2 GHz and at 28.8 GHz, respectively. The amplitude modulation caused by beam squint versus bandwidth and scan angle is given by:

$$\Delta G = \frac{\sin(0.5Nkd_{el}(\sin(\theta_0) - sin(\theta_{squit})))}{N\sin(0.5kd_{el}(\sin(\theta_0) - sin(\theta_{squit})))} \tag{2.5}$$

where k is the wavenumber at f_0, and θ_{squint} is a function of frequency f and can be calculated using (2.4) by replacing f_{min} or f_{max} with f. For a 2-GHz bandwidth and 60° scan angle, the amplitude modulation is 0.95 dB at f_{min} and 0.8 dB at f_{max}. Note that the amplitude modulation versus frequency offset (or signal banwidth) is deterministic and well-behaved and can be easily compensated using a 2nd or 3rd-order polynomial with the opposite trend in an equalizer or using digital predistortion. Even if non-compensated, an amplitude variation of ±0.2-0.5 dB versus waveform bandwidth has a minor effect on the EVM for a 64-QAM waveform.

2.4 Equalization of ISI

Fig. 2.4 presents the block diagram used in MATLAB *Simulink* for simulating the ISI in a phased array. A 16×16 array is modeled for an azimuth-plane scan of θ_0, and therefore, 16 channels are used to simulate the different delays encountered by the columns in the array. A single discrete impulse signal preceded and followed by zeroes is generated first for simplicity. The discrete signal is up-sampled and passed through a TX root-raised-cosine filter. A 0°-360° phase shifter, equivalent to 0-33 ps time delay at 30 GHz, with phase state corresponding to the desired scan angle is added to each channel, and its delay is included in simulations. Note

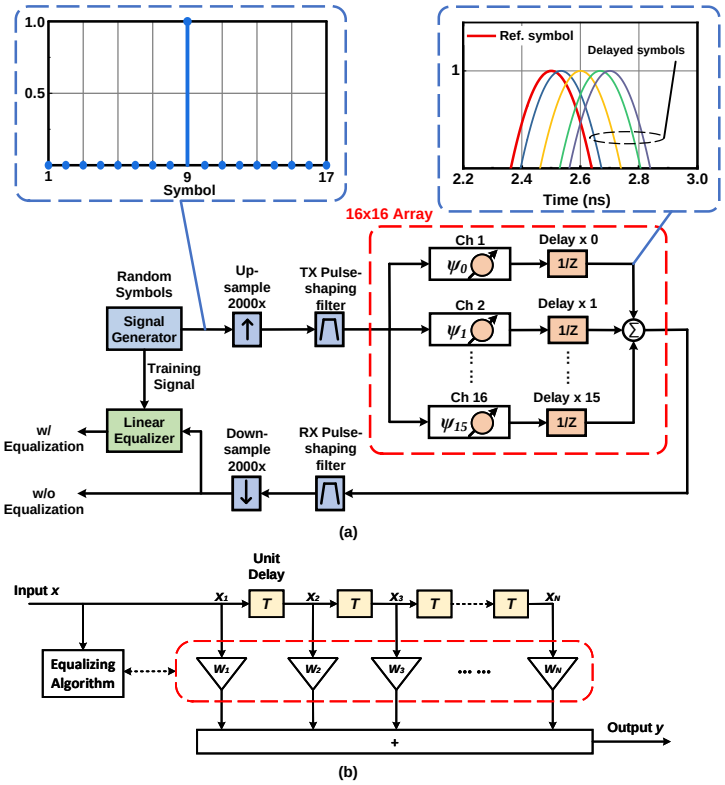

Figure 2.4: (a) Block diagram for MATLAB *Simulink* ISI simulations and (b) equalizer with 17-taps and weights.

that any phase state above 360°, or 33 ps, is wrapped around 0 due to the limited range of the phase shifters. The signal is then combined in free space using an ideal summer, passed by a RX pulse-shaping filter, and down-sampled to its original form of discrete symbols. An equalizer block is then added to analyze the effectiveness of equalizing the array-induced ISI. The equalizer is shown in Fig. 2.4(b) and is a linear 17-tap design with the following characteristics: Input signal X with unit delay T between the symbols are added with different weights W to produce an output equalized signal Y. T is the symbol period and depends on the waveform baud rate. The equalizer tap weights, W, are calculated using minimum mean-square error (MMSE) method, which minimizes the mean-square error of the signal created by ISI. A 17-tap equalizer is used because the phased-array creates 16 different delays in azimuth-plane scan. The number of equalizer taps can also be reduced for ease of use.

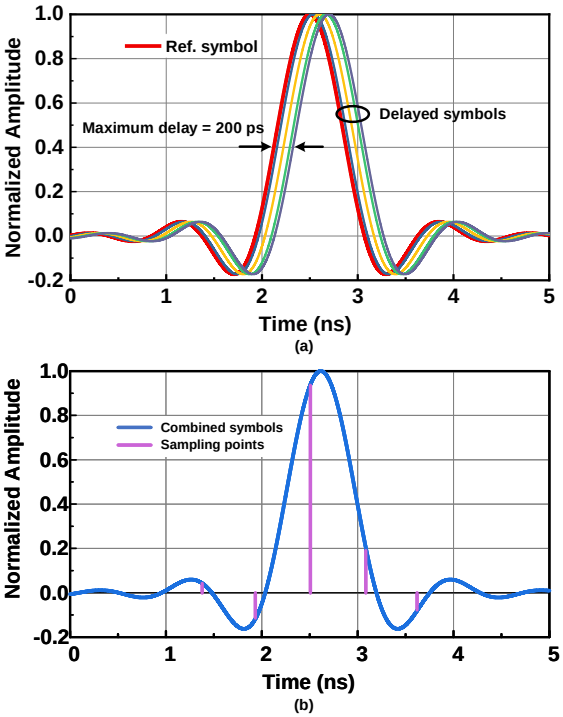

Figure 2.5: (a) The impulse signals after upsampled, passed through a TX root-raised cosine filter and the phased array channels. (b) Combined delayed symbols and their sampling points.

Fig. 2.5(a) presents the delayed symbols after passing by the TX pulse-shaping filter and the 16-channels in the phased-array, done for a symbol rate of 1600 MBaud (symbol period of 625 ps). Symbols from only 5 channels are shown for clarity. The phased-array is scanned to 60° and the edge-to-edge delay is 200 ps, and is 32% of the symbol period. Fig. 2.5(b) presents the upsampled symbols added in free space (or at phased-array sum port) and corresponding sampling points. The sampling points show non-zero amplitude for symbols other than the impulse. The combined downsampled signal is presented in Fig. 2.6(a), with the distortions created by ISI clearly visible in the resulting impulse response. The distorted symbols are then passed through the 17-tap equalizer, with tap weights shown in Fig. 2.6(b).

The tap weights are calculated using MMSE method as [43]:

$$W = R_{xx}^{-1} R_{xy} \tag{2.6}$$

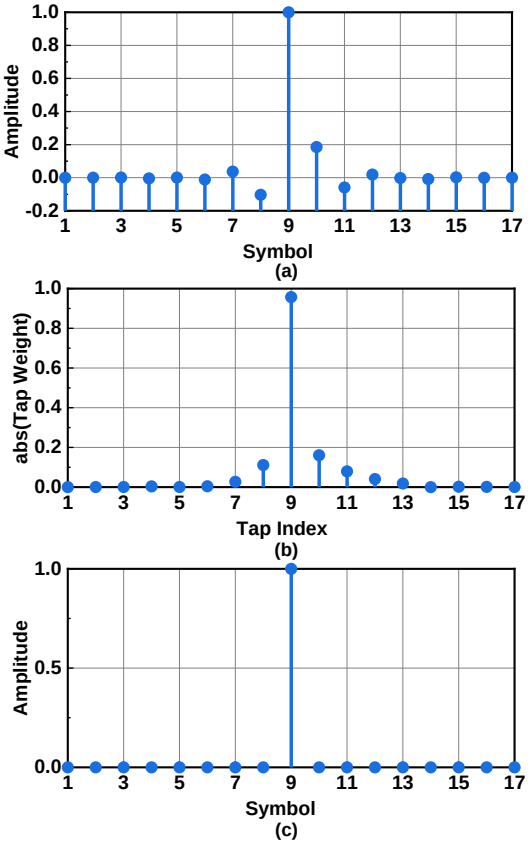

Figure 2.6: (a) Combined down-sampled discrete symbols after passed through RX root-raised cosine filter. (b) Equalizer tap weights. (c) Equalized symbols by convolution between (a) and (b).

where W is a vector with length equal to 17. R_{xx} is the autocorrelation matrix of the input signal X given by

$$R_{xx} = X^T X, \tag{2.7}$$

R_{xy} is the cross-correlation vector given by

$$R_{xy} = X^T Y, \tag{2.8}$$

where Y is the desired output signal. The input signal matrix X is defined as:

$$X = \begin{bmatrix} x(-N) & 0 & 0 & \cdots & \cdots & 0 & 0 \\ x(-N+1) & x(-N) & 0 & \cdots & \cdots & 0 & 0 \\ \vdots & & & \vdots & & & \vdots \\ x(N) & x(N-1) & \cdots & \cdots & \cdots & x(-N+1) & x(-N) \\ \vdots & & & \vdots & & & \vdots \\ 0 & 0 & \cdots & \cdots & 0 & 0 & x(N) \end{bmatrix} \tag{2.9}$$

where $N = (\#\ of\ taps - 1)/2$. X represents a series of symbols with different indices passing through the equalizer at different times. The output vector Y is defined as:

$$Y = \begin{bmatrix} y(-2N) \\ \vdots \\ y(0) \\ \vdots \\ y(2N) \end{bmatrix} \tag{2.10}$$

where

$$y(k) = \begin{cases} 1 & for\ k = 0 \\ 0 & otherwise \end{cases} \tag{2.11}$$

and is used to calculate the equalizer tap weights so as to recover the ideal transmitted signal.

The convolution of the distorted symbols in Fig. 2.6(a) and the tap weights in Fig. 2.6(b) produces the equalized signal in Fig. 2.6(c), which closely matches the ideal transmitted signal. The results show that ISI created in a 256-element phased-array can be equalized using a simple MMSE equalizer model, even with a 1600 MBaud symbol rate at 60° scan. A zero-forcing equalizer model was also used and produces the same results, and is not shown for brevity.

The number of equalizer taps can be reduced for ease of use. Fig. 2.7(a) presents the tap weights of a 9-tap equalizer used to equalized the same 1600-MBaud signal at 60° scan. The resulting equalized symbols also show a good match with the transmitted symbols but with

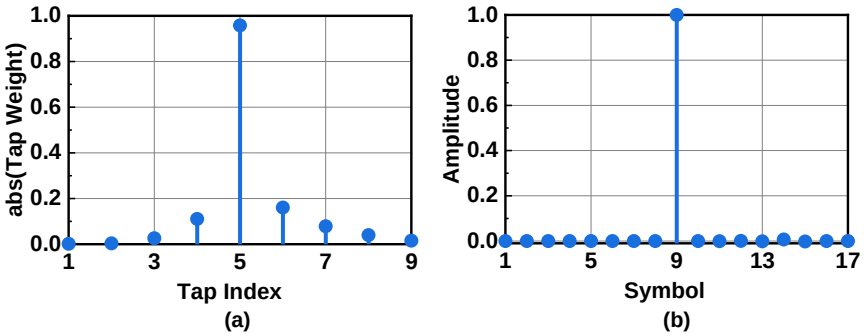

Figure 2.7: (a) Tap weights and (b) equalized symbols using a 9-tap equalizer.

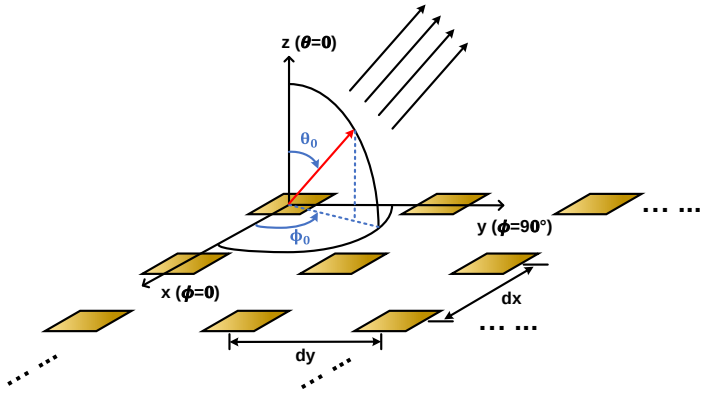

Figure 2.8: A 2-D array with radiation at any scan angle (θ_0, ϕ_0).

slightly higher errors compared to using a 17-tap equalizer. The root-mean-square error of the equalized symbols is 0.0031, and the resulting EVM_{RMS} is 0.5% for a 64-QAM waveform, calculated using [44]:

$$EVM_{RMS} = \frac{\sqrt{\frac{1}{N}\sum_{n=1}^{N} err[n]^2}}{RMS\ of\ Constellation} \times 100\% \tag{2.12}$$

The case where the array is scanned to an arbitrary angle (θ_0 and ϕ_0) is now presented in Fig. 2.8. The maximum time delay with respect to angle θ_0 and ϕ_0 is given by [41]:

$$TD(\theta_0, \phi_0) = \frac{L(\phi_0) \times \sin(\theta_0)}{c} \tag{2.13}$$

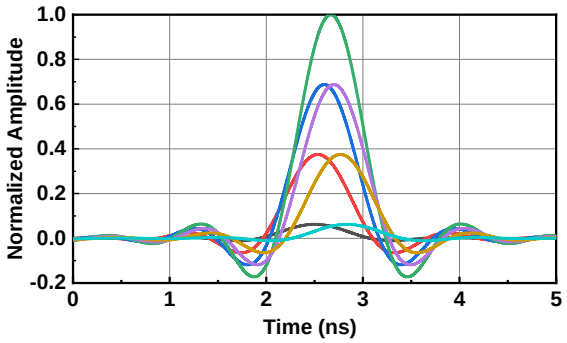

Figure 2.9: The delayed impulse signals after passing through the 16×16 phased-array channels for radiation in the diagonal plane.

where L is the phased-array length in the scanning plane, and is:

$$L(\phi_0) = \sqrt{Dx^2 + (Dy|\tan(\phi_0)|)^2} \tag{2.14}$$

for $-45^\circ < \phi_0 < 45^\circ$ or $135^\circ < \phi_0 < 225^\circ$, and

$$L(\phi_0) = \sqrt{(\frac{Dx}{|\tan(\phi_0)|})^2 + Dy^2} \tag{2.15}$$

otherwise, and Dx and Dy are the array lengths in X and Y directions, respectively. Fig. 2.9 presents the delayed signals with 1600-Mbaud symbol rate when the phased-array is scanned to 60° in the diagonal plane. 31 samples of delayed signals are created by the 256-element phased-array. Because the numbers of antennas in the diagonal columns (projected on the plane of propagation) increase from 1 antenna at the array corner to 16 antennas at the center, and back to 1 again at the other corner, the amplitudes of the signals also increase linearly from the corner towards the center, and then decrease towards the corner again. Only 7 samples are plotted for clarity. The combined distorted impulse response is plotted in Fig. 2.10(a). Following the same procedures for scanning in the azimuth plane, the tap weights of a 17-tap equalizer are presented in Fig. 2.10(b). Since the effective antenna spacing in the diagonal plane ($L(\phi_0)$ in (2.14) and

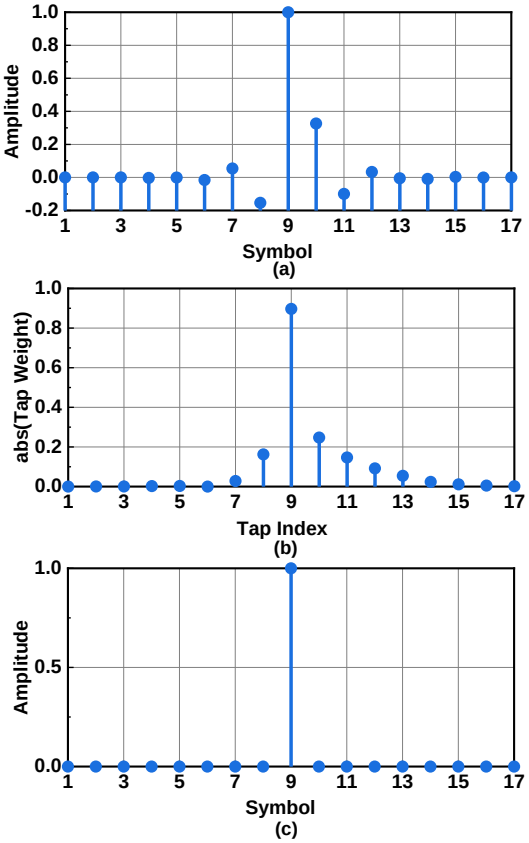

Figure 2.10: (a) Combined down-sampled discrete symbols with diagonal-plane incidence after passing through a root-raised-cosine filter. (b) Equalizer tap weights. (c) Equalized symbols by convolution between (a) and (b).

(2.15) divided by 31 diagonal columns) is smaller, and the center column contribute to the highest weight of the signal amplitude, the signal with 31 delays can be equalized with the same 17-tap equalizer, and result in very small distortions (Fig. 2.10(c)). For completeness, the diagonal plane was also analyzed with a 31-tap equalizer and the EVM values were essentially the same as the 17-tap equalizer.

2.5 EVM Simulations

The EVM of a complex modulated signal before and after equalization is obtained using MATLAB *Simulink* with the block diagram shown in Fig. 2.4 and procedures described in

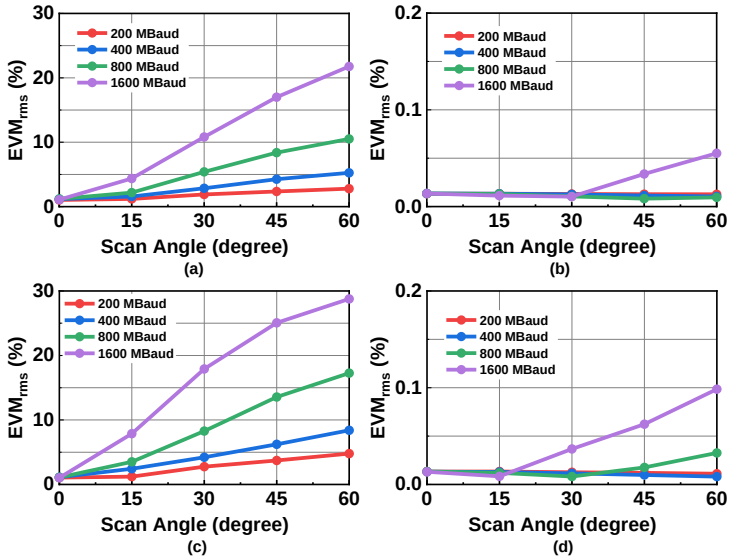

Figure 2.11: Simulated EVM versus scan angle of 16-QAM waveforms of azimuth-plane incidence: (a) without equalizer, (b) with equalizer. Diagonal plane incidence: (c) without equalizer, (d) with equalizer.

section IV. Random symbols with quadrature amplitude modulation (QAM) are generated and passed through the phased-array. A 17-tap linear adaptive equalizer block is added at the end, which changes the tap weights adaptively based on the input signal and the training signal. The equalizer taps are symbol-spaced with a tap-weight resolution of 0.01, and 10% of the ideal QAM waveforms are used for training.

Fig. 2.11 presents the EVM of a 16-QAM waveform versus scan angle at different symbol rates before and after equalization. Fig. 2.11(a) and (b) plot the results when the phased-array is scanned in the azimuth plane and Fig. 2.11(c) and (d) in the diagonal plane. For scanning in the azimuth plane, the EVM increases almost linearly with scan angle, only starting to saturate at 45° scan for 1600-MBaud waveform. After equalization, the signals present near-zero EVM across all scan angles. In the case of scanning in the diagonal plane, higher ISI is present in the combined signals, and the EVM starts to saturate, at 30° scan for a 1600-MBaud waveform. Although the high EVM at 60° scan angle for 1600-MBaud signal cannot be perfectly equalized, the resulting EVM is still very low.

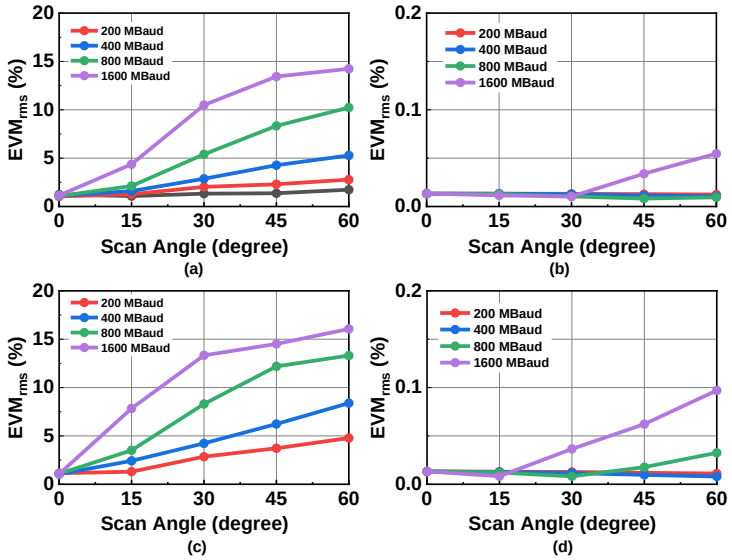

Figure 2.12: Simulated EVM versus scan angle of 64-QAM waveforms in azimuth-plane incidence: (a) without equalizer, (b) with equalizer. Diagonal plane incidence: (c) without equalizer, (d) with equalizer.

The same results for 64-QAM signals are plotted in Fig. 2.12. For signals with lower bandwidth, the EVM increases almost linearly with scan angle. However, due to the symbols closer in the 64-QAM constellation, the EVM for waveforms with higher bandwidths saturate earlier than 16-QAM cases. The 17-tap equalizer also produces near-zero EVM for all cases ($<$ 0.5% in the diagonal plane). By using a 31-tap equalizer, almost perfect equalization and EVM $<$ 0.1% can be achieved across all scan angles, and the results are not shown for brevity. The results show that the ISI created by a phased-array when scanned is independent of the modulation, and all types of signals can be equalized.

Fig. 2.13 presents the simulated EVM values of equalized 64-QAM waveforms using a 9-tap equalizer, in both azimuth-plane and diagonal scan. The 9-tap equalizer successfully equalizes the ISI in most cases, resulting in sufficiently low EVM values ($<$ 1%) for 64-QAM waveforms, except for the case of 1600-MBaud signals scanned to 60° in the diagonal plane. However, the overall equalized EVM values are high compared to using a 17-tap equalizer, which results in near-zero EVM. In general, it is best to use an equalizer with a number at least equal to

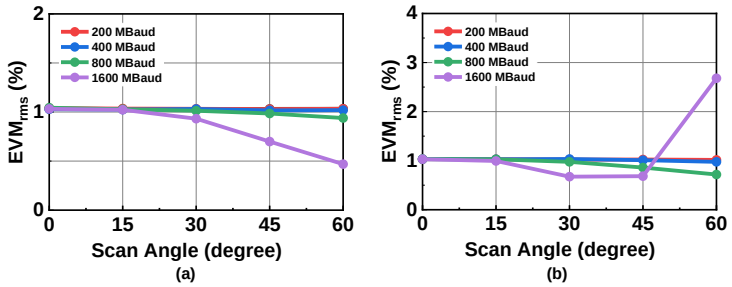

Figure 2.13: Simulated EVM versus scan angle of 64-QAM waveforms equalized with a 9-tap equalizer in (a) azimuth-plane scan, (b) diagonal scan.

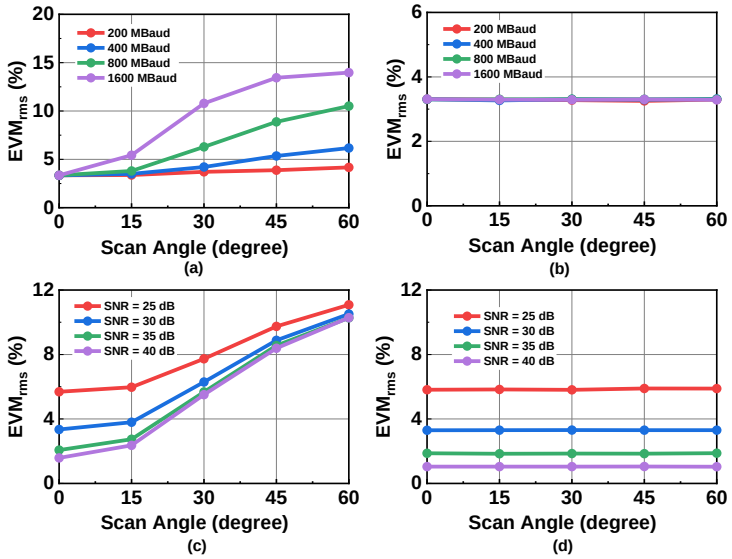

Figure 2.14: Simulated EVM versus scan angle of 64-QAM waveforms in azimuth-plane scan: (a) SNR = 30 dB versus symbol rate without equalizer, (b) SNR = 30 dB versus symbol rate with equalizer, (c) 800-MBaud waveform versus SNR without equalizer, (d) 800-MBaud waveform versus SNR with equalizer.

the largest columns (or rows) in a phased-array.

To simulate the effect of noise on the equalizer, additive white Gaussian noise is used in the model. Fig. 2.14(a) and (b) present the simulated EVM of 64-QAM waveforms with SNR = 30 dB versus scan angle and symbol rate, without and with a 17-tap equalizer, respectively. Compared to the ideal situation without noise (Fig. 2.12(a) and (b)), the EVM starts at higher values at 0° scan but saturates at almost the same levels at 60°. The equalized EVM remains flat for all scan angles, and the values are limited by the SNR at 3%. Fig. 2.14(c) and (d) presents

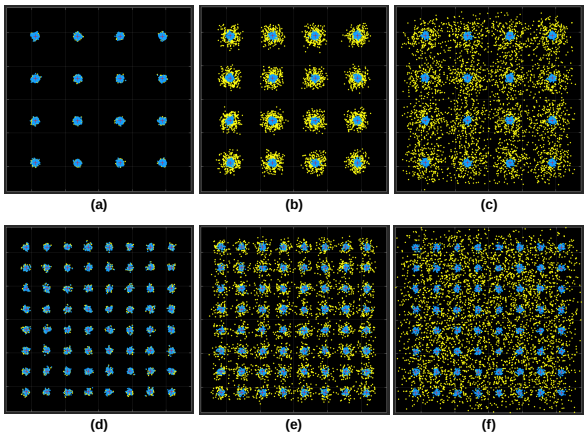

Figure 2.15: Simulated 16-QAM constellations when maximum ISI is (a) 0%, (b) 15%, (c) 30%, and 64-QAM constellations when maximum ISI is (d) 0%, (e) 15%, (f) 30%, with SNR = 30 dB

the EVM of 800-MBaud signals versus scan angle and SNR. It is obvious that SNR primarily affects the EVM when the ISI is small, and is a limiting factor on the best EVM achievable by the equalizer. In other words, the equalizer can only reduce the ISI but cannot alter the effects of the additive noise. The tap weights with added noise remain the same compared the ones calculated using MMSE method. Therefore, the same equalizer model can be applied to reduce the ISI regardless of the noise level.

Fig. 2.15 presents the constellations of 16-QAM and 64-QAM signals with SNR = 30 dB for different ISI values, where the yellow dots represent symbols before equalization and blue dots after equalization. The constellations visualize the increase in the EVM when the scan angle and symbol rate increase, and excellent equalization is achieved for all cases.

2.6 Measurements

A 256-element Ka-band phased-array is used as a demonstrator (Fig. 2.16(a) [10]). The phased-array is based on commercial 2×2 TX/RX beamformer chips, and all elements are combined using a 64:1 Wilkinson network, with a symmetrical and equi-distant layout between the phased-array common RF port and each of the beamformer chips. Furthermore, the 2×2

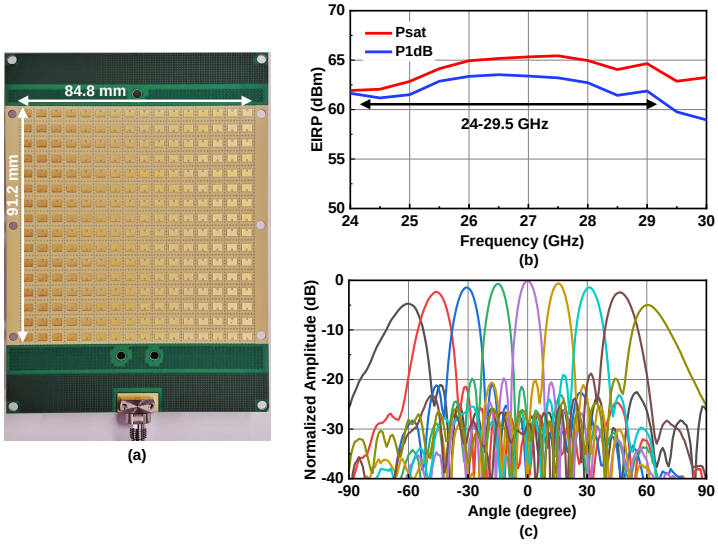

Figure 2.16: (a) A 256-element Ka-band phased-array using 64 2x2 beamformer chips and stacked-patch antennas (from [10]). (b) Measured EIRP at P_{1dB} and P_{sat} (from [10]). (c) Measured H-plane (azimuth) scanned patterns to $\pm 60^{\circ}$ at 27 GHz with 10-dB raised-cosine taper (from [10]).

beamformer chips are connected to the antennas using a symmetrical feed network, thereby ensuring uniformity throughout the entire phased array. This architecture has been presented before and is not repeated here for brevity [20], [22], [24–28]. The antennas are dual-stack microstrip patch antennas with probe feeds, and the chips are placed on the back side of the printed-circuit board (PCB). Details of the Renesas TX/RX 5G beamformer chip (F5280), printed-circuit board and phased-array antenna performance are presented in [10].

The 256-element phased-array was calibrated by measuring the S_{21} for each antenna element (turned on individually) in a far-field antenna chamber. Then the differences in S_{21} between the elements were compensated by using element-level gain and phase control [22], [28, 29]. The calibration results in an RMS amplitude error of 1 dB and an RMS phase error of 7.2°.

Complex modulation measurements were performed on the 256-element array in the TX mode with the measurement setup shown in Fig. 2.17(a). A Keysight M8195 arbitrary waveform generator (AWG) is used to generate 16-, 64- and 256-QAM modulated waveforms at 27 GHz

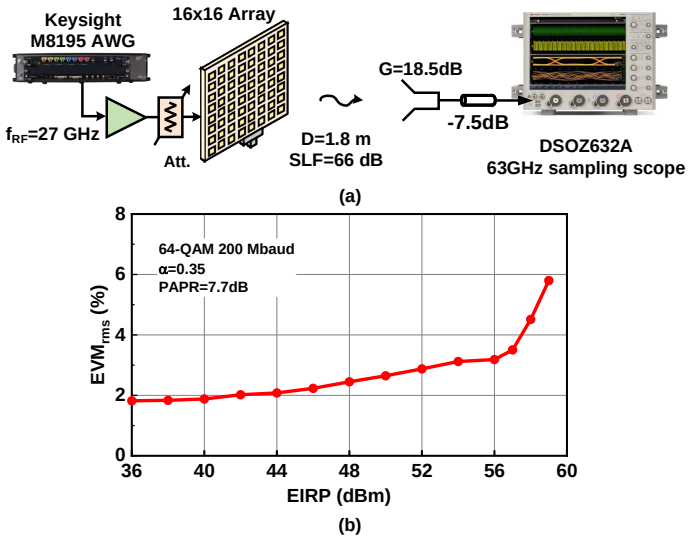

Figure 2.17: (a) EVM measurement setup for the Ka-band 16x16 phased-array. (b) Measured EVM versus EIRP at 27 GHz with 64-QAM 200 MBaud modulation at normal incidence (from [10]).

Table 2.1: Setup EVM for System Measurement

Modulation	200 MBaud	400 MBaud	800 MBaud	1600 MBaud
16-QAM EVM	1.90%	2.17%	2.54%	3.13%
64-QAM EVM	1.85%	2.22%	2.60%	3.20%
256-QAM EVM	1.99%	2.20%	2.53%	N/A

with a pulse shaping filter of $\alpha = 0.35$, resulting in a peak-to-average power ratio (PAPR) of 6.6-7.7-8.2 dB. The signal is then amplified, and the power at the phased-array input port is adjusted using an attenuator. The EVM of the instrumentation system (up to the phased-array input) measured with equalizer is summarized in Table 2.1.

A standard gain horn antenna is used on the RX side, and the signal is demodulated using the Keysight DSOZ632A 63-GHz oscilloscope running the Keysight 89600 Vector Signal Analysis (VSA) software. The equalizer tap number is set to 40 in the setting of the VSA software. Fig. 2.17(b) presents the measured phased-array EVM versus EIRP at normal incidence for a 27 GHz 64-QAM waveform. At an EIRP of 48 dBm (15 dB backoff), the output signal of the phased-array has high signal-to-noise-and-distortion ratio (SNDR) that yields optimal EVM

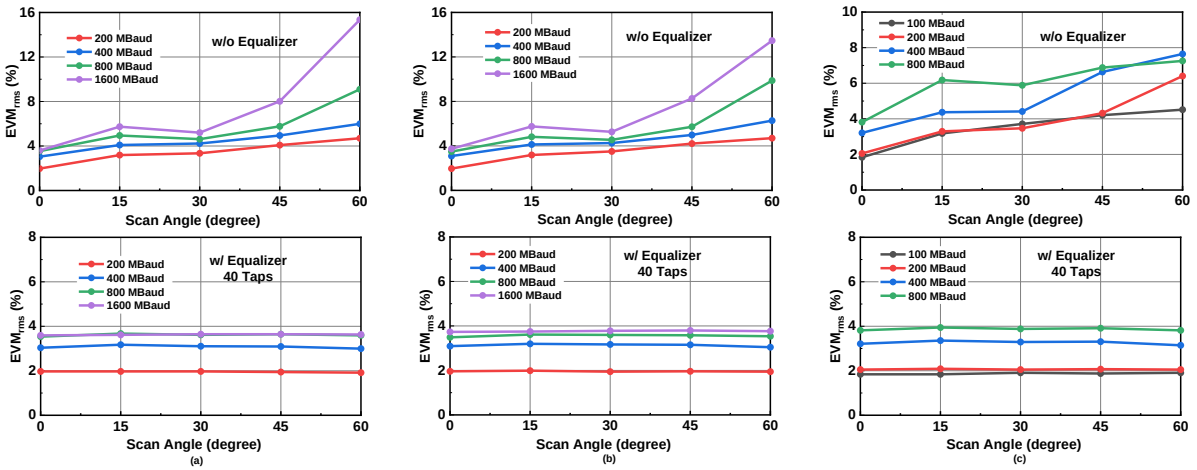

Figure 2.18: Measured EVM versus scan angle without and with equalizer of (a) 16-QAM, (b) 64-QAM, and (c) 256-QAM waveforms at EIRP = 48 dBm.

values of 2%. At this EIRP level, the power received by the DSO is -7 dBm, which is sufficient for accurate detection as the DSO can demodulate a -40 dBm 200 MHz waveform at 30 GHz with $<$ 1% EVM. All measurements are done at a center frequency of 27 GHz.

Fig. 2.18(a) presents the measured EVM RMS values for 16-QAM waveforms versus scan angle at different symbol rates. The measurements without the equalizer is performed by first running the equalizer at broadside, where no ISI is introduced by scanning, to take into account and normalize out the AWG, amplifier and cable loss frequency response. The system EVM, including the phased-array and DSO scope, starts at 2% for 200 Mbaud and is 3.8% at 1600 MBaud. Then the equalizer values are set on hold and the array is scanned.

As expected, the measured EVM increases both with scan angle and symbol rate. The measured curves do not match the simulated curves exactly because of other non-ideal effects in the phased-array and the measurement system setup, both of which are not modeled in the simulation. The EVM of the equalized signal in Fig. 2.18(a) remains constant across scan angles, which demonstrates that the ISI is eliminated by the equalizer, and the EVM for different symbol rates is solely determined by the system setup. Fig. 2.18(b) and Fig. 2.18(c) present similar results but for 64- and 256-QAM waveforms, respectively, and verify that the ISI introduced

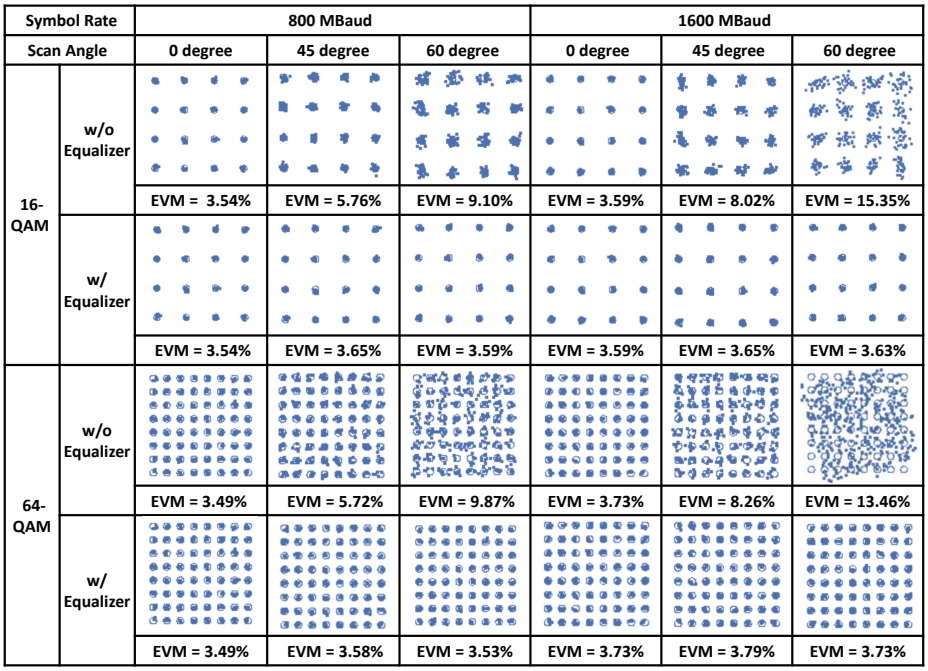

Figure 2.19: Measured constellations of 1600 Mbaud 16 and 64-QAM signals at different scan angles with and without equalizer (EIRP = 48 dBm).

by phased-array scanning can be equalized regardless of the modulation type. The 256-QAM 1600-MBaud waveforms cannot converge on the DSO and therefore results of 100 to 800-MBaud waveforms are shown. The measured constellations of 16- and 64-QAM waveforms with 800- and 1600-MBaud symbol rates at different scan angles are presented in Fig. 2.19. It is clear that the constellations remain the same with small errors for all cases with the equalizer.

The effect of phased-array tapering on EVM is also investigated. Fig. 2.20 presents the EVM of a 400-MBaud 64-QAM waveform with two levels of raised-cosine taper applied to the phased-array, compared to uniform excitation. Note that a taper is basically equivalent to a diagonal-plane scan, and can be easily equalized. All three curves, both with and without equalization, match with each other, and shows that amplitude tapering has no effect on the phased-array EVM.

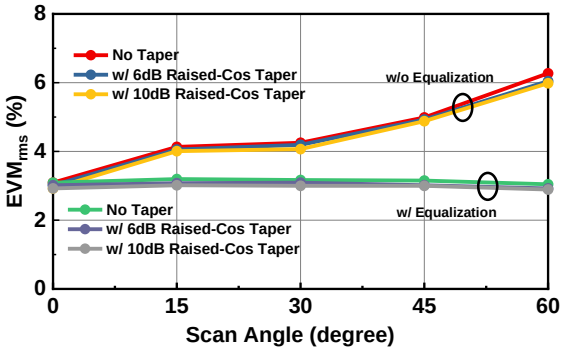

Figure 2.20: Measured 400 Mbaud 64-QAM signals versus scan angle when a 6-dB and a 10-dB raised-cosine taper are applied.

2.7 Conclusion

This paper presented the intersymbol interference created by a phased-array when scanned, which increases with symbol rate and scan angle and degrades the system EVM. It is shown that 5G phased-arrays do not need to employ complex and expensive TTD (true-time delay units), and 64-QAM and 256-QAM waveforms can be equalized using an N-tap equalizer. The equalizer can be implemented at baseband, or as commonly done today, in the modem using digital-signal processing. Measurements on a 16×16-element array with 200-1600 MBaud 64-QAM signals prove the validity of the analysis and excellent EVM is achieved over all scan angles with equalization.

2.8 Acknowledgment

The authors thank Kyocera International, San Diego, for assembling the arrays in their state of the art assembly line. The authors thank the Keysight team, Santa Rosa, for technical discussions and state-of-the-art equipment.This work was supported in part by the UCSD Center for Wireless Communications and in part by the by the Semiconductor Research Corporation (SRC) and The Defense Advanced Research Projects Agency (DARPA) under the JUMP program

with a DSSP addition.

Chapter 2, in part, is a reprint of the material as it appears in: Y. Yin, Z. Zhang, T. Kanar, S. Zihir and G. M. Rebeiz, "A 24-29.5 GHz 256-Element 5G Phased-Array with 65.5 dBm Peak EIRP and 256-QAM Modulation," *2020 IEEE/MTT-S International Microwave Symposium (IMS),* Los Angeles, CA, USA, 2020, pp. 687-690, doi: 10.1109/IMS30576.2020.9224031. The dissertation author was the co-author of this paper.

Chapter 2, in full, is a reprint of the material as it may appear in: Z. Zhang, Y. Yin and G. M. Rebeiz, "Intersymbol Interference and Equalization for Large 5G Phased Arrays With Wide Scan Angles," in *IEEE Transactions on Microwave Theory and Techniques,* vol. 69, no. 3, pp. 1955-1964, March 2021, doi: 10.1109/TMTT.2020.3048005. The dissertation author was the primary investigator and author of this paper.

Chapter 3

System-Level Analysis and Measurements of Thinned Randomized 27-29 GHz TX and RX Arrays for 5G Communications and for Radars with Low Sidelobe Levels

3.1 Introduction

Microwave and millimeter-wave radars are an essential component of automotive sensors, and of any air-to-air collision-avoidance sensor suite. For automotive systems, the radars are built using few transmit and receive antennas (4 to 16), and digital beamforming is used to determine the angle of arrival of several targets (vehicle and pedestrian radar returns). For such applications, it is imperative to build systems with low sidelobe levels so as to have high discrimination between the targets and clutter. On the other hand, air-to-air radars typically employ a much larger number of elements (64 to 1024) due to their longer range and higher performance requirements [45], [46], but still have stringent requirements on sidelobe levels (Fig. 3.1(a)). These arrays are also used

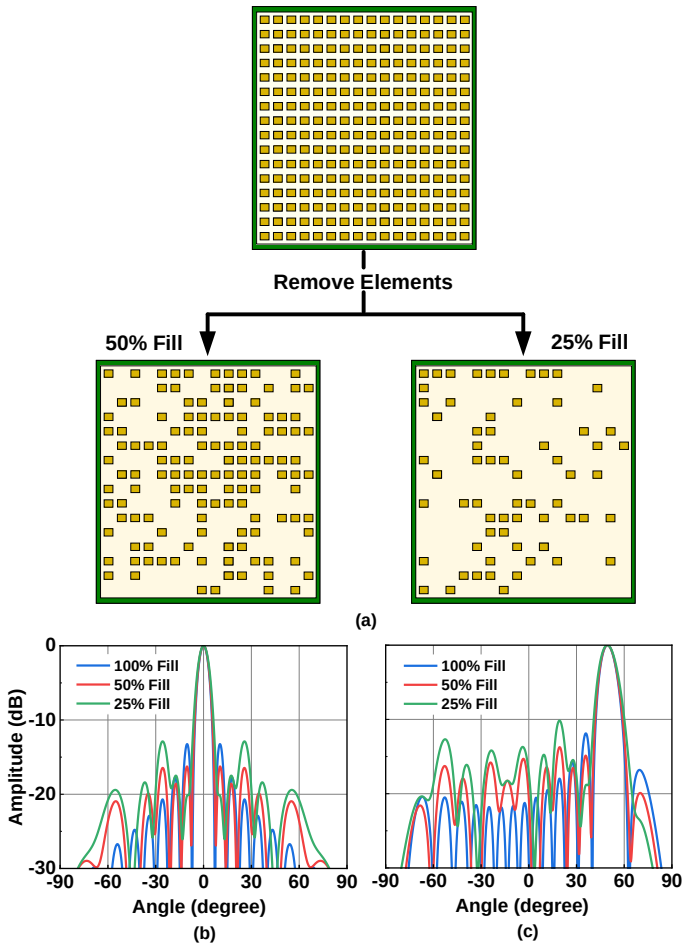

Figure 3.1: (a) Illustration of thinned randomized array, and simulated patterns of arrays with R_{fill} = 1, 0.5, 0.25 at (b) broadside, (c) 50° scan.

for mm-wave 5G communication systems at 24-29 GHz and 37-42 GHz and any reduction in the number of array elements can also be very beneficial for system cost.

Lately, advances in SiGe and CMOS technologies have allowed for a drastic reduction in the cost of transmit/receive modules, and silicon chips with multiple channels are now available at low cost for X, Ku, Ka-bands, and for automotive radars at 24 GHz and 77 GHz [16, 19, 24, 47–49]. Still, it is hard and relatively expensive to build imaging radars and large 5G communication arrays containing hundreds and even thousands of elements, especially for automotive applications where cost constraints are severe. The use of randomized grouping of elements and of overlapping sub-array techniques have been proposed to reduce the number of elements in a large aperture,

and to lower the cost of phased-arrays [50]. These solutions typically come with limited scan range which may not be allowed for large-volume scans.

This paper investigates the use of thinning and randomized arrays to greatly reduce the cost of large-aperture radars while still keeping high system performance. Thinning has been previously investigated, and results in increased sidelobes and reduced antenna gain and requires various optimization algorithms to maintain well-control sidelobe levels [51–55]. For communication systems, the increase in sidelobe levels may not meet the requirements for SATCOM and for base-stations applications. However, if applied correctly, thinning can result in an excellent solution for radars and 5G communication systems while still keeping a high fidelity for the main system parameters, such as bandwidth, beamwidth, sidelobes and scan volume.

3.2 Thinned Randomized Arrays

Fig. 3.1(a) presents 256-element antenna arrays spaced at 0.5λ in the x and y directions, but randomly thinned for an effective filling factor of 50% and 25% (R_{fill} = 0.5 and 0.25). The thinned arrays occupy the same area as the filled arrays as this is important for the 3-dB beamwidth. The random arrays are generated by starting with a 256-element array, randomly removing a set number of elements in the array, resulting in a remaining elements of $256 \times R_{fill}$, and simulating the patterns of generated arrays. In general, 5000-10,000 configurations are done in MATLAB and the random arrays with better sidelobes at broadside are selected. The patterns for R_{fill}=0.5 and 0.25 and shown in Fig. 3.1(b) and (c) at broadside and for a scan angle of 50° in the azimuth plane (due to randomization, the vertical plane scans result in similar patterns and is not shown). Note that the main beam is unaffected by the array thinning even with R_{fill} = 0.25. Also, grating lobes do not appear for any scan angle. For R_{fill} = 0.5, and for the best MATLAB-generated configuration, the maximum sidelobe level across the 2-D pattern is -15.5 dB and is lower than the typical -13.6 dB found for a uniformly-illuminated array. For R_{fill}=0.25,

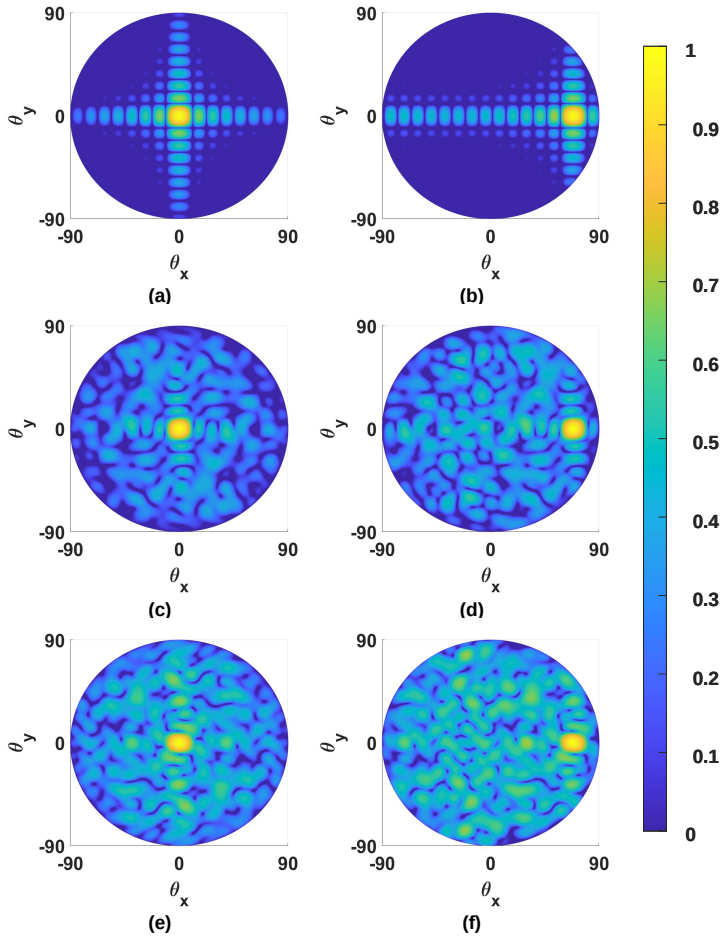

Figure 3.2: Simulated 2-D pattern of 100% filled array at (a) broadside, (b) 45° scan, and 50% filled array at (c) broadside, (d) 45° scan, and 25% filled array at (e) broadside, (f) 45° scan.

the maximum sidelobe level increases to -12.9 dB, but the peak sidelobe can appear anywhere in the pattern for a random array. In short, thinned random arrays having the same area as filled arrays do not suffer from any degradation in the 3-dB beamwidth or from peak sidelobe levels, but they do have many more sidelobes in the entire space than periodic arrays.

The performance of thinned random arrays is clearly seen when the 2-D patterns are plotted for broadside and 50° scan angles (Fig. 3.2). Note that the sidelobes that initially appear on the E and H-planes in a filled periodic array are now spread over the entire solid angle in randomly distributed locations. The increase in the number of sidelobes reduces the array directivity, as

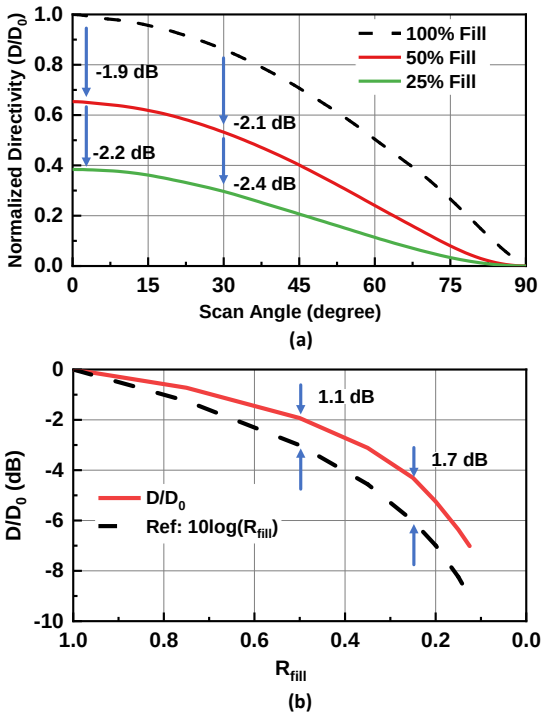

Figure 3.3: (a) Simulated normalized directivity of thinned randomized arrays (a) with R_{fill} = 1, 0.5, 0.25 versus scan angle, (b) versus R_{fill} at broadside.

expected.

Fig. 3.3(a) presents the simulated directivity of thinned random arrays with $R_{fill} = 0.5$ and $R_{fill} = 0.25$ versus scan angle, normalized to the directivity of a filled array with the same overall size and a uniform spacing of 0.5λ. The directivity of a filled array with uniform illumination can be expressed as:

$$D = D_0 cos^n(\theta_0) \tag{3.1}$$

where

$$D_0 = 4\pi A/\lambda^2 \tag{3.2}$$

and θ_0 is the scan angle [56]. n denotes the effect of the antenna element factor and impedance mismatch. For well-designed array, $n = 1.1 - 1.3$, and for this analysis, we will take an ideal array with $n = 1$. The directivities of thinned arrays at broadside for $R_{fill} = 0.5$ and $R_{fill} = 0.25$ are

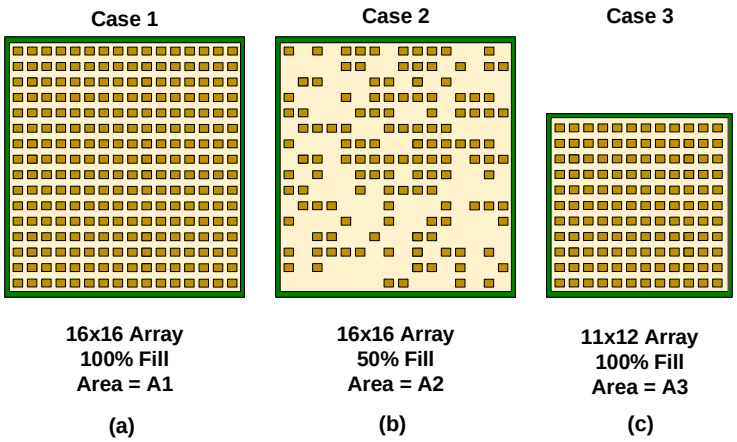

Figure 3.4: (a) Uniform, fully populated array; (b) thinned randomized array with the same aperture as (a) and 50% fill; (c) Uniform, fully populated array with the same number of elements as (b) and a smaller aperture.

$0.64D_0$ and $0.38D_0$, respectively, and are 1.9 dB and 4.1 dB lower than the filled array. However, they are also 1.1 dB and 1.9 dB higher than a fully populated array with the same number of elements but a smaller aperture ($D = D_o R_{fill}$). Therefore, if higher sidelobes can be tolerated, then a random array with $R_{fill} = 0.5 - 0.25$ can result in a directivity enhancement as compared to a fully-populated array with the same number of elements. One of the main reasons is that the antenna element factor has a higher directivity when the array is thinned as compared to a fully populated array. Fig. 3.3(b) presents the directivity at broadside of a thinned array versus R_{fill}, and it is seen that it is always higher than $D_0 R_{fill}$.

The directivity can be written as (Fig. 3.4):

$$Case\ 1 : D_1 = 10logN + G_{el} \tag{3.3}$$

(uniform array with a $\lambda/2 \times \lambda/2$ grid, where $G_{el} = 4\pi A/\lambda^2 = 5$ dB)

$$Case\ 2 : D_2 = 10log(NR_{fill}) + G'_{el} \tag{3.4}$$

(thinned random array with G'_{el} = 6.5-7 dB and reduced number of elements, having same aperture

as Case 1)

$$Case\ 3 : D_3 = 10log(NR_{fill}) + G_{el} \tag{3.5}$$

(uniform array with G_{el} = 5 dB having a reduced number of elements and a smaller aperture than Case 1). It is clear that $D_1 > D_2 > D_3$ and $A_1 = A_2 > A_3$ as shown in Fig. 3.4.

3.3 Thinned Randomized Arrays for Radar Applications

The use of thinned random arrays in radar applications can greatly lower the number of required Tx and Rx channels, but at a cost of reduced directivity and higher sidelobes in the entire 2-D space. This is considered below:

3.3.1 EIRP

For R_{fill} = 0.5 and 0.25, the EIRP is expected to be reduced by a factor of 2-4 (reduced number of elements) and also by the reduction in directivity to $0.64D_0$ and $0.38D_0$, respectively. This results in an EIRP reduction of 4.9-10.1 dB for R_{fill} = 0.5-0.25. In lower power radars transmitting 5-15 dBm/element, this is not an issue as the element transmit power can be increased by 4.9-10.1 dB to compensate for the EIRP drop. Also, note that only 50% and 25% of the elements are populated which leaves a lot of space for heat removal. And, it is well known that medium power amplifiers with P_{sat} of 15-25 dBm are more efficient than low power amplifiers with P_{sat} of 7-12 dBm, especially at mm-wave frequencies. The EIRP equations can be written as:

$$Case\ 1 : EIRP_1 = 20logN + G_{el} + P_{el} \tag{3.6}$$

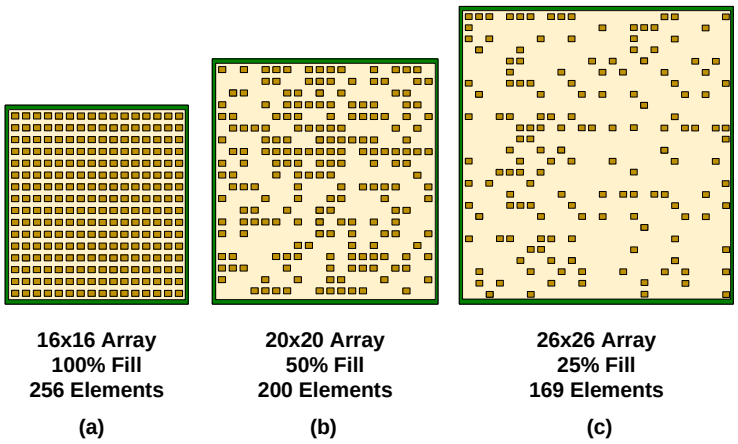

Figure 3.5: Arrays with R_{fill} = 1, 0.5, 0.25 and the same antenna gain: (a) uniform array; (b) 20×20 array and R_{fill} = 0.5; (c) 26×26 array and R_{fill} = 0.25.

$$\begin{aligned} &Case\ 2: \\ &EIRP_2 = 20log(NR_{fill}) + G'_{el} + P'_{el} \end{aligned} \tag{3.7}$$

and for $EIRP_1 = EIRP_2$, we must have

$$P'_{el} = P_{el} - 20log(R_{fill}) + (G_{el} - G'_{el}) \tag{3.8}$$

3.3.2 Receive Gain

For R_{fill} = 0.5 and 0.25, the thinned array directivity is $D = 0.64D_0$ and $0.38D_0$, respectively, as compared to a fully populated array (D_0). It is clear that in thinned arrays, the received power is reduced and system performance is degraded as the RX channels have the same noise figure (NF) for both the filled and thinned arrays ($P_R = SA_{eff}$, where S is the incident power density, $A_{eff} = (\lambda^2/4\pi)D$, and NF remains the same). One solution is to increase the aperture area to compensate for this gain reduction. For $R_{fill} = 0.5$ and $D = 0.64D_0$, one needs to increase the receive aperture for a 256-element array with an aperture of $64\lambda^2$ ($8\lambda \times 8\lambda$) to $100\lambda^2$ ($10\lambda \times 10\lambda$), and employing 200 RX modules to achieve the same gain (Fig. 3.5(a), (b)).

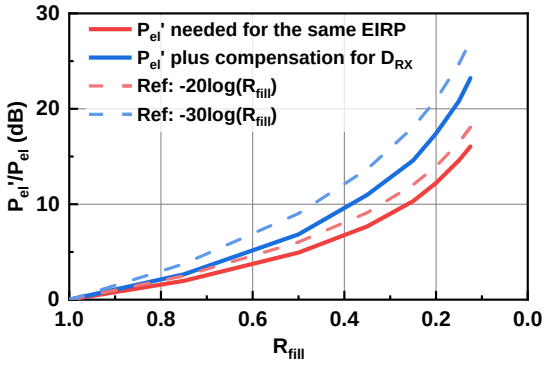

Figure 3.6: P'_{el} required to get the same EIRP versus R_{fill} as a fully populated array with the same aperture, and P'_{el} plus the compensation for drops in RX directivity.

For $R_{fill} = 0.25$ and $D = 0.38D_0$, the aperture area required is $169\lambda^2$ and with 169 RX modules (Fig 3.5(c)). Note that even with the increased area, the total number of RX channels will still be lower than a filled array.

The increase in aperture area will change the RX beamwidth and may not be ideal for radar applications. A better way is to increase the transmit EIRP to compensate for the reduction in receive gain (while keeping the same RX aperture area). In this case, the EIRP should be increased by an additional 1.9-4.1 dB as compared to (8) for R_{fill} = 0.5-0.25, and this results in an increase in the power per element by the same factor. Fig. 3.6 presents the P'_{el} required to reach the same EIRP as the fully populated array, and to also compensate for the drop in the receive gain. For R_{fill} = 0.5 and 0.25, the radiated power of each element needs to be 6.8 and 14.6 dB higher, respectively, to achieve the same return power for radar applications. However, note that the required power per element for R_{fill} = 0.5-0.25 is still 2.2-3.4 dB lower than what is needed if smaller fully-populated arrays are used with the same number of elements (transmit power needs to be increased as $30Log(R_{fill})$).

3.3.3 Sidelobe Levels

The high sidelobe levels, especially for thinned arrays with $R_{fill} = 0.25$, cannot be mitigated when considering one-way patterns, which may be problematic for transmit communication systems with a mandated pattern mask. Still, as shown in Fig. 3.4, one can employ thinned arrays in the receive mode and with reduced number of elements, provided that the RX system can tolerate higher sidelobe levels (low interference scenarios). This may be useful for SATCOM applications.

For radars, with TX and RX systems, one can choose complementary thinned TX and RX arrays, such that the sidelobes of the TX array are greatly reduced by nulls in the RX array patterns. As is well known, the radar equation contains $G_T(\theta,\phi) \times G_R(\theta,\phi)$ and what is most important is the multiplication of both of these patterns. A large search is done in MATLAB to find complementary array configurations, as the sidelobe levels should not be reduced only on the principal planes, but everywhere in the 2-D patterns. In general, a 50,000 TX$\times$RX pattern search is done and the best TX and RX combinations are chosen.

Fig. 3.7 presents complementary arrays with $R_{fill} = 0.5$. Due to pattern optimization, both the TX and RX patterns have a peak sidelobe level of less than -15 dB, resulting in a return TX $\times$ RX peak sidelobe level of -33 dB, which is lower than the -27 dB return sidelobe level expected from a uniform fully populated array. Fig. 3.7(d) presents the TX and RX patterns scanned to $\theta_0 = 45^\circ$ and $\phi_0 = 45^\circ$. The complementary design is obvious since the peaks of some sidelobes in the TX array align with the nulls of the RX array, resulting in a peak return sidelobe level of -31 dB. Fig. 3.7(e) and (f) presents the return patterns in the 2-D space, for both broadside and 45° scan, showing low sidelobes over the entire visible space. The peak sidelobes can be found next to the main beam in elevation at -33 dB and -31 dB for broadside and 45° scan, respectively.

Fig. 3.8 presents the complementary arrays with $R_{fill} = 0.25$ and their patterns in both 1-D and 2-D space. Due to aggressive thinning, the sidelobe levels of both the TX and RX arrays

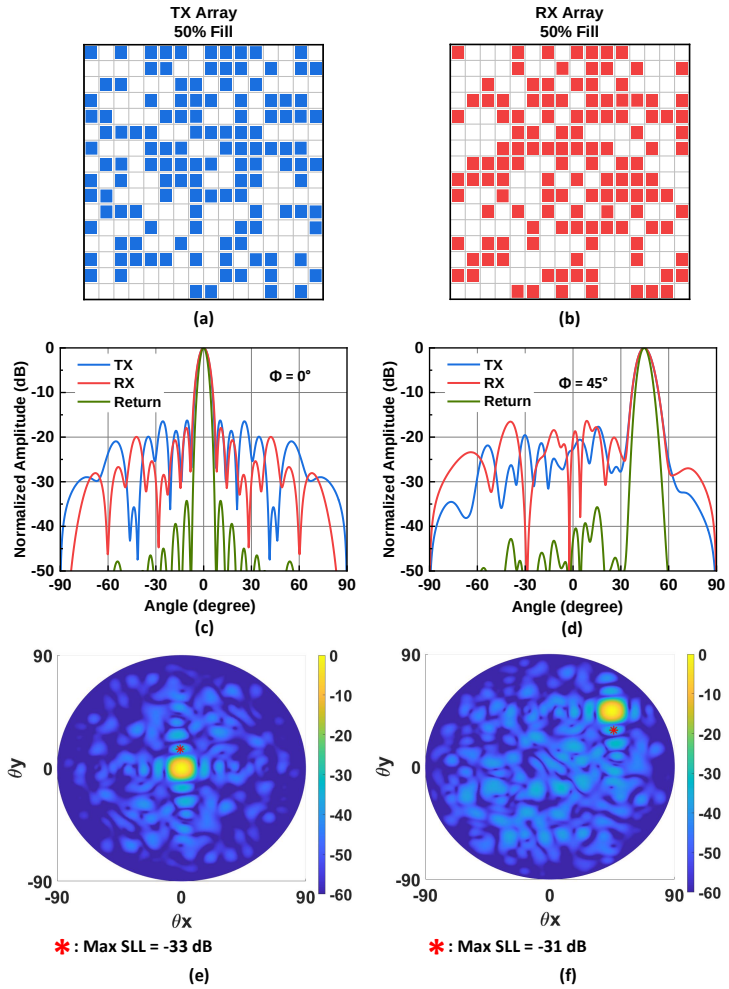

Figure 3.7: Optimized (a) TX and (b) RX thinned randomized array configuration with R_{fill} = 0.5; simulated TX, RX and TX×RX patterns at (c) broadside and (d) $\theta_0 = 45°$,$\phi_0 = 45°$ scan; simulated 2-D TX×RX patterns at (c) broadside and (d) $\theta_0 = 45°$,$\phi_0 = 45°$ scan.

are significantly higher than R_{fill} = 0.5. Therefore, the effect of the complementary patterns is even more clear, resulting in sidelobes of -30 dB at around θ = 28° in the elevation plane for broadside, and at -26 dB for 45° scan far away from the main beam, showing that low sidelobe levels can be achieved at all scan angles. Note that sidelobe levels far away from the main beam are easy to remove in radar systems due to their significant difference in time of arrival.

A taper can be applied to randomly thinned arrays to reduce sidelobe levels. Fig. 3.9 presents the patterns with R_{fill} = 0.5, with a -7 dB raised-cosine taper and -25 dB Taylor taper

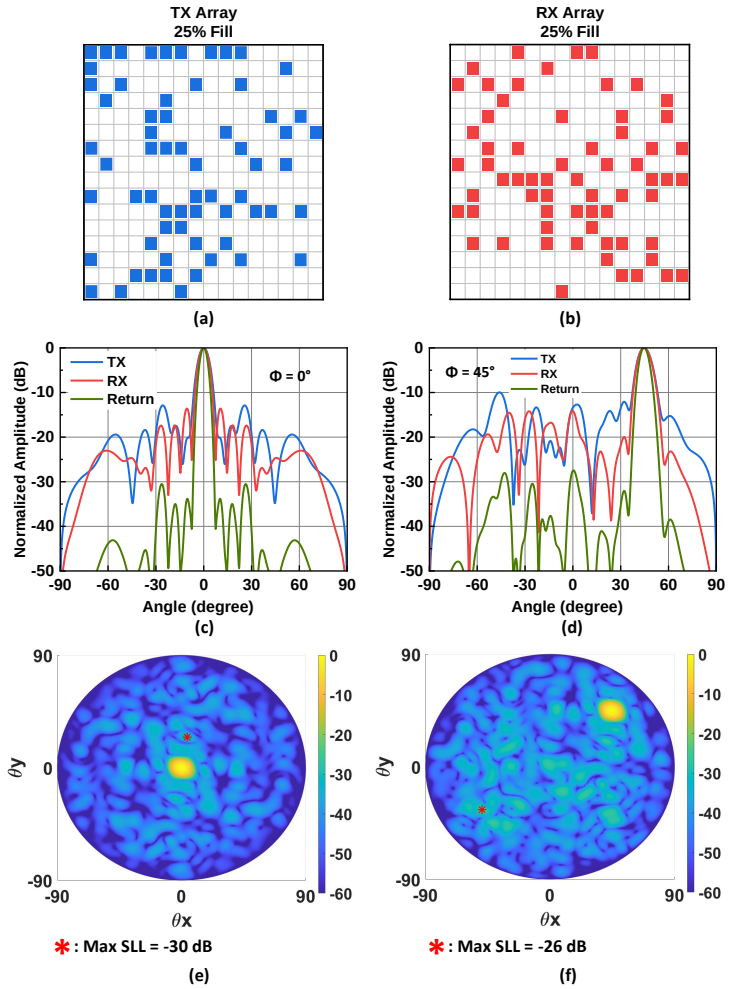

Figure 3.8: (a) TX and (b) RX thinned randomized array configuration with $R_{fill} = 0.25$; simulated TX, RX and TX×RX patterns at (c) broadside and (d) $\theta_0 = 45°$,$\phi_0 = 45°$ scan; simulated 2-D TX×RX patterns at (c) broadside and (d) $\theta_0 = 45°$,$\phi_0 = 45°$ scan.

applied. The peak sidelobe level in the principal plane decreases from -34 dB to -48 dB, due to the taper. However the sidelobe levels in the full 2-D space are dominated by the random discretization and cannot be reduced by tapering. Therefore, the peak sidelobe of the return pattern is not located on the principal planes, and the resulting sidelobe level is -40 dB in the 2-D space, which is still 6 dB lower than uniform excitation. Fig. 3.9(c) and (d) present the patterns with -25 dB Taylor taper. The patterns show that only the sidelobes close to the main beam are further reduced to -50 dB, but the highest sidelobe is still at around -40 dB.

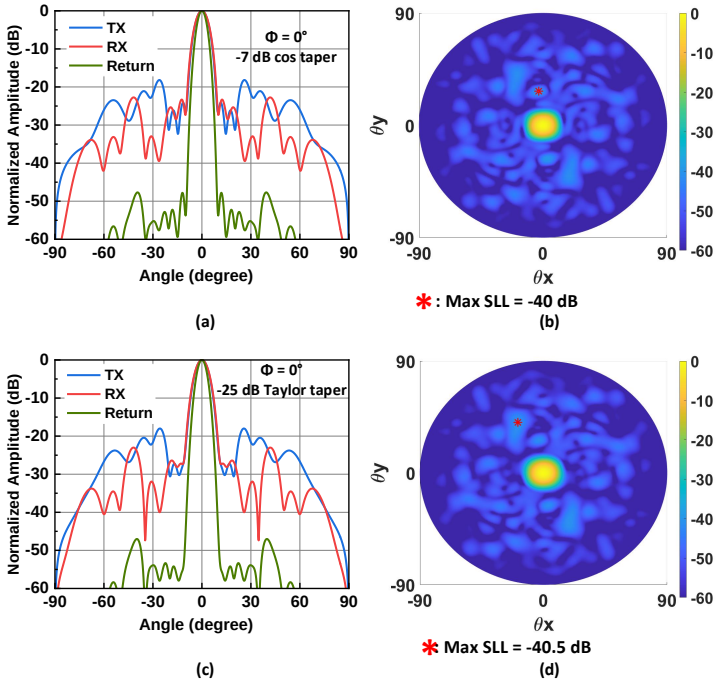

Figure 3.9: Simulated patterns with R_{fill} = 0.5 and -7 dB raised-cosine taper in (a) $\phi_0 = 0^\circ$ plane and (b) in 2-D space; and simulated patterns with R_{fill} = 0.5 and -25 dB Taylor taper in (c) $\phi_0 = 0^\circ$ plane and (d) in 2-D space.

In conclusion, the reduction in the number of elements and in antenna gain can be mitigated by a higher element transmit power (which in turn can result in a more efficient system), and the increase in sidelobes is mitigated by choosing complementary TX and RX arrays and by applying an amplitude taper to further reduce the close-in sidelobes. This results in radar systems with greatly thinned arrays in both TX and RX apertures, and with the same system parameters (beamwidth, scan angle, low sidelobes, similar SNR) as fully-populated arrays but with a reduction of 2-4$\times$ in the number of elements.

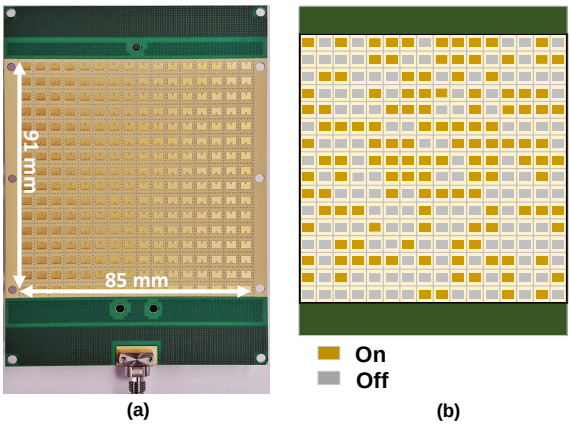

Figure 3.10: (a) Photo of the 16×16 Ka-band TRX phased array. (b) Illustration of turning off channels to simulate effects of thinned arrays ($R_{fill} = 0.5$ shown).

3.4 Measurements

The thinned randomized array is demonstrated using a fully populated 16×16 Ka-band TRX phased array by turning on different channels to emulate the thinning (Fig 3.10(a) and (b)). A 256-element phased array based on commercial 2×2 TRX SiGe beamformer chips is used for this experiment. The antenna elements are combined using a 64:1 Wilkinson network, with a symmetrical and equi-distant layout between the phased array's common RF port and each of the beamformer chips. The 2×2 SiGe beamformer chips are connected to the antennas using a symmetrical feed network, therefore ensuring uniformity throughout the entire phased array [20, 22, 26, 27]. The antenna utilizes a stacked-patch structure with a grid of 5.3 mm (0.5λ at 28 GHz) in the H-plane (azimuth) and 5.7 mm (0.53λ at 28 GHz) in the E-plane. The array is capable of scanning up to ±60° in the azimuth and ±50° in the elevation planes, and has a measured EIRP of 63 dBm and 65 dBm at its P_{1dB} and P_{sat}, respectively [10].

The phased array is first calibrated at 28 GHz by measuring the S_{21} of each TX and RX channel (turned on individually) in a far-field antenna chamber. The differences in amplitudes and phases between different elements are compensated by the VGA and phase shifters at each element, respectively. The resulting RMS amplitude and phase errors after calibration are less

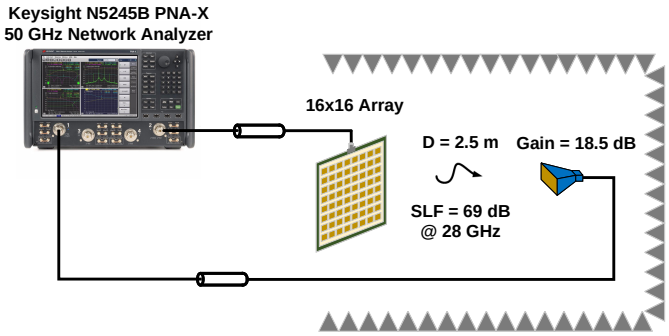

Figure 3.11: Setup for pattern, EIRP and RX electronic gain measurements.

than 1 dB and 8°, respectively, for both TX and RX channels.

3.4.1 Patterns

Both the TX and RX patterns are measured in the far-field chamber using the Keysight N5245B 50 GHz vector network analyzer and a standard gain horn (Fig. 3.11). All patterns are shown at 28 GHz unless otherwise noted.

Fig. 3.12(a) and (b) presents the measured H-plane (azimuth) broadside patterns with uniform excitation using the complementary configurations with $R_{fill} = 0.5$ and $R_{fill} = 0.25$ shown in Fig. 3.7 and Fig. 3.8, respectively. The TX×RX patterns are then calculated by multiplying the TX and RX patterns of each configuration. Without taper, the TX×RX patterns exhibit a peak of sidelobe level of -33.9 dB for R_{fill} = 0.5 and -30.6 dB for R_{fill} = 0.25, which is close to the simulated values of -34.4 dB and -30.7 dB, respectively, verifying the complementary design. Fig. 3.12(c) and (d) present the same set of patterns with -7 dB raised-cosine taper. The resulting peak return sidelobe levels in the azimuth plane are -46.6 dB and -37.1 dB for R_{fill} = 0.5 and R_{fill} = 0.25, respectively. Due to more aggressive thinning, the sidelobes of the the R_{fill} = 0.25 case are quickly dominated by random sidelobes away from the main beam. Although very low sidelobe levels can be achieved in the H-plane, the peak sidelobes reside away from the principal planes for both cases. The peak sidelobe levels are -40 dB and -31.5 dB for R_{fill} = 0.5 and 0.25, respectively, according to simulations. Therefore, with only half the elements and

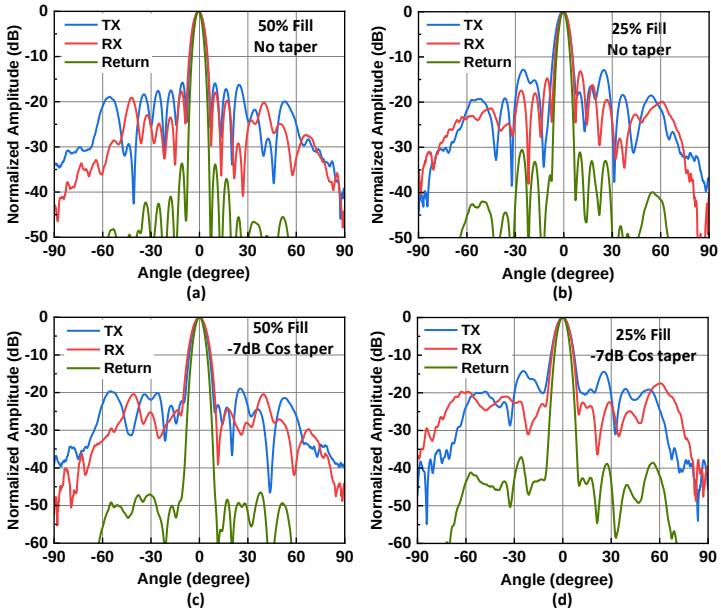

Figure 3.12: Measured patterns at 28 GHz at broadside with (a) R_{fill} = 0.5 and uniform excitation, (b) R_{fill} = 0.25 and uniform excitation, (c) R_{fill} = 0.5 and -7 dB raised-cosine taper, (d) R_{fill} = 0.25 and -7 dB raised-cosine taper.

beamformer chips, the thinned randomized array can have comparable performance to a fully populated array with -7 dB raised-cosine taper for radar applications. Note that the one-way patterns for R_{fill} = 0.25 have high sidelobes, even with -7 dB taper, and may not be acceptable for certain communication systems. However, the R_{fill} = 0.5 patterns are excellent and may be a great compromise for communication systems.

The -3 dB beamwidths of the thinned arrays with R_{fill} = 0.5 and 0.25 remain similar to the fully populated array. For R_{fill} = 0.5 and 0.25, the TX and RX beamwidths are 6.6° and 7° with uniform excitation, and only 0.2° to 0.6° wider than the 6.4° beamwidth of a fully populated array. With -7 dB raised-cosine taper, the -3 dB beamwidth are 7.2°, 7.4° and 8° for R_{fill} = 1, 0.5, and 0.25, respectively.

Fig. 3.13 presents the patterns with R_{fill} = 0.5 and R_{fill} = 0.25 scanned from 30° to 60°, with -7 dB raised-cosine taper. Due to the pattern of the microstip antennas at wide angles, the amplitude of the main beam is compressed at large scan angles, resulting in a higher sidelobe

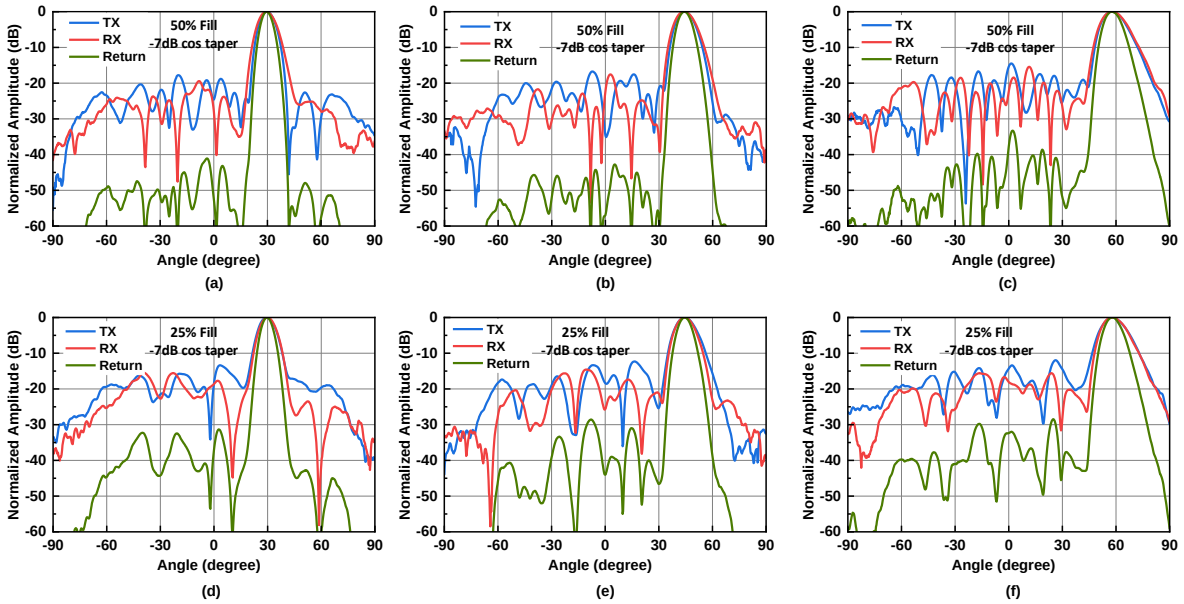

Figure 3.13: Measured patterns at 28 GHz with R_{fill} = 0.5 and -7 dB raised-cosine taper at (a) 30° (b) 45° (c) 60° scan, and patterns with R_{fill} = 0.25 and -7 dB raised-cosine taper at (a) 30° (b) 45° (c) 60° scan

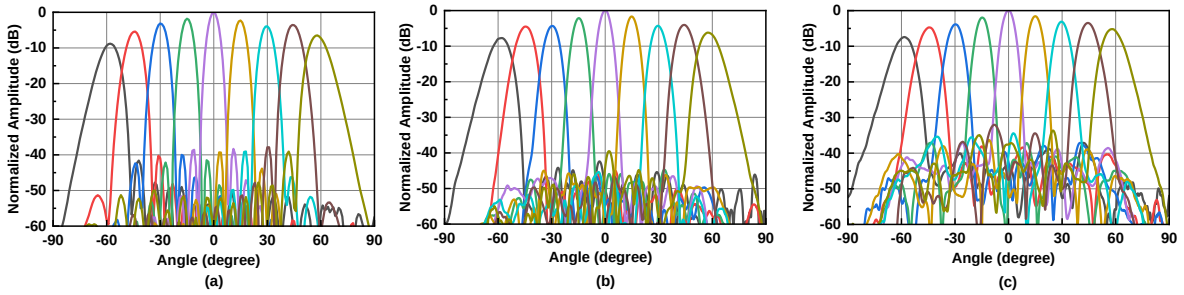

Figure 3.14: Measured TX×RX patterns of (a) R_{fill} = 1, (b) R_{fill} = 0.5, (c) R_{fill} = 0.25 arrays with -7 dB raised-cosine taper scanned from -60° to 60°.

level. Overall, the patterns maintain consistent sidelobe levels across all scan angles. Because of the randomness of antenna locations, no grating lobes emerge even at 60° scan.

Fig. 3.14(a) presents the measured TX×RX patterns of the fully populated 16×16 array with -7 dB raised-cosine taper, scanning from -60° to 60° at 28 GHz. The patterns show higher sidelobe levels in the H-plane compared to the thinned arrays with R_{fill} = 0.5 (Fig. 3.14(b)). In general, R_{fill} = 0.5 array shows similar sidelobe levels over the entire 2-D space compared to the

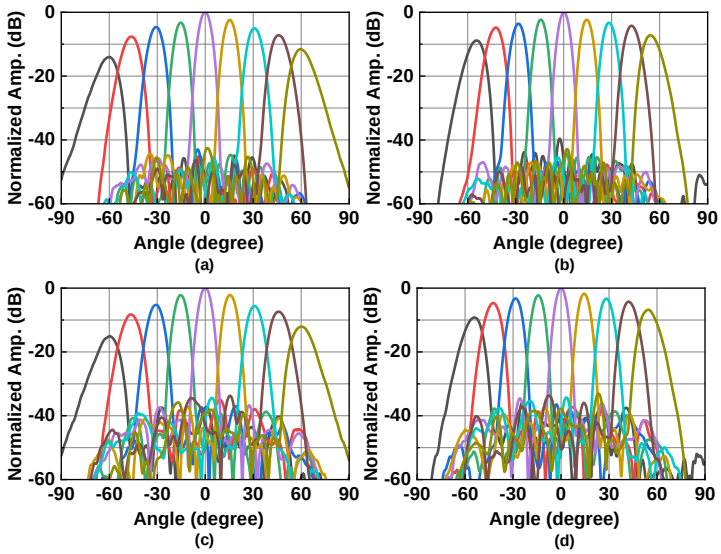

Figure 3.15: Measured TX×RX patterns of R_{fill} = 0.5 array with -7 dB raised-cosine taper scanning from -60° to 60° at (a) 27 and (b) 29 GHz; Measured TX×RX patterns of R_{fill} = 0.25 array with -7 dB raised-cosine taper scanned from -60° to 60° at (c) 27 and (d) 29 GHz

fully-populated array. The array with R_{fill} = 0.25 shows higher sidelobe levels since the sidelobes created by random discretization are unaffected by taper. Note that for a fully populated array, the highest sidelobe is always next to the main beam, while for the thinned randomized array, it is located farther from the main beam, and its radar return can be removed in post-processing. As shown in Fig. 3.14, the -3 dB beamwidth of the thinned arrays remain close to the fully populated array even at large scan angles. At 60° scan with -7 dB raised-cosine taper, the -3 dB beamwidth of the TX × RX pattern is 8.4° for the fully active array, and 9.4° for both R_{fill} = 0.5 and 0.25.

The complementary thinned array pair also work across a wide range of frequencies. Fig. 3.15 presents the TX×RX patterns from -60° to 60° at 27 GHz and 29 GHz, for R_{fill} = 0.5 and R_{fill} = 0.25 with -7 dB raised-cosine taper. All patterns show similar sidelobe levels as 28 GHz. This is an instantaneous bandwidth measurement, and the phase gradient is set at 28 GHz, resulting in minor beam squinting at 27 and 29 GHz.

In the case where higher directivity in the RX array is desired to improve the signal to noise ratio, a RX array with R_{fill} = 0.5 can be paired with a TX array with R_{fill} = 0.25. Fig.

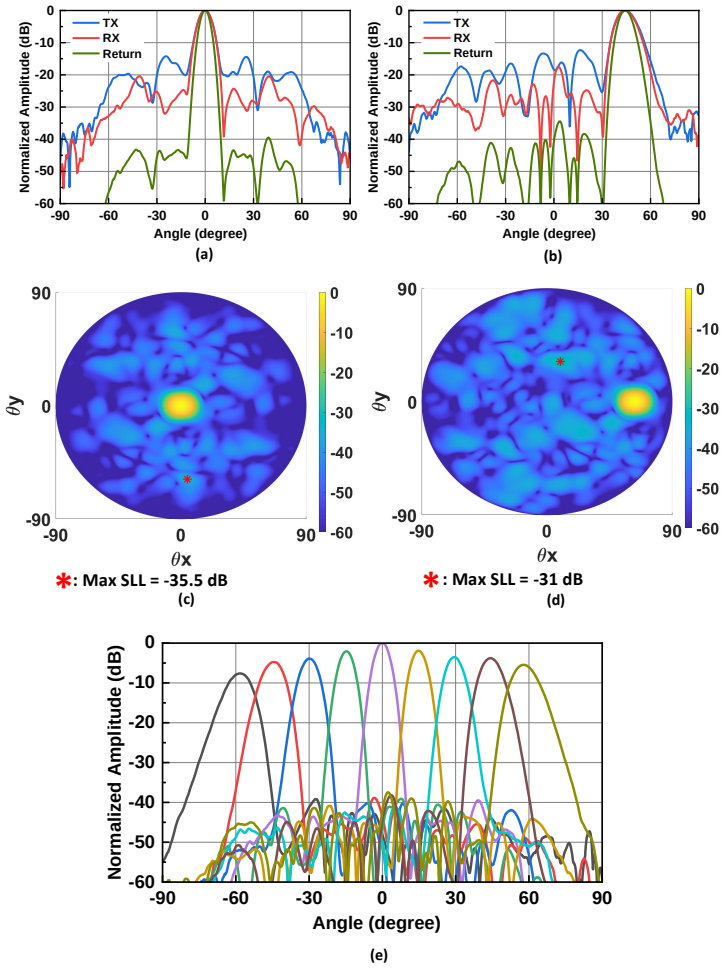

Figure 3.16: Measured patterns with R_{fill} = 0.25 for TX and 0.5 for RX and -7 dB raised-cosine taper at (a) broadside (b) 45° scan, and simulated 2-D pattern with R_{fill} = 0.25 for TX and 0.5 for RX and -7 dB raised-cosine taper at (c) broadside (d) 45° scan. (e) Measured TX×RX patterns from -60° to 60° scan.

3.16(a) and (b) present the measured patterns of such a combination at broadside and for a scan angle of 45° in the H-plane. The measured patterns show equally low sidelobe levels in the H-plane compared to the previous results, and the simulation shows low sidelobe levels in the entire 2-D space (Fig. 3.16(c),(d)). The measured patterns also show low sidelobe levels across a wide scan range (Fig. 3.16(e)). Therefore, a wide combination of R_{fill} can be used for the TX and RX arrays (with complementary designs) and will result in low sidelobe levels.

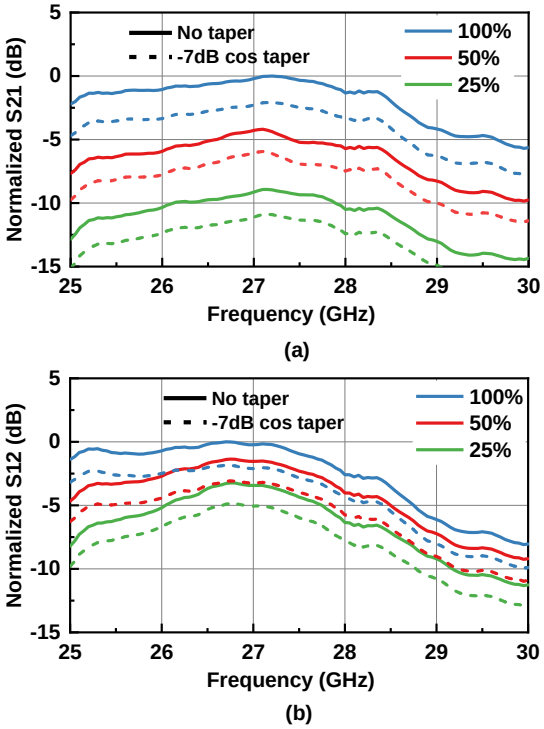

Figure 3.17: Measured normalized frequency response: (a) TX (b) RX.

3.4.2 EIRP and Directivity

Fig. 3.17(a) presents the normalized TX frequency response with R_{fill} = 1, 0.5, and 0.25. The decrease in EIRP is 4.4 dB and 9.2 dB for R_{fill} = 0.5 and 0.25, respectively. An EIRP drop of 4.9-10.1 dB (R_{fill} = 0.5-0.25) is expected, and the measured EIRP is 0.5-0.9 dB better. This could be due to a better impedance match with the PA, or a much lower heat load across the array, resulting in a higher P_{out} per 2×2 SiGe beamformer chip.

Fig. 3.17(b) presents the RX electronic-gain frequency response for R_{fill} = 1, 0.5, and 0.25. The RX electronic gain is defined as:

$$RX_{electronic\_gain} = P_{rec}/P_{inc} \tag{3.9}$$

where P_{rec} is the power at the RF connector and P_{inc} is the total power available at the the phased-

array aperture ($S \times Area$). S is easily calculated using $S = P_t G_t / 4\pi R^2$ (P_t is the transmit power from the network analyzer, G_t is the horn gain, and R = 2.5m), and $Area$ is the physical area of the 16x16 phased-array antenna (85mm$\times$81mm). This gain definition includes the antenna ohmic and dielectric loss (which is constant versus R_{fill}), the beamformer chip electronic gain (also constant versus R_{fill}), the Wilkinson network ohmic loss, and any reduction in the aperture efficiency due to R_{fill} (lower directivity). Since the elements of the 16$\times$16 array are turned off instead of not being present to emulate thinned arrays, and a 256:1 Wilkinson network is used with 50% or 75% of the elements not active, there is an excessive loss of 3 dB and 6 dB in the Wilkinson network for R_{fill} = 0.5 and 0.25, respectively. This loss is removed from measurements, so as to only show the drop in directivity.

The RX electronic gain decreases by 1.5-3.2 dB for R_{fill} = 0.5 to 0.25 while the expected decrease is 1.9 dB and 4.1 dB, respectively. Again, we believe that the discrepancy is perhaps due to a lower heat load (better chip electronic gain) and a better antenna impedance match. When a -7 dB raised-cosine taper is applied, the array gain decreases by 1.8-2 dB for all cases. The simulated drop in directivity for -7 dB raised-cosine taper is 0.5 dB, while the simulated power loss after combined in the Wilkinson network is 1.8-2 dB due to the taper (average electronic gain is lower across the array).

In conclusion, the measurements for EIRP and RX gain are better than simulation by 0.5-0.9 dB in both TX and RX, and show that randomized thinned arrays do produce the expected results.

3.4.3 EVM

For the case where communication systems allow relatively high sidelobes, such as in-house CPE (customer premise equipment) for 5G systems which operate in multi-bounce environments, it is important to determine the randomized thinned array performance under complex modulated waveforms. A Keysight M8195 arbitrary waveform generator (AWG) is

used to generate 16-QAM and 64-QAM waveforms at 27 GHz with a pulse shaping filter of α = 0.35, and the peak-to-average power ratio (PAPR) is 6.6 dB and 7.7 dB, respectively. The instrumentation EVM (at the amplifier's output) is presented in Fig. 3.18 and is $2 \pm 0.1\%$ for 100-200 MBaud waveforms. A standard gain horn antenna is used on the RX side, and the signal is demodulated using the Keysight DSOZ632A 63-GHz oscilloscope running the 89600 Vector Signal Analysis (VSA) software.

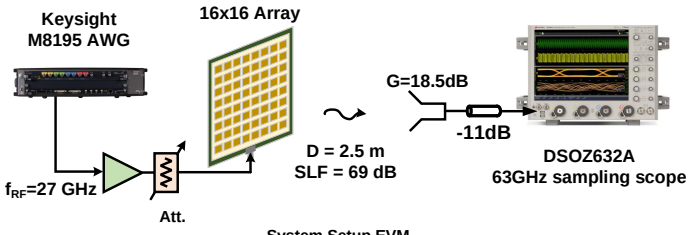

System Setup EVM

Mod/BW	100 MBaud	200 MBaud
16-QAM	1.98 %	2.09%
64-QAM	1.9%	2.2%

Figure 3.18: EVM measurement system setup and instrumentation EVM values.

Fig. 3.19(a) presents the EVM versus EIRP for 16-QAM waveforms with 100 MBaud symbol rate, measured with uniform array excitation. At low EIRP, the system EVM is limited by the setup As EIRP increases, the system EVM is dominated by the linearity of the phased array. For R_{fill} = 1, the EVM reaches 8% (-22 dB) at an EIRP of 60 dBm, 3 dB back-off from P_{1dB}. At a constant 8% EVM, the difference in EIRP between R_{fill} = 1 and 0.5 is 4.8 dB, and is 10.4 dB, and agrees with the results presented in Fig. 3.17(a).

Fig. 3.19(b) presents the EVM for 64-QAM waveforms with 100 MBaud symbol rate. The EVM reaches 5% (-26 dB) at 58.5 dBm (4.5 dB BO from P_{1dB}), and the decrease in EIRP at 5% EVM is 4.5 dB and 10.1 dB for R_{fill} = 0.5 and 0.25, respectively. Again, the results are consistent across different modulations. Fig. 3.19(c) presents the EVM of 64-QAM 100 MBaud waveform with a -7 dB raised-cosine taper applied. The EVM reaches 5% at 58 dBm for R_{fill} = 1, only 0.5 dB lower than uniform array excitation. A 5% EVM, the drop in EIRP is 5 dB and 4.9

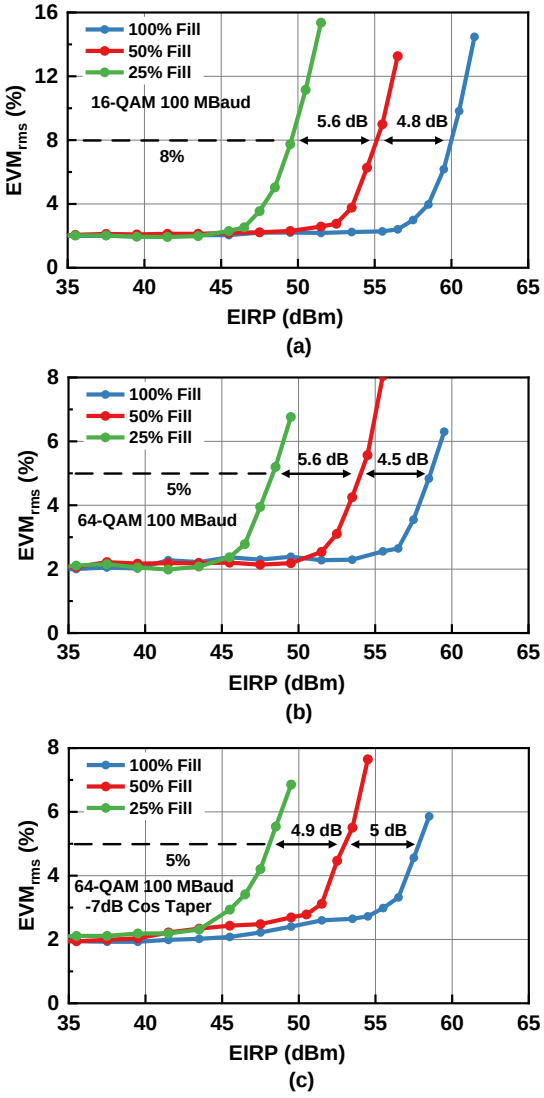

Figure 3.19: Measured EVM versus EIRP of (a) 16-QAM 100 MBaud waveform, (b) 64-QAM 100 MBaud waveform and (c) 64-QAM 100 MBaud waveform with -7 dB raised-cosine array taper.

dB for R_{fill} = 0.5 and 0.25, respectively, which agrees with uniform array excitation. The array taper does not affect EVM performance, and the EVM with -7 dB raised-cosine taper follows the same trend versus R_{fill} and EIRP. It is clear that the EVM curves are similar in all cases except for a absolute power shift. Therefore, if a 5G array with Rfill=0.5 and the same EIRP is required, then the power amplifiers on each channel should provide 5 dB higher power, but with half the number of elements.

3.5 Conclusion

This paper presented the analysis and measurements of TX and RX randomly thinned phased arrays for 5G and radar applications to reduce element density and save costs. The primary penalties for thinned randomized arrays are higher sidelobes over the entire 2-D space and decrease in directivity. However, it is shown in this paper that the reduced directivity does not drop as much as the decrease in elements and EIRP can be compensated by implementing power amplifiers with higher output power. The TX×RX sidelobe levels can be reduced by choosing an optimized complementary design and can be further improved by applying array taper. This results in a system that uses a significantly lower number of beamformer channels while maintaining a similar performance as a fully populated array. EVM measurements on 50% and 25% filled arrays also showed consistent results for 16-QAM and 64-QAM waveforms.

3.6 Acknowledgment

The authors thank Mirise/Toyota for techical discussions, Kyocera International, San Diego, for assembling the arrays in their state of the art assembly line, and the Keysight team, Santa Rosa, for technical discussions and state-of-the-art equipment. This work was supported in-part by Toyota/MIRISE and in part by the Defense Advanced Research Projects Agency (DARPA) under the JUMP DSSP program.

Chapter 3, in part, is a reprint of the material as it appears in: Y. Yin, Z. Zhang, T. Kanar, S. Zihir and G. M. Rebeiz, "A 24-29.5 GHz 256-Element 5G Phased-Array with 65.5 dBm Peak EIRP and 256-QAM Modulation," *2020 IEEE/MTT-S International Microwave Symposium (IMS),* Los Angeles, CA, USA, 2020, pp. 687-690, doi: 10.1109/IMS30576.2020.9224031. The dissertation author was the co-author of this paper.

Chapter 3, in full, is a reprint of the material as it may appear in: Z. Zhang, J.S. Schalch, Y. Yin and G. M. Rebeiz, "System-Level Analysis and Measurements of Thinned Randomized 27-29

GHz TX and RX Arrays for 5G Communications and for Radars with Low Sidelobe Levels," in *IEEE Transactions on Microwave Theory and Techniques,* submitted. The dissertation author was the primary investigator and author of this paper.

Chapter 4

Improved 5G and SATCOM Phased-Array Calibration Using the 2×2 Quad-Antenna Method

4.1 Introduction

Millimeter-wave 5G phased-arrays, typically 64 to 512 elements for small cells and large base-stations, are an essential component in all FR2 5G systems (26 GHz, 28 GHz, 37 GHz, 42 GHz, 48 GHz) as they provide a high antenna gain, a high equivalent isotropic radiated power (EIRP) and a large collecting aperture for the signals transmitted from user-equipment (cell phones or other devices) [14, 15]. They are built using multi-channel transmit/receive silicon beamformer chips with amplitude and phase control on every element [16–18, 20, 24, 25], placed next to the antennas on a low-cost printed-circuit board (Fig.4.1). Single and dual-polarized antennas and chips are generally used, but dual-polarized/dual-beam antennas have become more prevalent due to their 2×2 polarization-MIMO capabilities. The chips are designed to feed 4 antennas (2×2 quads), 8 antennas (2×4) and 16 antennas (4×4), and the 2×2 quad chips are the

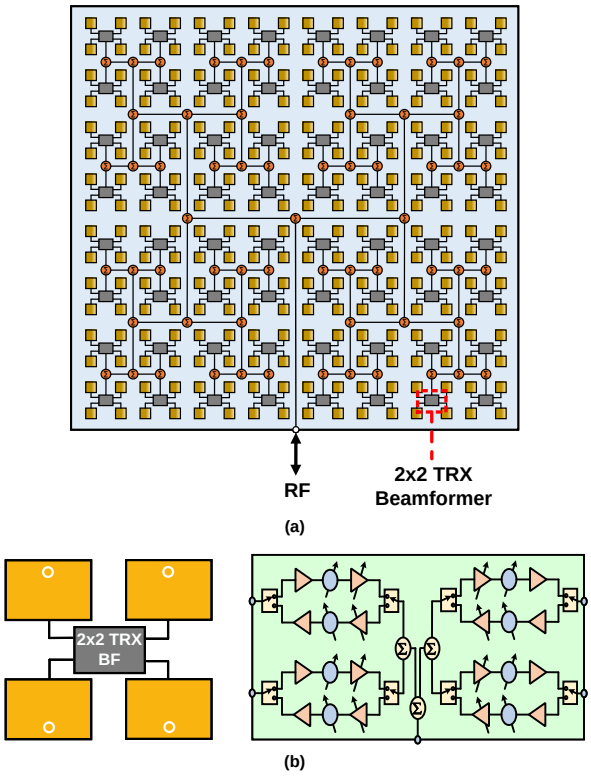

Figure 4.1: Block diagram of (a) phased array with 4-channel beamformers and (b) the 2×2 beamforming architecture.

most prevalent nowadays.

The same architecture applies to satellite communication phased-arrays at Ku and Ka-band, but in this case, the prevalent architecture is the 2×2 quads and the array size is 1024-4096. Also, SATCOM ground-terminal arrays are Tx-only and Rx-only for frequency-division duplexing (FDD) geostationary earth orbit (GEO) and medium earth orbit (MEO) satellite systems, and Tx/Rx for low earth orbit (LEO) satellite systems [57–60].

A key issue in all large phased-arrays is the calibration time and accuracy. The traditional method of turning on one element in a sequential manner and measuring the S_{21} in the near or far field is time consuming and is prone to errors (as will be shown in this work). Other techniques such as orthogonal code-domain calibration have been demonstrated, both using amplitude-only or 0°/180° Hadamard codes, and with good accuracy [61–63]. This work presents

a novel calibration technique based on the 2×2 quad-antenna method, and is applicable both in the near and far field, but the demonstrations here are done in the far-field. It will be shown that this technique results in higher accuracy and repeatability than the traditional method.

4.2 Traditional Calibration Method

The traditional method consists of turning on one antenna element at a time and measuring the S_{21} between the array common port and a far-field horn in an anechoic chamber. An up/down-converter can be used at the array or sub-array sum point, and the calibration is then done from IF/baseband (array port) to an RF or IF/baseband port at the standard-gain horn. A channel is defined as the gain and phase of every antenna element from the common port (RF or IF/baseband) to air, and takes into account the up/down-converters, Wilkinson network unequal phase and amplitude distribution errors, the gain and phase variations in the silicon RFIC channels, and any amplitude and phase difference in the transmission lines between the silicon RFIC and the antennas. Calibration is done by measuring every channel individually for all elements in the array, and then using the VGA and phase shifter in each channel (and if available, any subarray driver or up/down-converter) to compensate for the S_{21} differences between the channels [22, 28, 29]. The end goal is to equalize all the channels and to result in a uniform amplitude and phase across the phased-array aperture (low RMS amplitude and phase errors on the aperture).

Fig.4.1 presents a typical 5G phased-array built using 2×2 chips (single polarization is shown). Note that 5G and SATCOM systems do not employ a circulator or a matched absorptive switch on each element. This is done to achieve lowest loss performance at millimeter-wave and to reduce the system cost. Therefore, the off-antennas are terminated with reactive loads and not 50Ω. This reactive load can be a random low or high impedance (mostly reactive) and depends on the PA or LNA off-impedance and the transmission-line lengths between the silicon chip and the antenna feed.

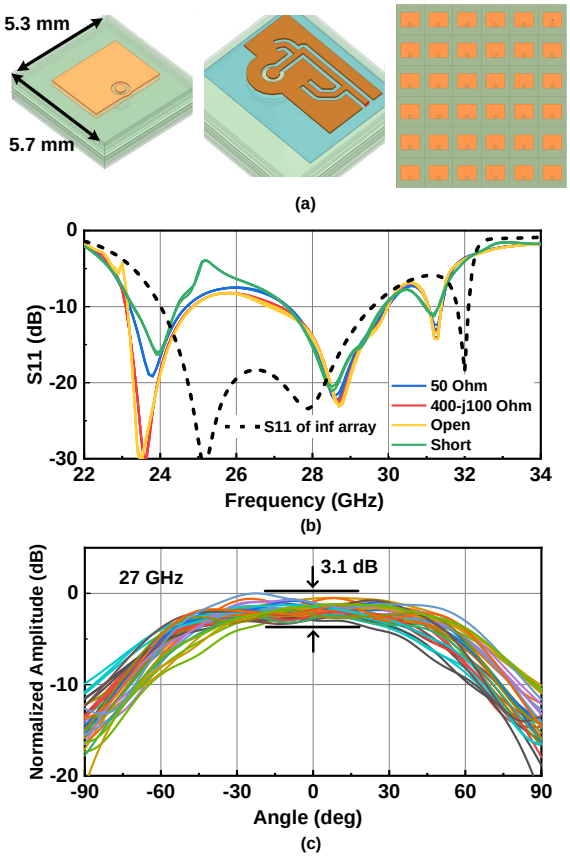

Figure 4.2: (a) Antenna and array configuration for simulation with single channel excitation; (b) simulated S_{11} of 4 center elements with different termination of surrounding elements compared to simulated S_{11} of an infinite array; (c) normalized patterns of all elements.

There are two effects arising from this technique: 1) The antenna impedance of the single microstrip antenna is different than the actual antenna impedance in a 2-D active array environment where all the elements are energized (designed and optimized using Floquet mode analysis), and 2) the patterns of the single antenna with neighbors having a reactive load has a lot of ripples. The ripples and non-uniformity of the element patterns are also observed and discussed in [64–66]. One cause of element patterns variation is the diffraction of surface waves and ground currents from the finite substrate and ground plane, which can result in undesirable effects on the element patterns.

To show these effects, a 6×6 microstrip antenna array with a period of $0.48\lambda_0 \times 0.52\lambda_0$

at 27 GHz in the azimuth and elevation planes, respectively, and placed on a Panasonic Megtron6 substrate with ε_r = 3.35, is simulated in Ansys HFSS using the radiation boundary conditions (Fig.4.2(a)). The simulated antenna impedance of the center 4 elements are shown in Fig.4.2(b), and S_{11} varies from -20 dB to -8 dB for different terminations for the neighboring antennas. However, this may not affect the calibration coefficients if all the antennas in a large array behave the same (impedance mismatch between the PA or LNA and the antenna is the same for all antennas).

A more important problem is the ripple in the element patterns (activated one at a time) arising from mutual coupling and spurious radiation from the neighboring elements (Fig.4.2(c)). Depending on the element location, there is a 3 dB peak-to-peak variation between the elements. Also, the element patterns cross each other at random angles. This means that the calibration coefficients obtained at 0° (broadside) will be different than the coefficients obtained if the calibration is done at 10° or 20°. This poses a significant problem for array calibration.

Another issue in single-element calibration is the signal-to-leakage ratio. 5G and SATCOM phased-arrays do not use isolated metal cavities and are based on silicon chips placed on printed-circuit boards. Therefore, there is signal leakage in every channel when turned off, and this can be significant in large arrays (Fig. 4.3). Consider a 256-element phased-array in the receive mode with channel gain of 25 dB (G_{ch}) in a 2×2 quad chip, and 45 dB of isolation (G_{leak} = -45 dB) when the channel is turned off. For an incident power density S (W/m^2) on the array aperture and a power collected per unit cell of $P_{avs} = S \times D_x \times D_y$ (W), where D_x and D_y is the length of the element aperture in the x and y direction, respectively. The signal at the RF connector is:

$$\begin{aligned} P_{rx} &= P_{avs} + G_{ch} - 3 \times N - L_{ohmic} \\ &= P_{avs} + 25 - 24 - 8 = P_{avs} - 7 \text{ dB} \end{aligned} \tag{4.1}$$

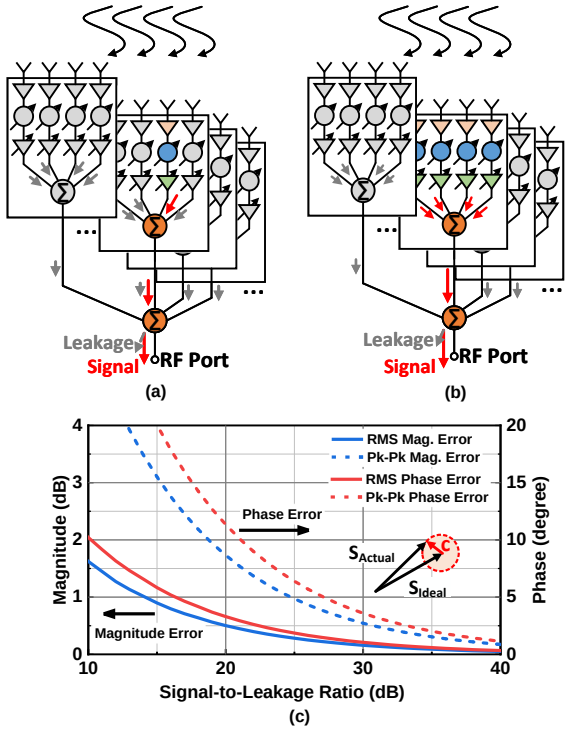

Figure 4.3: Demonstration of signal and leakage paths when (a) one channel is turned on and (b) a 2×2 quad is turned on, and (c) additional magnitude and phase errors versus signal-to-leakage ratio.

where N is the number of Wilkinson stages ($N = 8$ for a 256:1 network) and L_{ohmic} is the Wilkinson network ohmic loss (L_{ohmic} = 8 dB). Note that the received power by a single element power passes by a large Wilkinson network and suffers from 24 dB of excess network loss since only a single channel is activated.

On the other hand, the leakage power from the 255 (M=255) off-elements is:

$$\begin{aligned} P_{leak} &= P_{avs} + 10logM + G_{leak} - L_{ohmic} - L_{coh} \\ &= (P_{avs} + 24) - 45 - 8 - 2 = P_{avs} - 31 \text{ dB} \end{aligned} \tag{4.2}$$

where L_{coh} (1-2 dB) is the coherent additive loss of every 2×2 array since the channels are not calibrated. Note that there is no excess Wilkinson network loss since all the channel paths

are activated by the leakage signals. This results in a signal-over-leakage-ratio (SLR) of 24-25 dB for an off-channel isolation of 45 dB.

The leakage signal phase is not known and adds coherently to the single-element signal, thereby creating an error of up to (1±c) in magnitude and $\pm\tan^{-1} c \approx \pm c$ (rad) in phase on each single channel measurement. This is turn results in an RMS error when averaged over the 256 channels (Fig.4.3(c)). This leakage error is un-calibratable and will add to the final calibrated array RMS amplitude and phase values. An SLR of 25 dB results in an additional RMS errors of 0.3 dB and 2°.

Note that for near-field measurements, the leakage signal is much lower as the near-field probe radiates (or receives) from a small sub-array at a time when scanned across the aperture.

4.3 Quad 2×2 Calibration Method

The problems outlined above can be solved if a 2×2 quad is turned on as a single unit. It is assumed that the 2×2 quad is either symmetrical with equidistant lines between the silicon RFIC ports and antennas, or the 2×2 quad is pre-built as a connectorized unit test cell and characterized independently to find out the amplitude and phase difference between the 4 channels and the antenna feed points. Also, silicon beamformer chips nowadays all have power detectors or other built-in-self-test modes at their output ports, which can calibrate the channels to within ±1 dB in amplitude [67–70].

The 6×6 microstrip-antenna array is now simulated with different 2×2 unit cells activated and the other 32 antennas in an off-state with various termination impedance (Fig.4.4(a)). It is seen that the simulated antenna impedance for each antenna in the 2×2 quads is much closer to the 2-D Floquet mode impedance, resulting in a more accurate calibration (Fig.4.4(b)). Most important, the simulated patterns of the 2×2 quads show very little difference with only +/-0.12 dB variation between the different activated quads. The variation in the patterns reduced from a

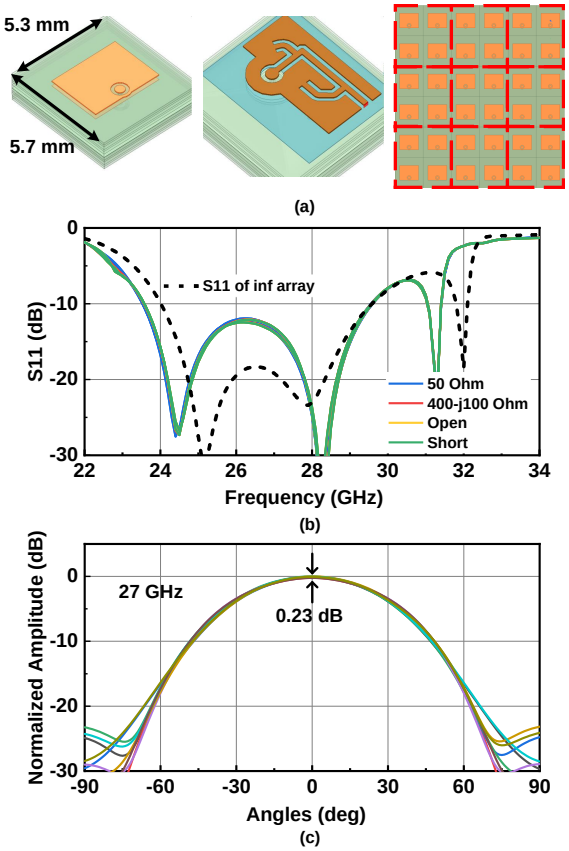

Figure 4.4: (a) Antenna and array configuration for simulation with 2×2 excitation; (b) simulated active S_{11} of 4 center elements all excited with different termination of surrounding elements compared to simulated S_{11} of an infinite array; (c) normalized patterns of all 2×2 quads.

peak-to-peak of 3.1 dB to 0.23 dB with the use of 2×2 quads (Fig.4.4(c)).

Furthermore, the 2×2 quads result in an SLR improvement of 12 dB (Fig. 4.3(b)). This is due to +6 dB additional signal level due to the actuation of four antennas instead of one antenna, and 6 dB less Wilkinson excess loss in the combining network. The leakage signal is basically the same (M=251 instead of 251). A 12 dB SLR improvement is critical as it improves the SLR from 25 dB to 37 dB, and results in virtually no added RMS amplitude and phase errors in the array calibration.

To compare the single-element and the quad calibration methods, the magnitude of the patterns of all elements at three different look angles (0°,-10°, and 10°) is shown in Fig. 4.5

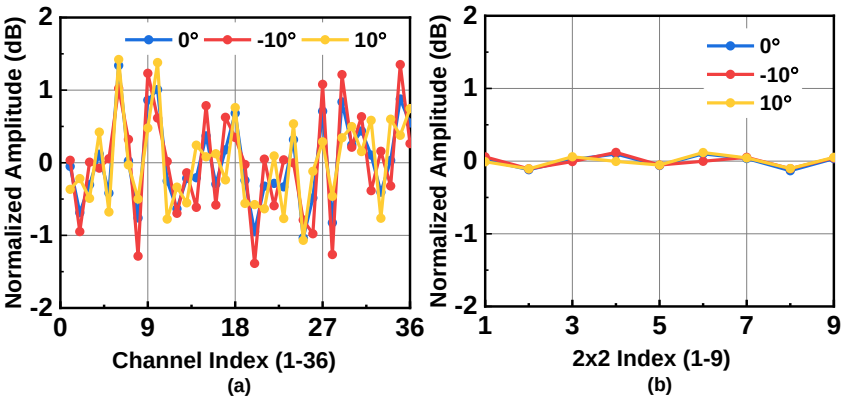

Figure 4.5: Normalized simulated amplitude variation for the 6×6 array at look angles of 0°, -10°, and 10° of (a) single elements and (b) 2×2 quads.

for both methods. Both plots are normalized to their average values. It is clear that the single elements patterns result in much larger variation across different elements and different look angles. This results in different calibration coefficients at different angles. The 2×2 element patterns are basically ideal versus look angle.

In short, by turning on 2×2 antennas at a time (one chip at a time), the 2×2 quad method results in better antenna impedance, removes the antenna ripples, and has higher SLR and better accuracy, It also calibrates out the average gain and phase variations between the silicon chips, the Wilkinson distribution network and the subarray drivers or up/down-conveters. An independent calibration needs to be done for the 2×2 cell if it is not symmetrical, but only for one cell and not for all cells in the array.

4.4 Pattern Investigations

The effect of the intrinsic error within a beamformer chip that forms a 2×2 antenna quad are now investigated. Assuming that the quad (2×2) calibration has removed all the errors up to the chips and calibrated out the average gain and phase difference between the chips, the remaining errors will be the differences between the individual channels within a beamformer

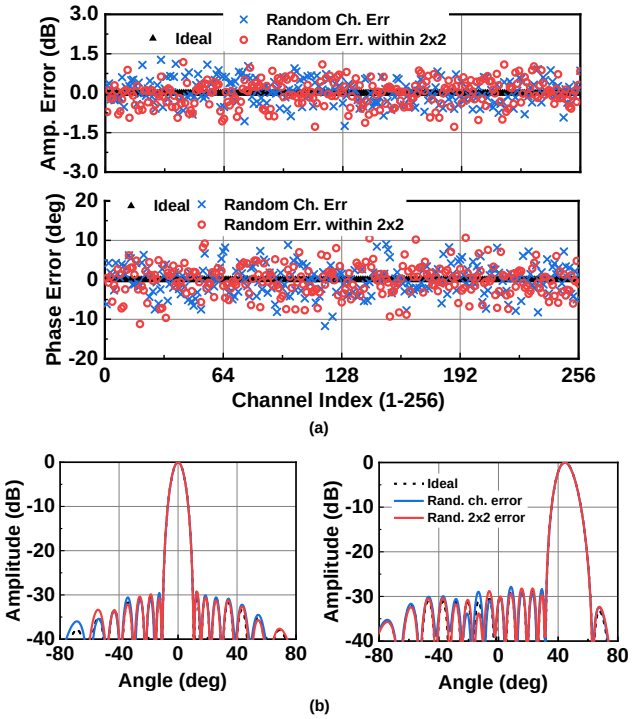

Figure 4.6: (a) Distribution of RMS amplitude and phase errors of 0.5 dB and 4° generated repeatedly for every 2×2 quads in a random fashion, and generated at once for all 256 channels, compared to the ideal case. (b) Corresponding patterns at broadside and 45° scan with -30 dB Taylor taper.

chip and their transmission-line connections to the antennas (these connections can be considered as part of the individual channels). In order to investigate this effect, different amplitude and phase errors with RMS values of 0.5 dB (±1 dB peak) and 4° (±8° peak), respectively, are imposed on the 64 2×2 quads in the array, representing the chip local error in a perfectly calibrated array at the 2×2 level. Also, an amplitude and phase distribution with the same RMS error is generated at once for the 256 channels, representing a non-ideal calibration using the single element method. The patterns of these two distributions are plotted in Fig. 4.6 at broadside and 45° scan with -30 dB Taylor taper distribution. The pattern shows very little difference between these two types of errors, and a close match to the ideal pattern up to -30 dB Taylor taper. The results clearly indicate that the internal errors inside the beamformer chips have the same effect as an array with random errors provided that the errors in the 2×2 cells are random and not systematic (same error

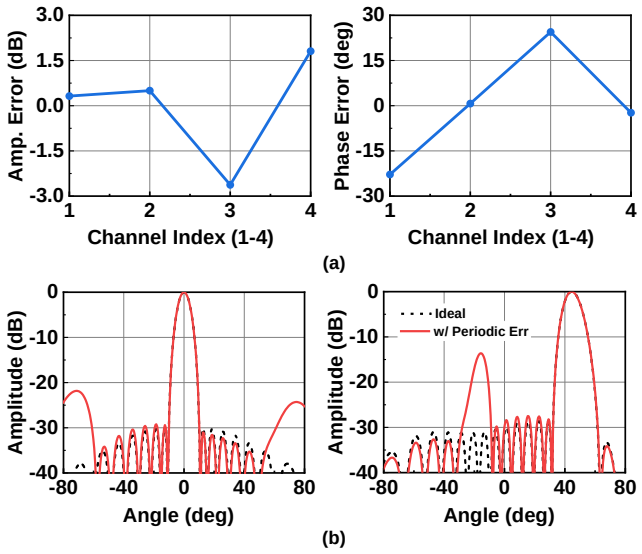

Figure 4.7: (a) Distribution of RMS amplitude and phase error of 2 dB and 20° for 4 channels within a 2×2 quad and repeated periodically for all 2×2 quads. (b) Corresponding patterns at broadside and 45° scan with -30 dB Taylor taper.

appears on the same channel over and over again).

The effect of systematic errors in the 2×2 quad are much more severe as shown in Fig. 4.7. In this case, a randomly generated error of ±15° in phase and 1.6 to -2.8 dB in amplitude is taken in a unit cell and is repeated for all quads in the array. Again, a -30 dB Taylor distribution is assumed to result in low sidelobe levels. One can clearly see the illumination error grating lobes for the broadside pattern since they occur at a period of $1\lambda_0$. Also, the error lobes scan with the patterns and appear at -10° for a 45° scan angle. Note that if a uniform illumination is used with -13 dB sidelobe levels, such error sidelobes will not be prominent, but they are clearly seen in -20 dB or -30 dB Taylor tapers. Therefore, it is important to remove the systematic errors in the 2×2 quad (generally arising from the transmission line connections) using a separate calibration, and this is usually done in a connectorized test cell. Alternatively, one can use the Ansys HFSS models for these transmission-line connections to calibrate them out. As seen above, as long as the residual amplitude and phase errors in a unit cell are within ±1 dB and ±8°-10° in a random fashion (chip-to-chip variations), then one can achieve -30 dB sidelobes with no issues.

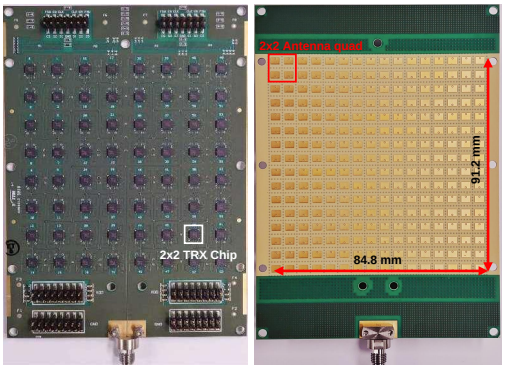

Figure 4.8: A 256-element Ka-band phased-array using 64 2×2 beamformer chips and stacked-patch antennas.

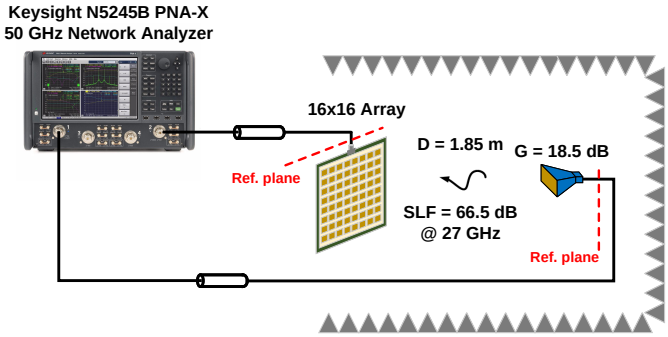

Figure 4.9: Far-field measurement setup for calibration of the 256-element phased array.

4.5 Measurements

The measurements are done on a 256-element single-polarized Ka-band phased array that can be used in 5G and radar systems. The array is based on commercial 2×2 Tx/Rx beamformer chips, designed with SiGe BiCMOS technology. Each chip consists of 4 RF channels and one common RF port, and with operation at 25–30 GHz. Each channel has a 6-bit phase shifter, 8-bit gain control, a PA, and an LNA and a Tx/Rx switch.

Fig. 4.8 presents the antenna and chip-side views of the 256-element phased array. All elements are combined using a 64:1 symmetrical Wilkinson network, with a symmetrical and equidistant layout between the common port and each of the beamformer chips. The antenna utilizes a stacked-patch structure for wide band operation with a simulated -10 dB S_{11} bandwidth

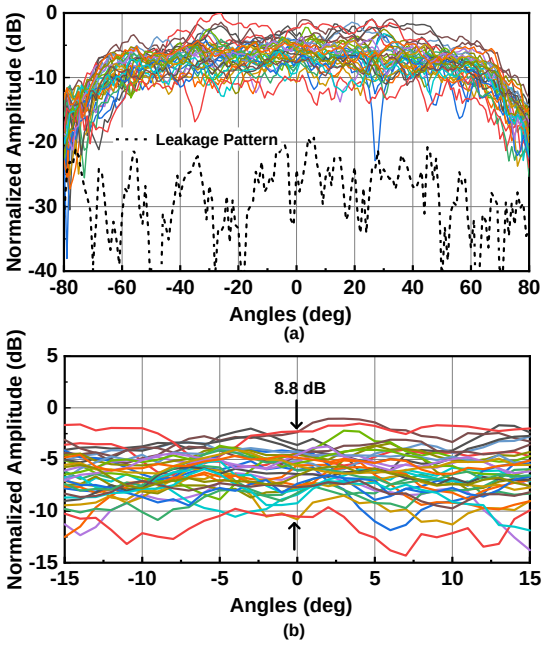

Figure 4.10: (a) Normalized element patterns of selected antennas and leakage pattern of the array at 27 GHz. (b) Element patterns from -15° to 15°.

of 24-30 GHz. Also, the connections between the 4-channel chip and the 2×2 antennas are perfectly symmetrical with equidistant lines and therefore, in this work, no independent calibration is done for the 2×2 cell. This design has been presented before and will not be further discussed here for brevity [26].

The 256-element phased-array was measured in an anechoic chamber, with a distance of 1.85 m and space loss of 66.5 dB at 27 GHz. The far-field range is 2.8 m, and a measurement distance of 1.85 m results in a spherical-wave aperture phase error of 32.4° between the center of the array and the diagonal array edge (to the horn). Increasing the measurement distance to 3.7 m will reduce the aperture phase error by half. A Keysight N5245B PNA-X 50-GHz vector network analyzer (VNA) is used for S_{21} measurements and with the cable loss calibrated out (Fig. 4.9).

Fig. 4.10 presents the measured patterns of 40 different antenna elements in the 256-element phased-array with a single element activated at a time. The patterns exhibit large variations at broadside (8.8 dB) and even larger variations at other angles. Larger amplitude

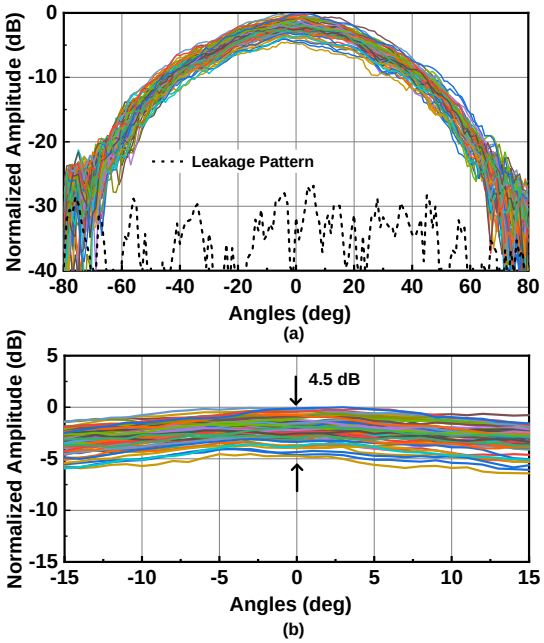

Figure 4.11: (a) Normalized 2×2 and leakage patterns of the array at 27 GHz. (b) 2×2 patterns from -15° to 15°.

variation requires more gain states to be used for calibration, leaving less dynamic range for tapering that is needed for low sidelobe levels. In addition, each element pattern displays ripples over all angles, with multiple cross-over, and a calibration at 0° (broadside) results in different amplitude and phase corrections than if the calibration is done at 5° or 10° off broadside.

The leakage pattern measured when all the elements are shut off and normalized to a peak element pattern is also plotted in Fig. 4.10(a). An average SLR of 17 dB is found at broadside, and results in an additional RMS amplitude and phase error of 0.7 dB and 4.6°, and peak-to-peak amplitude and phase error of 2.4 dB and 16°, respectively. The signal-to-leakage ratio is on the low side due to an lower isolation of -40 dB of the first-generation chips and the leakage from the RF connector, resulting in 7 dB more leakage than calculated before.

Fig. 4.11 presents the measured patterns of all 64 2×2 quads. The patterns at broadside exhibit much smaller variation compared to the element patterns (4.5 dB versus 8.8 dB), which can be corrected using fewer VGA states. The patterns also exhibit less ripples across all angles,

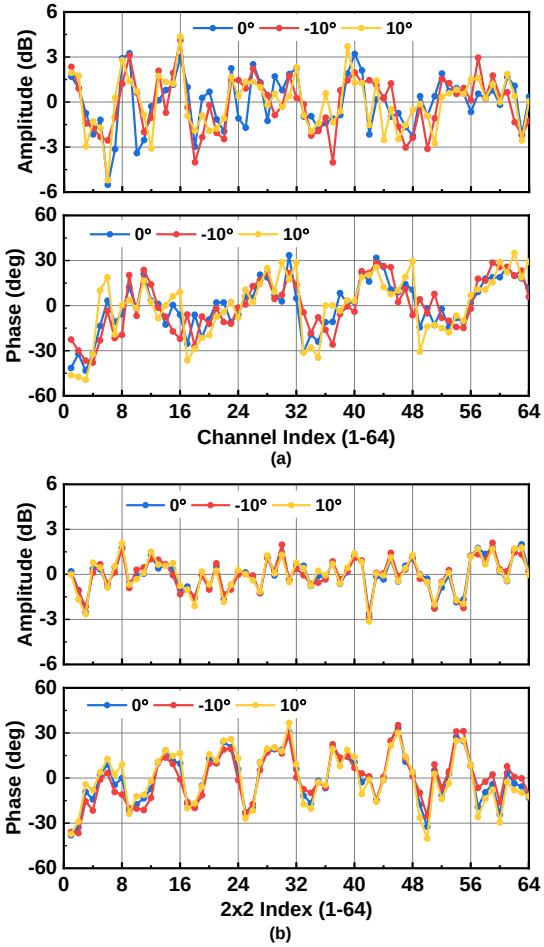

Figure 4.12: Normalized measured amplitude and phase variations at look angles of 0°, -10°, and 10° of 64 (a) elements and (b) 2×2 quads.

creating fewer cross-overs between patterns, and the calibration values obtained at broadside are close to the values obtained at 10°–20° off-broaside. In addition, the average signal-to-leakage ratio of the 2x2 patterns increases by 12 dB at broadside compared to the element patterns (from 17 dB to 29 dB), as predicted. This results in an additional RMS error of only 0.2 dB and 1.3° across the array.

Fig. 4.12 presents the measured single-element and 2×2 patterns values at three different look angle (0°,-10°, and 10°), normalized to their average values. Only 64 individual elements are plotted in Fig. 4.12(a) for clarity. The 2×2 patterns show lower amplitude and phase variations

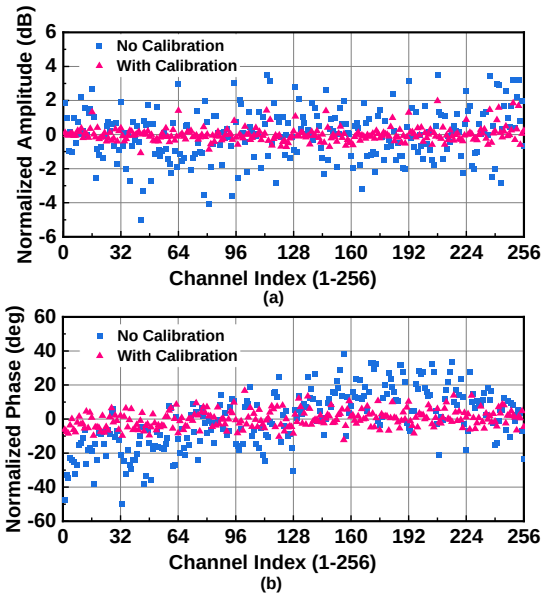

Figure 4.13: (a) Amplitude and (b) phase distribution measured at 27 GHz broadside in RX mode for 256 channels before and after channel calibration.

across all elements, and more importantly, the same calibration coefficients are obtained if the measurements are done at 0° or ±10°. This applies to both amplitude and phase.

Fig. 4.13 presents the measured amplitude and phase distribution of all 256 channels at 27 GHz at broadside with and without calibration, using single-element calibration, normalized to the average amplitude and phase values. The array results in an RMS error of 1.5 dB and 17° before calibration, and 0.5 dB and 5° after calibration. The average decrease in amplitude is 3.5 dB after calibration, and the VGA range has been limited to 7 dB (0 dB to -7 dB).

Fig. 4.14 presents the amplitude and phase distribution of all 2×2 quads at 27 GHz at broadside with and without calibration. In this case, the array shows an RMS error of 1.1 dB and 17° before calibration, and 0.15 dB and 2.3° after calibration, resulting in an almost flat response over all 2×2 quads and very accurate array calibration. The average decrease in amplitude is 2.3 dB after calibration, and the VGA range used is 0 dB to -4.5 dB. The 2×2 calibration is done by changing the VGA and phase shifters of all 4 channels in the same chip simultaneously.

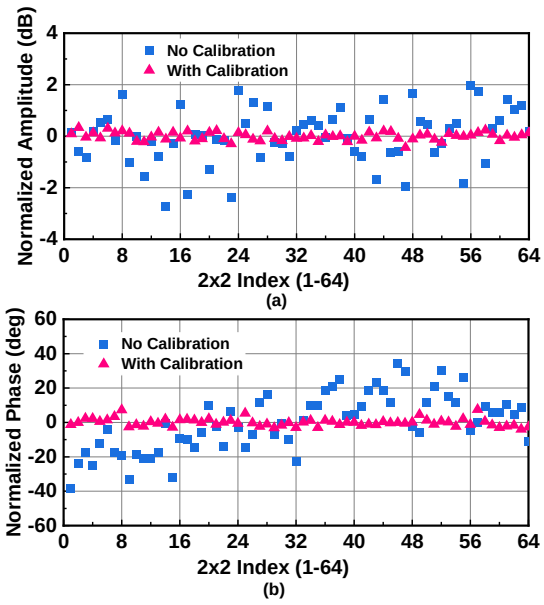

Figure 4.14: (a) Amplitude and (b) phase distribution measured at 27 GHz broadside in RX mode for 64 2×2 quads before and after 2×2 calibration.

4.6 Pattern Measurements

The measured patterns of the 256-element phased array at 27 GHz under uniform illumination scanned to 0°, 30°, 45° and 60° are plotted in Fig. 4.15(a)-(d). At broadside, the patterns with both calibration methods produce symmetrical sidelobes with almost identical levels, and the primary advantage of the 2×2 method is reduced calibration time. The reason is that a rectangular array with uniform illumination produces high sidelobes in the major axes (-13.6 dB) and is very tolerant to amplitude and phase errors. However, if a full 3-D patterns were taken, one would be able to see that the 2×2 calibration results in better sidelobes on the diagonal axes.

A better check for this method is to use aperture distributions with low sidelobe levels. Fig. 4.15 presents the measured patterns at broadside and 45° scan for a -25 dB Taylor distribution. It is clear that the 2×2 quad calibration results in better patterns than the single-element method with slightly lower sidelobe level and a more symmetrical pattern. However, with -35 dB Taylor distribution, the 2×2 quad method results in much lower sidelobe levels than single element

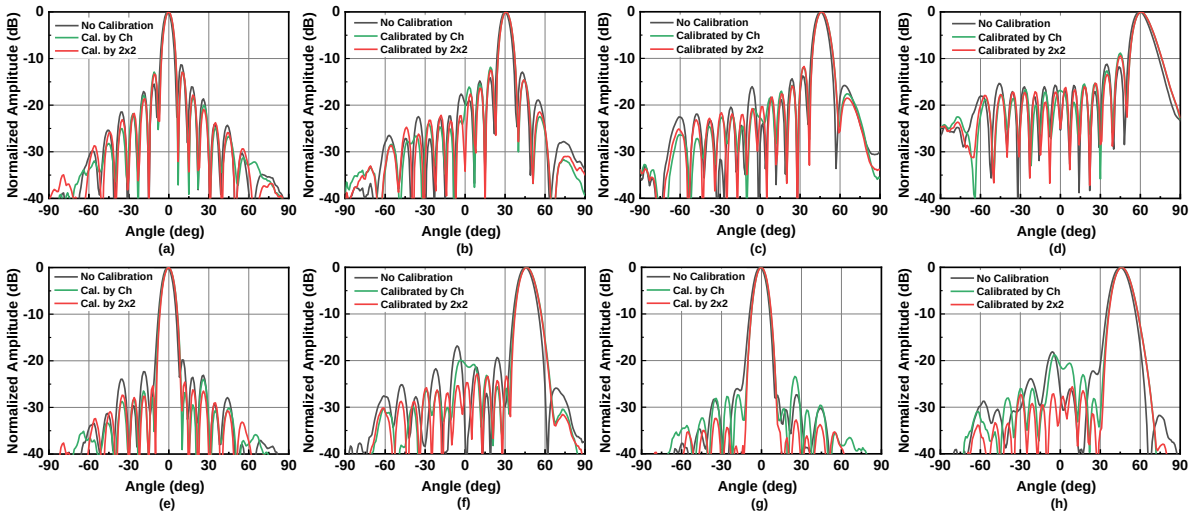

Figure 4.15: Measured patterns of the 256-element phased array without calibration, with calibration by channel and by 2x2 quads when scanned to (a) 0°, (b) 30°, (c) 45°, and (d) 60° without taper; patterns with -25 dB Taylor taper at (e) 0°, (f) 45° scan, and with -35 dB Taylor taper at (g) 0°, (h) 45° scan.

calibration, reaching even below -30 dB for the peak sidelobe level. Therefore, calibration based on 2×2 quads shows a significant advantage for applications that require low sidelobes.

Note that the calibration is done only at broadside for both methods, but the phase shifter itself has RMS errors of 0.7 dB and 3.6°. at 27 GHz, and this limits the sidelobe level when scanned to 45°. Better patterns could have been obtained if the phase shifter errors are calibrated out, but this is not done here. The phase shifter errors add to the residual calibration errors, and affect the quad 2×2 calibration more than the single-element calibration since it has lower residual RMS errors.

Fig. 4.16 presents the gain states of all 256 VGAs applied to the phased array using the two calibration methods, for a -35 dB Taylor taper illumination. The VGA settings must meet both the phased-array calibration (first) and then the taylor illumination (second). On average, calibration using 2×2 quads method employs 5 fewer gain states (0 is the maximum gain state) at the center of the array, resulting in larger dynamic that is needed for aggressive tapering.

Lastly, Fig. 4.17(a) presents the measured patterns with the array calibrated using the quad (2×2) method, for a -25 dB Taylor taper and scan angles up to ±60° in the azimuth plane. The

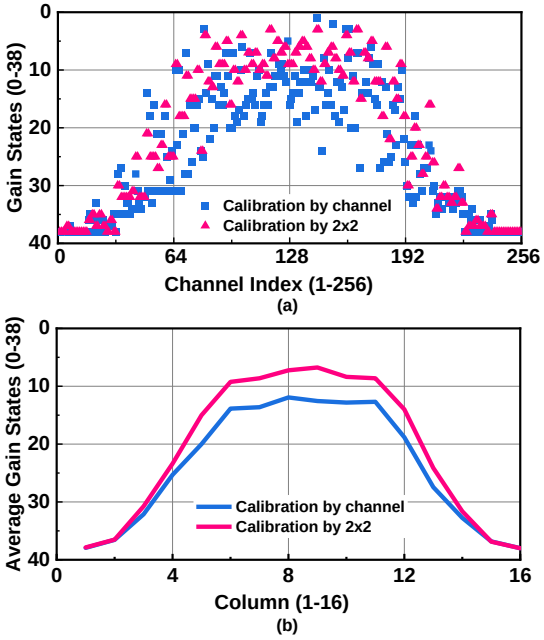

Figure 4.16: (a) Gain states of VGAs of all channels used for calibration with two different methods and a -35 dB Taylor taper. (b) Average gain states of columns on the azimuth plane used for calibration with two different methods and a -35 dB Taylor taper.

patterns exhibit low sidelobe levels at all scan angles. A comparison with simulations is shown in Fig. 4.17(b) for patterns at broadside. A sidelobe level of -25 dB and excellent agreement with simulations are achieved.

4.7 Mathematical Quad Calibration based on Single-Element Measurements

The responses of the 2×2 antenna quads can be approximated by adding 4 corresponding single channel responses mathematically in post-processing, and this can be used to calibrate the array using fewer VGA states. However, by doing the mathematical quad calibration, the advantages of shorter measurement time of the 2×2 calibration are lost.

Fig. 4.18 presents the 256-element array measured amplitude and phase variation of

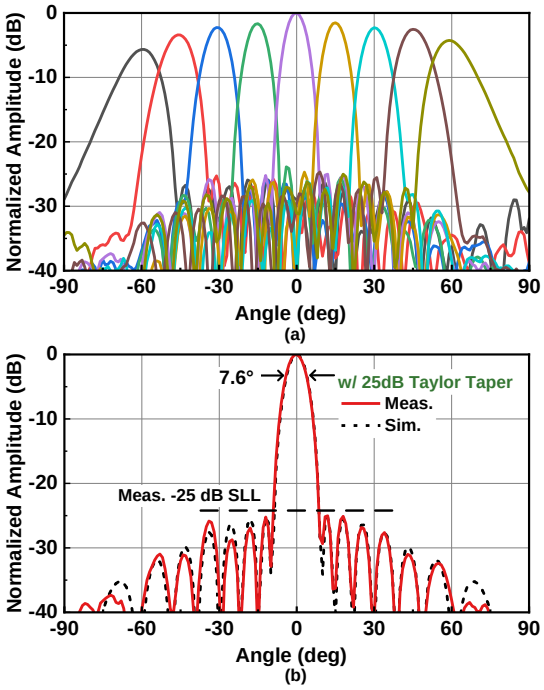

Figure 4.17: (a) Measured H-plane (azimuth) scanned patterns to $\pm 60^{\circ}$ at 27 GHz with 25-dB Taylor taper. (b) Measured versus simulated H-plane pattern at 27 GHz.

single elements and 2×2 antenna quads in the Rx mode at 27 GHz, as well as the mathematically averaged 2×2 responses calculated from the corresponding single element data. The calculated 2×2 responses tracks the measured 2×2 data closely, with an RMS amplitude and phase difference of 0.26 dB and 1.2°, respectively, between the two. This is very close knowing that one can have a bit of reflections from the PCB edges, connector leakage (not part of the array leakage) and the surrounding environment.

Fig. 4.19 presents the measured 2×2 patterns versus the mathematically calculated ones of several 2×2 quads at 27 GHz. The calculated patterns match the measured ones closely, but with ripples as a result of the reasons stated above. This means that, while better than single element calibration, the mathematical quad calibration technique exhibits larger error and is less robust across different scan angles than the true 2×2 calibration technique. Still, it is a worthy alternative to consider in case a true 2×2 quad cannot be done.

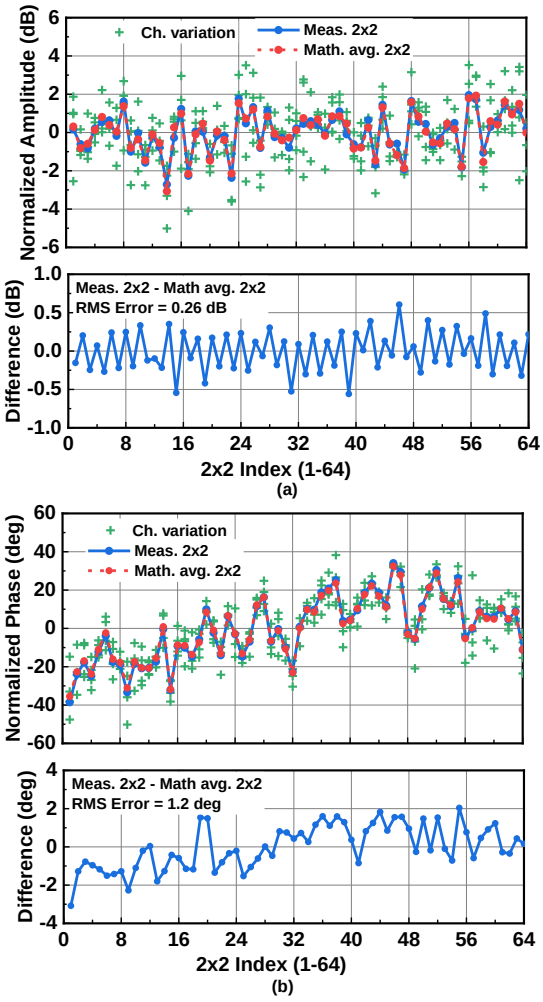

Figure 4.18: (a) Amplitude and (b) phase variation of measured single elements, 2×2 quads and 2×2 quads by mathematically averaging 4 elements at 27 GHz, and the difference between the measured and mathematically averaged 2×2 quads.

4.8 Conclusion

Two different methods for phased arrays calibration are presented in this paper. While the traditional single element calibration method results in good performance, the 2×2 method produces more accurate and robust calibration due to a closer match of the active impedance to that of an infinite array and fewer ripples in the 2×2 patterns. Further more, the 2×2 calibration yields patterns with lower sidelobe levels when aggressive tapers are applied, due to fewer

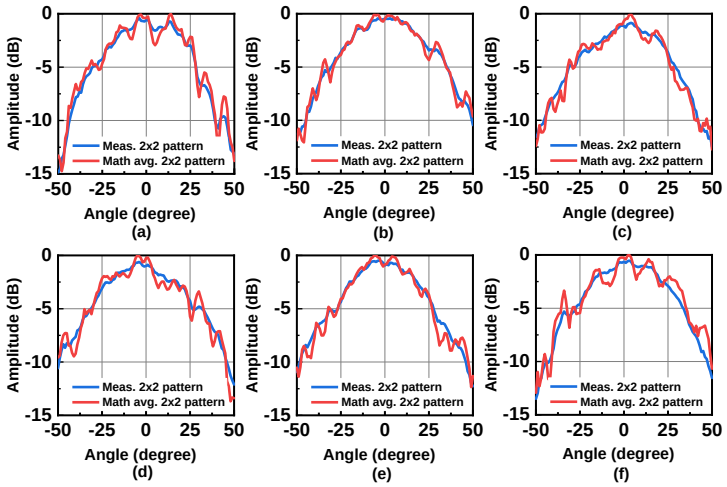

Figure 4.19: Measured and mathematically averaged 2×2 patterns of 6 selected 2×2 quads in the 256-element array at 27 GHz.

VGA gain states used for calibration and higher available dynamic range for taper control. This method is applicable to both single-polarization and dual-polarization dual-beam arrays for 5G applications.

4.9 Acknowledgment

The authors thank Kyocera International, San Diego, for assembling the arrays in their state of the art assembly line, and the Keysight team, Santa Rosa, for technical discussions and state-of-the-art equipment. This work was supported in part by Keysight, in part by the by the Semiconductor Research Corporation (SRC) and the Defense Advanced Research Projects Agency DARPA under the JUMP program with a DSSP addition.

Chapter 4, in part, is a reprint of the material as it appears in: Y. Yin, Z. Zhang, T. Kanar, S. Zihir and G. M. Rebeiz, "A 24-29.5 GHz 256-Element 5G Phased-Array with 65.5 dBm Peak EIRP and 256-QAM Modulation," *2020 IEEE/MTT-S International Microwave Symposium (IMS),* Los Angeles, CA, USA, 2020, pp. 687-690, doi: 10.1109/IMS30576.2020.9224031. The dissertation author was the co-author of this paper.

Chapter 4, in full, is a reprint of the material as it may appear in: Z. Zhang, A. Nafe, Y. Yin and G. M. Rebeiz, "Improved 5G and SATCOM Phased-Array Calibration Using the 2×2 Quad-Antenna Method," in *IEEE Transactions on Microwave Theory and Techniques,* submitted. The dissertation author was the primary investigator and author of this paper.

Chapter 5

Near-field Error Vector Magnitude Measurement and Analysis

5.1 Introduction

With millimeter-wave phased-array systems becoming more and more popular and with more units being deployed in the fields of 5G, satellite communications and radar applications, the calibration of phased arrays have become a larger than ever challenge that is necessary for a seamlessly working system. For phased arrays used in SATCOM systems, the size of the arrays usually exceed 4000 elements due to the stringent radiation mask regulations. Due to the far field distance of such large phased arrays, it becomes costly to set up a far-field measurement system to calibrate the array regularly. For smaller phased arrays of 64 to 384 elements such as the ones used in 5G communication and automotive radar systems, a far-field calibration becomes impractical due to the large amounts of units deployed in the field. Therefore, a near-field calibration system with simple setup that can be used on arrays deployed in the field is necessary and results in high cost-saving.

A built-in-self-test (BIST) calibration method utilizing the mutual coupling symmetry

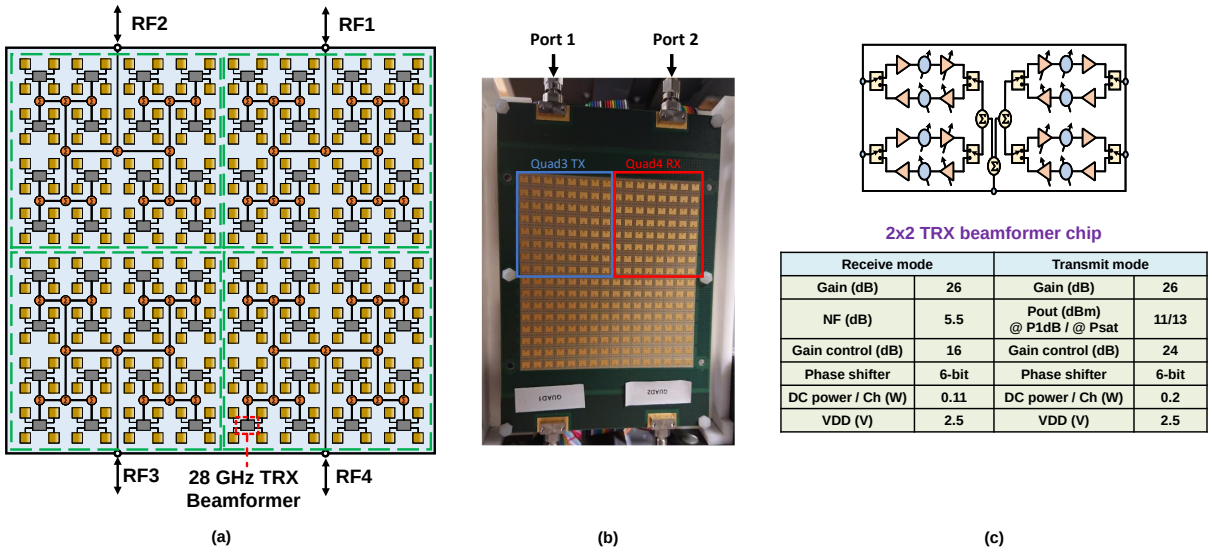

Receive mode		Transmit mode	
Gain (dB)	26	Gain (dB)	26
NF (dB)	5.5	Pout (dBm) @ P1dB / @ Psat	11/13
Gain control (dB)	16	Gain control (dB)	24
Phase shifter	6-bit	Phase shifter	6-bit
DC power / Ch (W)	0.11	DC power / Ch (W)	0.2
VDD (V)	2.5	VDD (V)	2.5

Figure 5.1: (a) Block diagram of the 4×8×8 TRX phased array with 4-channel beamformers, (b) its photo, and (c) block diagram and summary of the 4-channel 28 GHz TRX beamformer chip.

between antennas in a phased array has been demonstrated with great success and with similar performance compared to far-field calibration [13], and this chapter is an extension of the BIST calibration. One way to verify the results of phased array calibration is to measure a complex modulated signal used in communication systems. In this chapter, the error vector magnitude (EVM) of a complex modulated signal is measured and investigated using near-field coupling on a 28 GHz 4×8×8 phased array with 4 quadrants (fig. 5.1). Each quadrant has an independent RF port and can be set to TX or RX mode individually. Section II investigates the different coupling levels between different combinations of TX and RX antennas and explains the combinations used for EVM measurements. Section III presents the near-field EVM measurement results and compared them to the far-field ones, and section IV concludes this chapter.

5.2 Near-field Coupling

Fig. 5.1 (a) and (b) present the block diagram and photo of the 28 GHz 4×8×8 phased arrays with 4 quadrants and 4-channel TX/RX beamformer chips, and fig. 5.1 (c) presents the

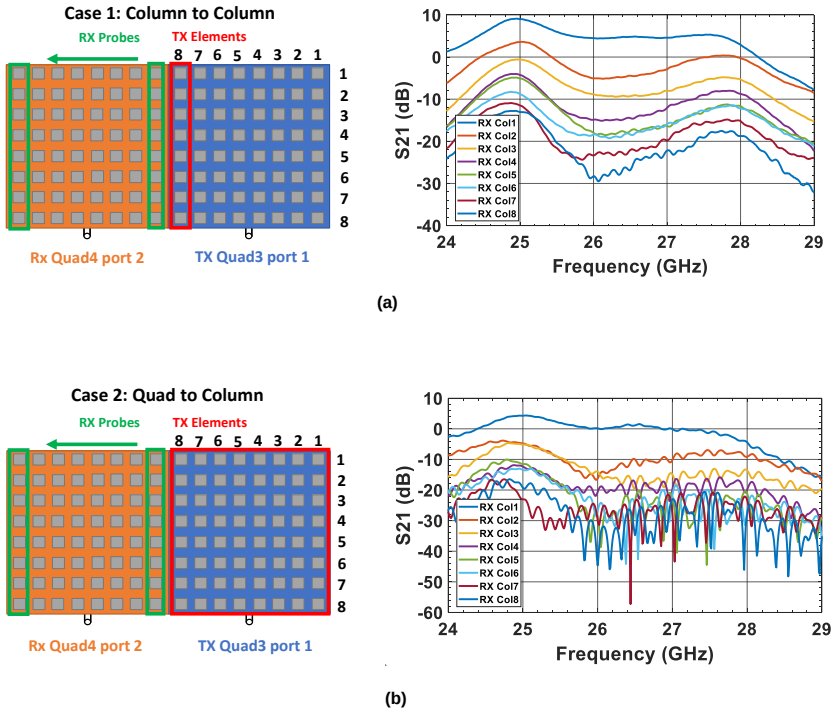

Figure 5.2: (a) Measured port-to-port S_{21} when (a) column 8 of quad 3 is turn on in TX mode and (b) entire quad 3 is turned on in TX mode, with column 1 to 8 of quad 4 are turned on one by one in RX mode.

beamformer architecture, with each channel consisting of a TX and RX path, and the summary of key parameters. Channels in quad 3 of the array are set to TX mode and are the "antennas under test" for the EVM measurements, and channels in quad 4 are set to RX mode and act as the near-field probes. The S_{21} is measured from port 1 to port 2 using a vector network analyzer.

Fig. 5.2 presents two cases of the coupling levels measured on the $4\times8\times8$ array. In case 1 (fig. 5.2(a)), Only column 8 of quad 3 is turn on in the TX mode, and the S_{21} is measured from column 1 to column 8 individually in the RX mode. Strong coupling can be observed when adjacent TX and RX columns are turned on and decreases gradually when the RX probes move away from the TX column. In case 2, instead of 1 TX column, the entire quad 3 is turned on in the TX mode and the coupling levels are measured from column 1 to column 8 in the RX mode in quad 4. However, even with more TX channels turned on in case 2, the coupling levels drop compared to case 1. This is due to the coupling levels from the different TX columns adding out

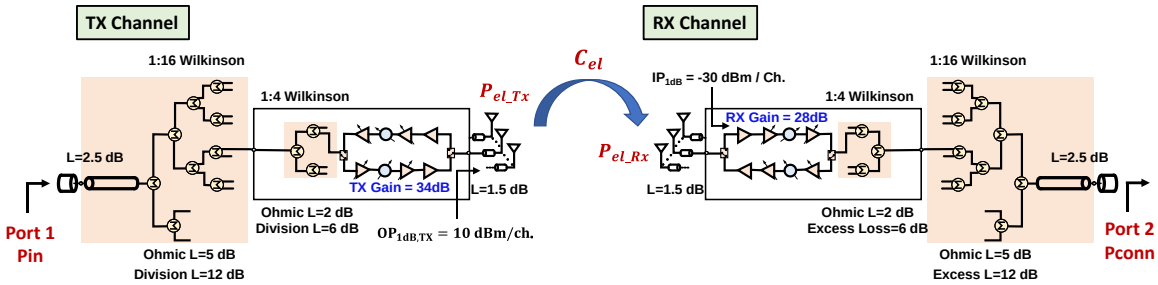

Figure 5.3: Block diagram of the TX and RX channels and the feeding networks of the 4×8×8 array and demonstration of the element-to-element coupling

of phase at the receive column due to the $\lambda/2$ spacing between antennas. When the RX columns are close to quad 3, the coupling from column 8 in quad 3 dominates, and the out-of-phase coupling from other elements only creates small ripples as seen in the measured S_{21}. However, when the RX columns become far from the TX quad, the couplings start to cancel each other, creating deep nulls in the S_{21} measurements. Therefore, due to the stable coupling levels, case 1 is chosen for the EVM measurements.

We are interested in the coupling levels from the TX channel outputs to the RX channel inputs, and therefore, the responses of the TX and RX channels need to be de-embedded in calculations.

Fig. 5.3 presents the block diagram of TX and RX channels with the Wilkinson networks and transmission lines in the 4×8×8 array and the demonstration of coupling when only one TX and one RX channels are activated. The TX electronic gain from the RF input port to the antenna feed port, with the loss in the feed network, can be calculated as

$$G_{el\_Tx} = \frac{P_{el\_Tx}}{P_{in}} = L_{Ohmic} + L_{div} + G_{Ch\_Tx} + L_{ant} = 5 \text{ dB} \tag{5.1}$$

where P_{el_Tx} is the radiated power from the antenna, P_{in} is the input power at the RF port, L_{Ohmic} is the ohmic loss in the feed network, L_{div} is the division loss of the Wilkinson network, G_{Ch_Tx} is the gain of a TX channel in the beamformer chip, and L_{ant} is the loss of the antenna.

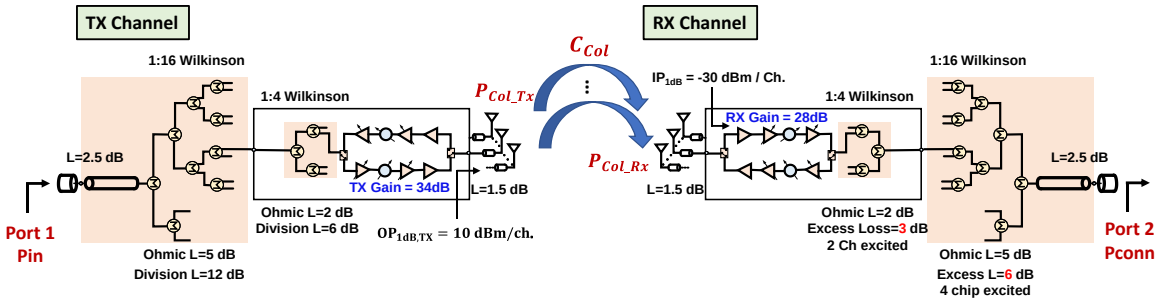

Figure 5.4: Block diagram of the TX and RX channels and the feeding networks of the 4×8×8 array and demonstration of the column-to-column coupling

The RX electronic gain from the antenna feed port to the RF port can also be calculated as:

$$G_{el\_Rx} = \frac{P_{conn}}{P_{el\_Rx}} = L_{ant} + G_{Ch\_Rx} + L_{Ohmic} + L_{excess} = -1 \text{ dB} \tag{5.2}$$

where L_{excess} is the excessive loss of the RX Wilkinson network that is present when only some of the channels are turned on. $L_{excess} = 0$ when all the RX channels of the array are turned on as condition the array normally operated in. Using (5.1) and (5.2), the coupling from antenna to antenna can be calculated as (Fig. 5.4):

$$C_{el} = S_{21} - G_{el\_Tx} - G_{el\_Rx} = S_{21} - 4 \text{ dB} \tag{5.3}$$

where S21 is measured from the RF port on the Tx quadrant (Port 1) to the RF port on the Rx quadrant (Port 2). Fig. 5.4 presents the block diagram of TX, RX channels and feed networks and demonstration of coupling when one column (8 channels) of TX and one column of RX channels are turned on. Compared to the element-to-element coupling shown in Fig. 5.3, the TX radiated power is $10log8 = 9$ dB higher and the excess loss in the RX Wilkinson network is 9 dB lower. Therefore, the column-to-column coupling level becomes:

$$C_{Col} = S_{21} - G_{Col\_Tx} - G_{Col\_Rx} = S_{21} - 22 \text{ dB} \tag{5.4}$$

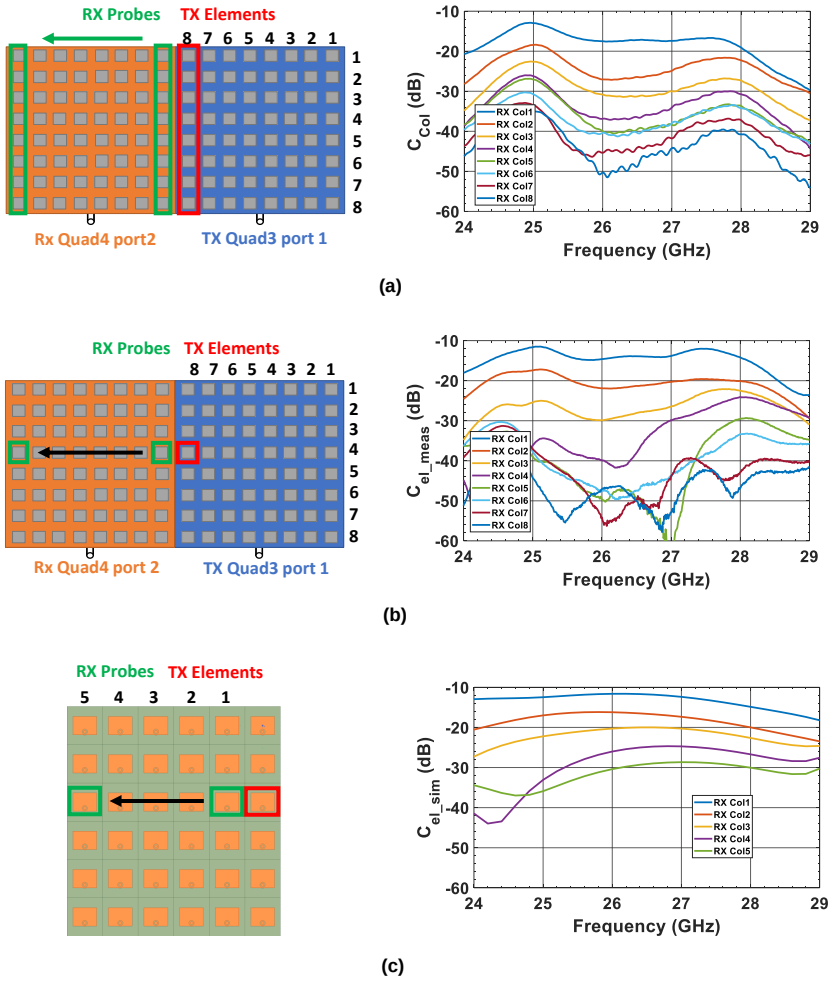

Figure 5.5: Measured coupling levels from (a) column 8 of quad 3 in TX mode and (b) column 8 row 4 of quad 3 in TX mode to different RX probes in quad 4. (c) Simulated coupling levels from the TX element to different RX elements on row 3 in a finite 6×6 array.

Fig. 5.5(a), (b), and (c) present the column-to-column coupling levels obtained using the measured port-to-port S_{21} and (5.4), the element-to-element coupling level calculated using the measured S_{21} and (5.3), and the element-to-element coupling level simulated in a finite 6×6 array, respectively. Both the column-to-column and the element-to-element coupling levels are close to the simulated ones but decrease faster when the RX probes move away from the TX antennas. Due to the higher transmitted and received power, and therefore higher signal-to-noise ratio in the column-to-column coupling experiment, it is chosen over the element-to-element method for

measuring EVM in the near field.

One problem emerges when measuring the EVM using near-field coupling in the high TX power region. Because of the high coupling level between the adjacent TX and RX columns, the RX channels can be easily saturated which results in non-accurate TX channel EVM measurements (the receiver now is contribution to the measured EVM). For example, if all the TX channels in a column are operated at their 1-dB compression point (OP1dB = 10 dBm), the average received power of each RX channel in a column is

$$P_{el\_Rx} = OP1dB + 10log8 + C_{Col} + 2L_{ant} - 10log8 = -10.4 \text{ dBm} \tag{5.5}$$

which is much higher than the -30 dBm input P1dB of the RX channel. As a results, RX columns far away from the TX column should be selected as probes to measure the EVM in high power mode.

5.3 EVM Measurements

Fig. 5.6(a) presents the setup for measuring the EVM in the near field. A 64-QAM 100 MBaud modulated signal is sent from the Keysight M8195 arbitrary waveform generator (AWG) and amplified by a power amplifier. An variable attenuator is used to adjust the input power level before the signal is fed to the input of quad 3 of the $4\times8\times8$ array. The Keysight DSOZ632A digital oscilloscope (DSO) is connected to RF port of quad 4 and the signal is received and demodulated using the VSA 89600A software in the DSO. A standard-gain horn antenna is set up in the far field and connected to a power meter to measure the effective isotropic radiated power (EIRP) of the array during EVM measurement. As a reference, the EVM is also measured in the far field with the measurement setup shown in Fig. 5.6(b). Instead of using quad 4 of the array as a receiver, the DSO is connected to the horn antenna, and a power meter is also connected to the horn antenna through a -10 dB coupler to measure the received power and EIRP.

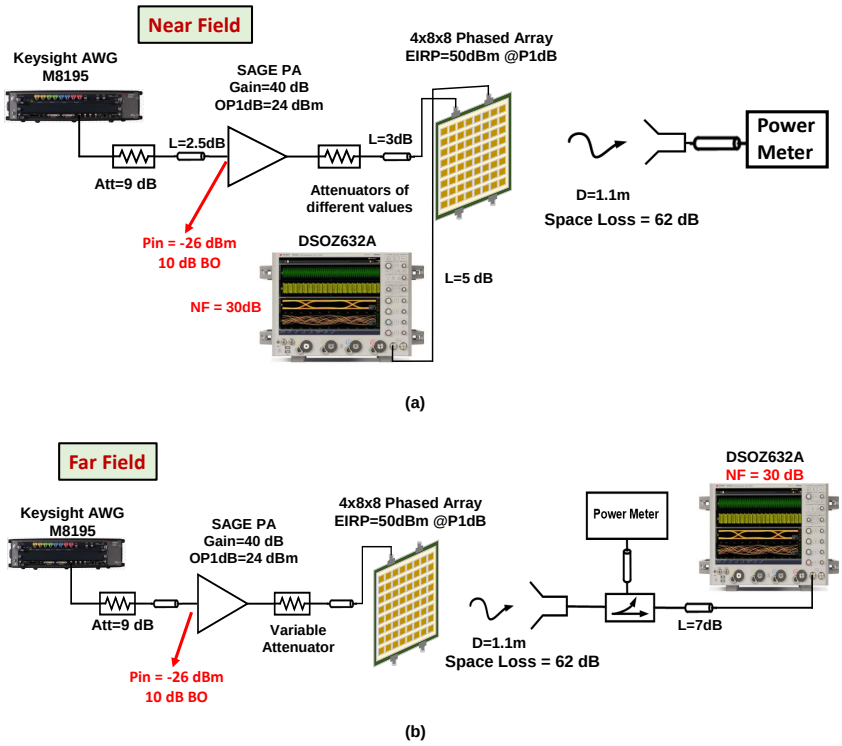

Figure 5.6: Setup of (a) near-field and (b) far-field EVM measurements.

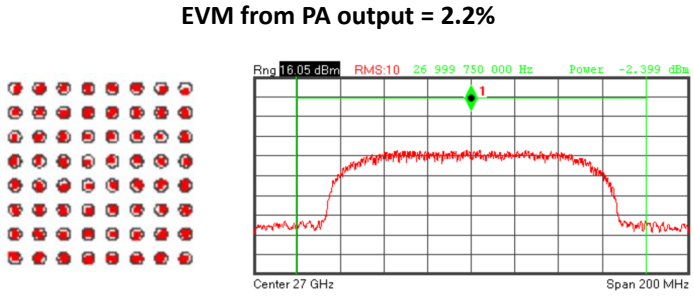

Figure 5.7: Reference constellation, spectrum and EVM level at the PA output for 64-QAM 100 Mbaud waveform.

Fig. 5.7 presents the constellation, spectrum and EVM level (2.2% referred to the RMS of the constellation) at the PA output for a 64-QAM 100 Mbaud waveform as a reference. This value represents the EVM level of the measurement setup system and is theoretically the minimum EVM that can be achieved through the array.

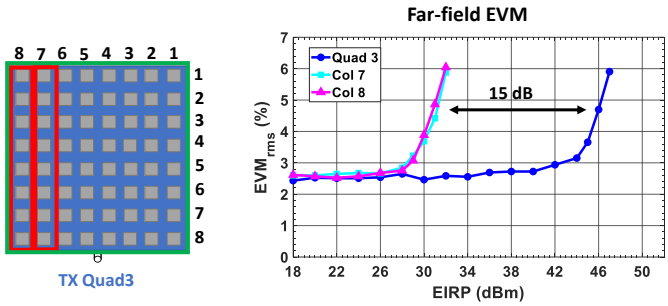

Figure 5.8: Reference EVM versus EIRP of 64-QAM 100 MBaud signal for entire quad 3, column 7 and column 8 of quad 3 in TX mode measured in the far field.

Fig. 5.8 presents the far-field measured EVM versus EIRP of 64-QAM 100 MBaud signal when the entire quad 3, column 7, and column 8 are turned on in TX mode, respectively. The EVM of column 7 and column 8 are very close to each other, are 15 dB lower than when the entire quad 3 is turned on. The difference in EIRP is smaller than the 18 dB we expected, which can be caused by narrower beam width of the 8×8 quad, beam pointing angle error, and the lack of calibration on the 8×8 array.

As mentioned in section II, the EVM in the high power region needs to be measured in the near field using RX columns far away from the TX one. Fig. 5.9 presents the near-field EVM of column 8 in quad 3 in TX mode measured by column 6 in quad 4 in the RX mode. At EIRP > 26 dBm, the EVM increases quickly due to the linearity of the channels. At EIRP < 18 dBm, the EVM also increases quickly due to the signal-to-noise ratio of the received system, and the EVM from 18 to 26 dBm is close to the system EVM, which indicates that it is dominated by the measurement setup.

The total transmitted power from the TX column can be calculated from the EIRP using

$$P_{Col\_Tx} = EIRP - 10log8 - G_{ant} - L_{ant} = P_{Col\_Tx} - 12.5 \text{ dBm} \tag{5.6}$$

where G_{ant} = 5 dB is the gain of the patch antenna. The average received power per element can

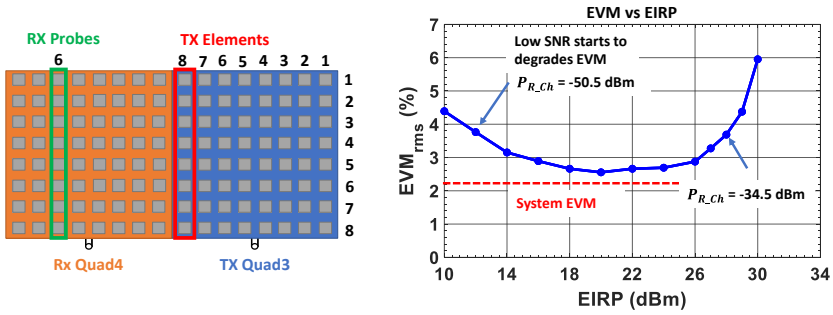

Figure 5.9: EVM versus EIRP of 64-QAM 100 MBaud signal of column 8 of quad 3 in TX mode measured by column 6 of quad 4 in RX mode using near field coupling.

be calculated using

$$P_{el\_Rx} = P_{Col\_Tx} + C_{col} + 2L_{ant} - 10log8 = P_{Col\_Rx} - 9 \text{ dBm} \tag{5.7}$$

where C_{col} = -38 dB at 27 GHz from column 8 in quad 3 to column 6 in quad 4. Using 5.6 and 5.7, the average received power per element at EIRP = 28 dBm is -34.5 dBm. At this power level, the TX channels are backed off by 4 dB and the RX channels by 4.5 dB, which indicates that the EVM can be affected by the linearity of both TX and RX channels. At EIRP = 12 dBm, the average received power is -50.5 dBm and the received power at the DSO input is -37 dBm. The DSO has a noise figure of 30 dB and noise floor of -144 dBm/Hz. For a 100 MHz modulated signal, the DSO noise floor is $-144 + 10log(10^8) = -64$ dBm, and the resulting SNR at the DSO is 27 dB. At 27 dB SNR, the calculated EVM is 4.4%, a little higher than the 3.9% measured value. This can be caused by measurement errors since the coupling levels and the EVM are measured in different setups, and only 1 dB higher SNR can decrease the EVM to 4%. A low noise amplifier can be used at the DSO input to remove the EVM limitations caused by the low SNR at the DSO input.

Instead of using an LNA to improve the SNR, different columns of RX probes are used to measure the EVM at different power levels. Fig. 5.10(a) presents the EVM versus EIRP measured

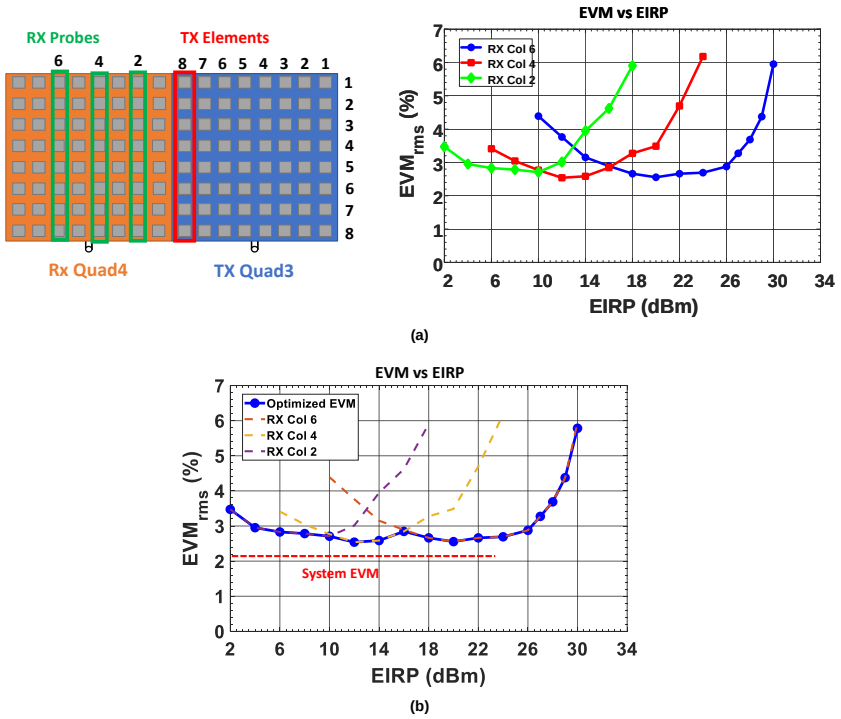

Figure 5.10: (a) EVM versus EIRP of 64-QAM 100 MBaud signal of column 8 of quad 3 in TX mode measured by column 2, 4, 6 of quad 4 in RX mode using near field coupling. (b) Combined optimized near-field EVM of quad 3 column 8 in TX mode.

from three different columns of RX probes. As expected, the curves show minimum EVM at different EIRP levels and can be combined to alleviate the effect of RX channel linearity at high power levels and received SNR at low power levels (fig. 5.10(b)). This method extends the EVM measurement range and reduces the effects of other factors in the measurement system to better represents the true performance of the TX channels.

Fig. 5.11 presents the comparison between the EVM of column 8 in quad 3 in the TX mode measured in the far field and measured in the near field using column 6 in RX mode. The two curves match closely from EIRP = 18 dBm to 26 dBm, but the EVM measured in the near field starts to increase at a lower EIRP values. At the same EVM level of 5%, the EIRP is 2 dB lower for the near-field results, which again indicates the effect of RX channel linearity. Columns further away have been used as RX probe in quad 4, but as shown in Fig. 5.5(a), ripples appear

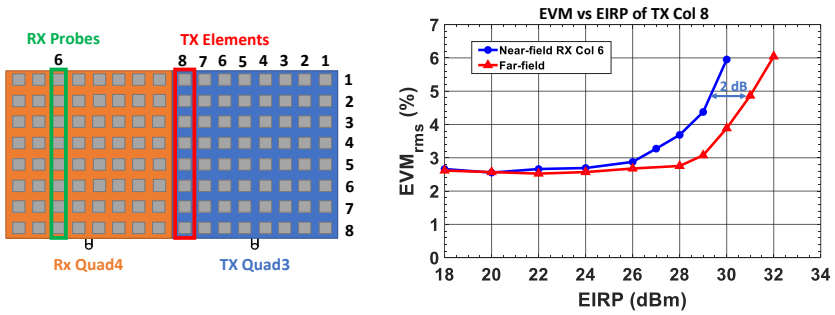

Figure 5.11: Comparison of EVM vs EIRP of 64-QAM 100 MBaud signal of quad 3 column 8 in TX mode between far-field measurements and near-field measurements using quad 4 column 6 in RX mode.

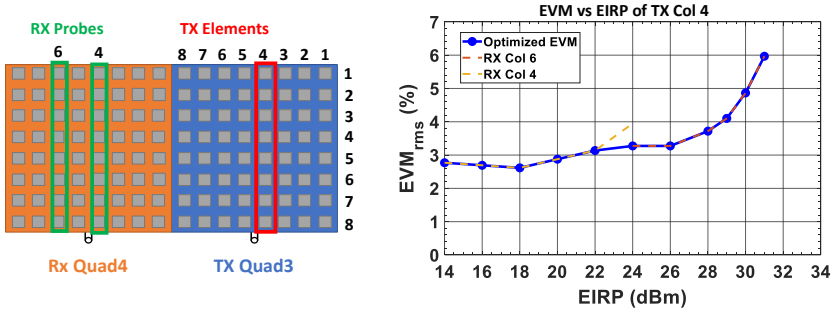

Figure 5.12: EVM versus EIRP of quad 3 column 4 in TX mode measured using quad 4 column 4 and 6 in RX mode.

due to coupling cancellation and this causes the received signal to be unstable.

Fig. 5.12 presents the EVM of column 4 in quad 3 in the TX mode measured from column 4 and 6 in quad 4 in the RX mode, which shows that the same method can be applied to different TX columns and obtain similar results and a wider dynamic range.

5.4 Conclusion

This dissertation presents a method to measure the error vector magnitude of a phased array in the near field, which eliminates the requirement for complex far-field measurement setups, reduces the cost of the measurement systems, and enables the calibration and verification to be

performed on phased arrays deployed in the field. The results show similar trends compared to the far field ones, with the linearity limited by the RX channels and the EVM rising sooner as EIRP increases.

5.5 Acknowledgment

The authors thank Kyocera International, San Diego, for assembling the arrays in their state of the art assembly line, and the Keysight team, Santa Rosa, for technical discussions and state-of-the-art equipment. This work was supported by the Semiconductor Research Corporation (SRC) and the Defense Advanced Research Projects Agency (DARPA) under the JUMP program with a DSSP addition.

Chapter 5, is coauthored with Nafe, Ahmed, Yin, Yusheng and Rebeiz, Gabriel M. The dissertation author was the primary investigator and author of this chapter.

Chapter 6

Conclusion and Future Work

6.1 Conclusion

This dissertation presented research on low cost planar phased-array systems. It has shown several use cases for phased arrays with emphasis on different aspects of their performance. Different methods were presented to resolved their existing artifacts and improve their performance in either a general way or optimized for certain applications.

In chapter 2, the effect of intersymbol interference created by phased arrays when they are scanned was presented and analyzed. The ISI increase with the scan angle and data rate, which can cause degradation in EVM particular in the high-bandwidth 5G communication. This is an effect from the use of phase shifters in the beamformer chips and it was shown that the ISI can be equalized and eliminated by a simple linear equalizer, resulting in the minimum EVM achievable by the system. The results were both simulated and demonstrated on a 16×16 phased array, proving that even with the high data rate communication in 5G, a complicated true-time delay module is not necessary for a high performing phased-array system.

In chapter 3, a novel method of greatly reducing the number of elements while keeping narrow beamwidths and low sidelobe levels was presented. The approach utilizes the co-design

of TX and RX arrays, and through a numerous iterations of randomly generated TX and RX array designs, finds the optimal combination that yields the lowest TX×RX sidelobe levels, which is suitable for radar applications. Such design has a high gain and EIRP compared to phased arrays with the same number of elements that are uniformly distributed on the aperture at 0.5λ spacing. A -40 dB TX×RX sidelobe level was presented and low sidelobes can be maintained up to 60° scan. For a automotive radar system that needs to be produced in large volume, this method reduces the cost of the system significantly.

In chapter 4, a new method of calibrating the phased array based on 2×2 sub-arrays was presented. It was shown that when 4 channels in a 2×2 quad are activated, the active input impedance is closer to that of a infinite array, and closer to a fully activated phased array under normal operation conditions. It also presented that the patterns of the 2×2 quads show lower variations and ripples, and therefore yield a more robust calibration at different scan angles. The VGA range needed for this method is lower, which improves the array performances with taper. Although any systematic error within the 2×2 quad needs to be calibrated in advance, the new method is still overall an improvement compared to the traditional single element calibration, with an extra benefit of reducing the measurement time by 75%.

In chapter 5, a method of measuring the EVM of a phased array in the near field was presented and investigated. This is an extension of the built-in-selt-test (BIST) phased array calibration in the near field [13]. The performance of the phased array and its calibration can be verified through EVM measurements. This method has shown close results to the ones measured in the far field, with the RX channels acting as probes limiting the linearity of the measurement systems. The resulting EVM rises earlier as EIRP increase. Nonetheless, near-field EVM measurements were shown to be a viable method for phased arrays deployed in the field.

6.2 Future Work

The phased array calibration and optimization methods presented in this dissertation may be expanded and improved in a few aspects:

1) For the ISI equalization, an analog-to-digital converter and digital equalizer can be implemented after down-converting the RF signal to IF frequencies. The equalizer architecture can be implemented on an FPGA instead of using the equalizer in the digital oscilloscope.

2) For the randomized array with reduced elements, the presented method uses a simple random search of different phased array combinations. An optimized adaptive search algorithm can be used to reduce the search time and possibly improve the results. The existing search seeks to only optimize the sidelobe levels at broadside but other parameters such as sidelobe levels at different scan angles and directivity can be added to find the required random distributions.

3) For the 2×2 calibration method, an argument that the active impedance is closer to a fully activated array was made. It would be useful to compare the measurement results to those measured with a near-field scanner, where all elements in the array are activated as well.

4) For the near-field EVM measurements, the results can be improved by improving the linearity of the RX channels. This can be done by reducing the gain of the RX LNA in the current system, but only to some extend. RX channels with higher linearity should be used for this measurements. A column-to-column EVM measurement was chosen due to the coupling cancellation when the entire array was turned on. It would be helpful to study the canceling mechanism and the relationship of the EVM of a each column to the EVM of the entire array.

Bibliography

[1] "BEYOND5 – about the project." [Online]. Available: https://www.beyond5project.org/about-project/

[2] "Golbal update on spectrum for 4G & 5G." [Online]. Available: https://www.qualcomm.com/media/documents/files/spectrum-for-4g-and-5g.pdf

[3] "Making 5G NR mmWave a commercial reality in your smartphone and beyond." [Online]. Available: https://www.qualcomm.com/media/documents/files/making-5g-mmwave-a-commercial-reality-in-your-smartphone.pdf

[4] "Samsung unveils new 5G NR integrated radio supporting 28GHz at MWC LA 2019." [Online]. Available: https://news.samsung.com/global/samsung-unveils-new-5g-nr-integrated-radio-supporting-28ghz-at-mwc-la-2019

[5] "Making 5G a reality: Addressing the strong mobile broadband demand in 2019 & beyond." [Online]. Available: https://www.qualcomm.com/media/documents/files/making-5g-a-reality-addressing-the-strong-mobile-broadband-demand-in-2019-beyond.pdf

[6] "Starlink review: Broadband dreams fall to earth." [Online]. Available: https://www.theverge.com/22435030/starlink-satellite-internet-spacex-review

[7] "Dumping and extracting the spacex starlink user terminal firmware." [Online]. Available: https://www.esat.kuleuven.be/cosic/blog/dumping-and-extracting-the-spacex-starlink-user-terminal-firmware/

[8] "Earth station antenna performance standards." [Online]. Available: https://www.law.cornell.edu/cfr/text/47/25.209

[9] "TEF810X: TEF810x fully-integrated 77 GHz radar transceiver." [Online]. Available: https://www.nxp.com/products/radio-frequency/radar-transceivers/tef810x-fully-integrated-77-ghz-radar-transceiver:TEF810X

[10] Y. Yin, Z. Zhang, T. Kanar, S. Zihir, and G. M. Rebeiz, "A 24-29.5 Ghz 256-element 5G phased-array with 65.5 dBm peak EIRP and 256-QAM modulation," in *2020 IEEE MTT-S International Microwave Symposium (IMS)*, Los Angeles, CA, Aug. 2020.

[11] "Everything you need to know about 5G." [Online]. Available: https://spectrum.ieee.org/everything-you-need-to-know-about-5g

[12] [Online]. Available: https://www.starlink.com/

[13] A. Nafe, A. H. Aljuhani, K. Kibaroglu, M. Sayginer, and G. M. Rebeiz, "In-situ self-test and self-calibration of dual-polarized 5G TRX phased arrays leveraging orthogonal-polarization antenna couplings," in *2020 IEEE/MTT-S International Microwave Symposium (IMS)*, 2020, pp. 1081–1084.

[14] W. Roh, J. Seol, J. Park, B. Lee, J. Lee, Y. Kim, J. Cho, K. Cheun, and F. Aryanfar, "Millimeter-wave beamforming as an enabling technology for 5G cellular communications: theoretical feasibility and prototype results," *IEEE Commun. Mag.*, vol. 52, no. 2, pp. 106–113, Feb. 2014.

[15] S. Onoe, "Evolution of 5G mobile technology toward 2020 and beyond," in *2016 IEEE International Solid-State Circuits Conference (ISSCC)*, Jan. 2016, pp. 23–28.

[16] J. D. Dunworth, A. Homayoun, B. Ku, Y. Ou, K. Chakraborty, G. Liu, T. Segoria, J. Lerdworatawee, J. W. Park, H. Park, H. Hedayati, D. Lu, P. Monat, K. Douglas, and V. Aparin, "A 28GHz bulk-CMOS dual-polarization phased-array transceiver with 24 channels for 5G user and basestation equipment," in *2018 IEEE International Solid - State Circuits Conference - (ISSCC)*, Feb. 2018, pp. 70–72.

[17] A. G. Roy, O. Inac, A. Singh, T. Mukatel, O. Brandelstein, T. W. Brown, S. Abughazaleh, J. S. Hayden, B. Park, G. Bachmanek, T. J. Kao, J. Hagn, S. Dalmia, D. Shoham, B. Davis, I. Fisher, R. Sover, A. Freiman, B. Xiao, B. Singh, and J. Jensen, "A 37-40 GHz phased array front-end with dual polarization for 5G MIMO beamforming applications," in *2019 IEEE Radio Frequency Integrated Circuits Symposium (RFIC)*, Boston, MA, Jun. 2019, pp. 251–254.

[18] Y. Yoon, K. H. An, D. Kang, K. Kim, S. Lee, J. S. Jang, D. Minn, B. Suh, J. Lee, J. Kim, M. Kim, J. H. Lee, S. T. Choi, J. Son, and S. Yang, "A highly linear 28GHz 16-element phased-array receiver with wide gain control for 5G NR application," in *2019 IEEE Radio Frequency Integrated Circuits Symposium (RFIC)*, Boston, MA, Jun. 2019, pp. 287–290.

[19] J. Pang, Z. Li, R. Kubozoe, X. Luo, R. Wu, Y. Wang, D. You, A. A. Fadila, R. Saengchan, T. Nakamura, J. Alvin, D. Matsumoto, A. T. Narayanan, B. Liu, J. Qiu, H. Liu, Z. Sun, H. Huang, K. K. Tokgoz, K. Motoi, N. Oshima, S. Hori, K. Kunihiro, T. Kaneko, A. Shirane, and K. Okada, "21.1 a 28GHz CMOS phased-array beamformer utilizing neutralized bi-directional technique supporting dual-polarized MIMO for 5G NR," in *2019 IEEE International Solid- State Circuits Conference - (ISSCC)*, Feb. 2019, pp. 344–346.

[20] K. Kibaroglu, M. Sayginer, T. Phelps, and G. M. Rebeiz, "A 64-element 28-GHz phased-array transceiver with 52-dBm EIRP and 8–12-Gb/s 5G link at 300 meters without any calibration," *IEEE Trans. Microw. Theory Tech.*, vol. 66, no. 12, pp. 5796–5811, Dec. 2018.

[21] J. Pang, R. Wu, Y. Wang, M. Dome, H. Kato, H. Huang, A. Tharayil Narayanan, H. Liu, B. Liu, T. Nakamura, T. Fujimura, M. Kawabuchi, R. Kubozoe, T. Miura, D. Matsumoto, Z. Li, N. Oshima, K. Motoi, S. Hori, K. Kunihiro, T. Kaneko, A. Shirane, and K. Okada, "A 28-GHz CMOS phased-array transceiver based on LO phase-shifting architecture with gain invariant phase tuning for 5g new radio," *IEEE J. Solid-State Circuits*, vol. 54, no. 5, pp. 1228–1242, May. 2019.

[22] A. Nafe, M. Sayginer, K. Kibaroglu, and G. M. Rebeiz, "2×64-element dual-polarized dual-beam single-aperture 28 GHz phased array with 2×30 Gbps links for 5G polarization MIMO," *IEEE Trans. Microw. Theory Tech.*, vol. 68, no. 9, pp. 3872–3884, 2020.

[23] H. Kim, B. Park, S. Song, T. Moon, S. Kim, J. Kim, J. Chang, and Y. Ho, "A 28-GHz CMOS direct conversion transceiver with packaged 2×4 antenna array for 5G cellular system," *IEEE J. Solid-State Circuits*, vol. 53, no. 5, pp. 1245–1259, May 2018.

[24] K. Kibaroglu, M. Sayginer, and G. M. Rebeiz, "A low-cost scalable 32-element 28-GHz phased array transceiver for 5G communication links based on a 2×2 beamformer flip-chip unit cell," *IEEE J. Solid-State Circuits*, vol. 53, no. 5, pp. 1260–1274, May 2018.

[25] B. Ustundag, K. Kibaroglu, M. Sayginer, and G. M. Rebeiz, "A wideband high-power multi-standard 23–31 GHz 2×2 quad beamformer chip in SiGe with>15 dBm OP1dB per channel," in *2018 IEEE Radio Frequency Integrated Circuits Symposium (RFIC)*, Philadelphia, PA, Jun. 2018, pp. 60–63.

[26] Y. Yin, S. Zihir, T. Kanar, and G. M. Rebeiz, "A 37-42 GHz 8x8 phased-array for 5G communication systems with 48-50 dBm EIRP," in *2019 IEEE MTT-S International Microwave Symposium (IMS)*, Boston, MA, Jun. 2019, pp. 480–483.

[27] Q. Ma, H. Chung, Y. Yin, T. Kanar, S. Zihir, and G. M. Rebeiz, "A 5G 24-30 GHz 2x32 element dual-polarized dual-beam phased array base-station for 2x2 MIMO system," in *2019 IEEE Global Communications Conference (GLOBECOM)*, Waikoloa, HI, 2019, pp. 1–5.

[28] B. Rupakula, S. Zihir, and G. M. Rebeiz, "Low complexity 54–63-GHz transmit/receive 64- and 128-element 2-D-scanning phased-arrays on multilayer organic substrates with 64-QAM 30-Gbps data rates," *IEEE Trans. Microw. Theory Tech.*, vol. 67, no. 12, pp. 5268–5281, Dec. 2019.

[29] B. Rupakula, A. Nafe, S. Zihir, Y. Wang, T. Lin, and G. Rebeiz, "63.5–65.5-GHz transmit/receive phased-array communication link with 0.5–2 Gb/s at 100–800 m and ± 50° scan angles," *IEEE Trans. Microw. Theory Tech.*, vol. 66, no. 9, pp. 4108–4120, Sep. 2018.

[30] B. Saltzberg, "Error probabilities for a binary signal perturbed by intersymbol interference and gaussian noise," *IEEE Transactions on Communications Systems*, vol. 12, no. 1, pp. 117–120, Mar. 1964.

[31] M. Aaron and D. Tufts, "Intersymbol interference and error probability," *IEEE Trans. Inf. Theory*, vol. 12, no. 1, pp. 26–34, Jan. 1966.

[32] C. Helstrom, "Calculating error probabilities for intersymbol and cochannel interference," *IEEE Trans. Commun.*, vol. 34, no. 5, pp. 430–435, May 1986.

[33] R. Lugannani, "Intersymbol interference and probability of error in digital systems," *IEEE Trans. Inf. Theory*, vol. 15, no. 6, pp. 682–688, Nov. 1969.

[34] N. C. Beaulieu, "The evaluation of error probabilities for intersymbol and cochannel interference," *IEEE Trans. Commun.*, vol. 39, no. 12, pp. 1740–1749, Dec. 1991.

[35] R. W. Lucky, "Techniques for adaptive equalization of digital communication systems," *The Bell System Technical Journal*, vol. 45, no. 2, pp. 255–286, Feb. 1966.

[36] P. Monsen, "MMSE equalization of interference on fading diversity channels," *IEEE Trans. Commun.*, vol. 32, no. 1, pp. 5–12, Jan. 1984.

[37] C. Niessen and D. Willim, "Adaptive equalizer for pulse transmission," *IEEE Trans. Commun. Technol.*, vol. 18, no. 4, pp. 377–395, Aug. 1970.

[38] E. Biglieri, A. Gersho, R. Gitlin, and Tong Lim, "Adaptive cancellation of nonlinear intersymbol interference for voiceband data transmission," *IEEE J. Sel. Areas Commun.*, vol. 2, no. 5, pp. 765–777, Sep. 1984.

[39] J. Proakis and J. Miller, "An adaptive receiver for digital signaling through channels with intersymbol interference," *IEEE Trans. Inf. Theory*, vol. 15, no. 4, pp. 484–497, Jul. 1969.

[40] H. Yoshino, K. Fukawa, and H. Sukuki, "Interference cancelling equalizer (ICE) for mobile radio communication," *IEEE Trans. Veh. Technol.*, vol. 46, no. 4, pp. 849–861, Nov. 1997.

[41] O. T. Von Ramm and S. W. Smith, "Beam steering with linear arrays," *IEEE Trans. Bio-Med. Eng.*, vol. BME-30, no. 8, pp. 438–452, 1983.

[42] M. Steer, "Antennas and the RF link," in *Microwave and RF Design, Volume 1: Radio Systems*, 3rd ed., ser. Microwave and RF Design. Raleigh, NC, USA: University of North Carolina Press, 2019, ch. 4, pp. 129–172.

[43] B. Sklar, "Baseband demodulation/dectection," in *Digital Communications: Fundamentals and Applications*, 2nd ed. Upper Saddle River, NJ, USA: Prentice-Hall PTR, 2001, ch. 3, pp. 104–166.

[44] B. Razavi, "Communication concepts," in *RF Microelectronics*, 2nd ed. Upper Saddle River, NJ, USA: Prentice-Hall PTR, 2012, ch. 3, pp. 91–153.

[45] E. Brookner, "Phased-array radars," *Sci. Am.*, vol. 252, pp. 94–102, Feb. 1985.

[46] A. J. Fenn, D. H. Temme, W. P. Delaney, and W. E. Courtney, "The development of phased-array radar technology," *Lincoln Lab. J.*, vol. 12, no. 2, pp. 321–340, 2000.

[47] G. M. Rebeiz and K. Koh, "Silicon rfics for phased arrays," *IEEE Microwave Magazine*, vol. 10, no. 3, pp. 96–103, 2009.

[48] B. Ku, P. Schmalenberg, O. Inac, O. D. Gurbuz, J. S. Lee, K. Shiozaki, and G. M. Rebeiz, "A 77–81-ghz 16-element phased-array receiver with $\pm 50^{\circ}$ beam scanning for advanced automotive radars," *IEEE Transactions on Microwave Theory and Techniques*, vol. 62, no. 11, pp. 2823–2832, 2014.

[49] K. Koh and G. M. Rebeiz, "An x- and ku-band 8-element phased-array receiver in 0.18-μm sige bicmos technology," *IEEE Journal of Solid-State Circuits*, vol. 43, no. 6, pp. 1360–1371, 2008.

[50] B. Rupakula, A. H. Aljuhani, and G. M. Rebeiz, "Limited scan-angle phased arrays using randomly grouped subarrays and reduced number of phase shifters," *IEEE Transactions on Antennas and Propagation*, vol. 68, no. 1, pp. 70–80, 2020.

[51] K. V. Mishra, I. Kahane, A. Kaufmann, and Y. C. Eldar, "High spatial resolution radar using thinned arrays," in *2017 IEEE Radar Conference (RadarConf)*, 2017, pp. 1119–1124.

[52] P. Nandi and J. S. Roy, "Optimization of sidelobe level of thinned phased array antenna using genetic algorithm and particle swarm optimization," in *2015 IEEE International WIE Conference on Electrical and Computer Engineering (WIECON-ECE)*, 2015, pp. 27–30.

[53] M. G. Bray, D. H. Werner, D. W. Boeringer, and D. W. Machuga, "Optimization of thinned aperiodic linear phased arrays using genetic algorithms to reduce grating lobes during scanning," *IEEE Transactions on Antennas and Propagation*, vol. 50, no. 12, pp. 1732–1742, 2002.

[54] Y. Chen, S. Yang, and Z. Nie, "Synthesis of uniform amplitude thinned linear phased arrays using the differential evolution algorithm," *Electromagnetics*, vol. 27, no. 5, pp. 287–297, 2007.

[55] D. G. Leeper, "Isophoric arrays-massively thinned phased arrays with well-controlled sidelobes," *IEEE Transactions on Antennas and Propagation*, vol. 47, no. 12, pp. 1825–1835, 1999.

[56] C. Balanis, "Fundamental parameters and figures-of-merit of antennas," in *Antenna Theory: Analysis and Design*, 4th ed. Hoboken, NJ, USA: John Wiley & Sons, 2016, ch. 2, pp. 25–126.

[57] G. Gültepe, T. Kanar, S. Zihir, and G. M. Rebeiz, "A 1024-element Ku-band SATCOM phased-array transmitter with 45-dBW single-polarization EIRP," *IEEE Trans. Microw. Theory Tech.*, vol. 69, no. 9, pp. 4157–4168, 2021.

[58] G. Gültepe, T. Kanar, S. Zihir, and G. M. Rebeiz, "A 1024-element Ku-band SATCOM dual-polarized receiver with $>$ 10-dB/K G/T and embedded transmit rejection filter," *IEEE Trans. Microw. Theory Tech.*, vol. 69, no. 7, pp. 3484–3495, 2021.

[59] K. K. Wei Low, S. Zihir, T. Kanar, and G. M. Rebeiz, "A 27-31 GHz 1024-element Ka-band SATCOM phased-array transmitter with 49.5-dBW peak EIRP, 1-dB AR, and $\pm 70^\circ$ beam scanning," *IEEE Trans. Microw. Theory Tech.*, 2021 (Submitted).

[60] K. K. Wei Low, T. Kanar, S. Zihir, and G. M. Rebeiz, "A 17.7-20.2 GHz 1024-element K-band SATCOM phased-array receiver with 8.1 dB/K G/T, $\pm 70^\circ$ beam scanning, and high transmit isolation," *IEEE Trans. Microw. Theory Tech.*, 2021 (Submitted).

[61] E. Lier, D. Purdy, J. Ashe, and G. Kautz, "An on-board integrated beam conditioning system for active phased array satellite antennas," in *Proceedings 2000 IEEE International Conference on Phased Array Systems and Technology (Cat. No.00TH8510)*, 2000, pp. 509–512.

[62] E. Lier, M. Zemlyansky, D. Purdy, and D. Farina, "Phased array calibration and characterization based on orthogonal coding: Theory and experimental validation," in *2010 IEEE International Symposium on Phased Array Systems and Technology*, 2010, pp. 271–278.

[63] T. Phelps, Z. Zhang, and G. M. Rebeiz, "Simultaneous channel phased- array calibration using orthogonal codes and post coding," in *2021 IEEE MTT-S International Microwave Symposium (IMS)*, Atlanta, GA, Aug. 2021.

[64] D. Pozar, "Analysis of finite phased arrays of printed dipoles," *IEEE Trans. Antennas Propag.*, vol. 33, no. 10, pp. 1045–1053, 1985.

[65] D. Pozar, "Considerations for millimeter wave printed antennas," *IEEE Trans. Antennas Propag.*, vol. 31, no. 5, pp. 740–747, 1983.

[66] J. A. Kasemodel, C. Chen, and J. L. Volakis, "Broadband planar wide-scan array employing tightly coupled elements and integrated balun," in *2010 IEEE International Symposium on Phased Array Systems and Technology*, Waltham, MA, 2010, pp. 467–472.

[67] T. Kanar, S. Zihir, and G. M. Rebeiz, "A 2–15-GHz accurate built-in-self-test system for wideband phased arrays using self-correcting eight-state I/Q mixers," *IEEE Trans. Microw. Theory Tech.*, vol. 64, no. 12, pp. 4250–4261, 2016.

[68] O. Inac, D. Shin, and G. M. Rebeiz, "A phased array RFIC with built-in self-test capabilities," *IEEE Trans. Microw. Theory Tech.*, vol. 60, no. 1, pp. 139–148, 2012.

[69] Y. Wang, R. Wu, J. Pang, D. You, A. A. Fadila, R. Saengchan, X. Fu, D. Matsumoto, T. Nakamura, R. Kubozoe, M. Kawabuchi, B. Liu, H. Zhang, J. Qiu, H. Liu, W. Deng, N. Oshima, K. Motoi, S. Hori, K. Kunihiro, T. Kaneko, A. Shirane, and K. Okada, "A 39GHz 64-element phased-array CMOS transceiver with built-in calibration for large-array

5G NR," in *2019 IEEE Radio Frequency Integrated Circuits Symposium (RFIC)*, Boston, MA, Jun. 2019, pp. 279–282.

[70] K. Greene, V. Chauhan, and B. Floyd, "Built-in test of phased arrays using code-modulated interferometry," *IEEE Trans. Microw. Theory Tech.*, vol. 66, no. 5, pp. 2463–2479, 2018.